X-RAY DIFFRACTION ANALYSIS OF SMALL GOLD NANOPOWDERS

MERDAN BATYROV

ÖZYEĞİN UNIVERSITY

FEBRUARY, 2025

X-RAY DIFFRACTION ANALYSIS OF SMALL GOLD NANOPOWDERS

by
Merdan Batyrov

Dissertation
Submitted in Partial Fulfillment of the
Requirements for the Degree of

Doctor of Philosophy

in
Mechanical Engineering

Advisor: Asst. Prof. Hande Öztürk Kaymaksüt
Co-Advisor: Assoc. Prof. İlknur Eruçar Fındıkçı

Graduate School of Science and Engineering
Özyeğin University
İstanbul

February, 2025

X-RAY DIFFRACTION ANALYSIS OF SMALL GOLD NANOPOWDERS

Approved by:

Asst. Prof. Hande Öztürk Kaymaksüt,
Advisor
Department of Mechanical Engineering
Özyeğin University

Asst. Prof. Erkan Şenses
Department of Chemical and Biological Engineering
Koç University

Assoc. Prof. Polat Şendur
Department of Mechanical Engineering
Özyeğin University

Prof. Sedat Nizamoğlu
Department of Electrical and Electronics Engineering
Koç University

Prof. Mehmet Burçin Ünlü
Department of Natural Sciences
Özyeğin University

Approval Date: February 7, 2025

To my family. To my beautiful and loyal companion, Şimşek.

DECLARATION OF ORIGINALITY

I hereby declare that I am the sole author of this thesis and that this is the true copy of my thesis, including the final revisions, approved by my thesis committee. All data and information have been obtained, produced, and presented in accordance with the rules of research ethics and principles of academic honesty. As required by these rules, to the best of my knowledge I have acknowledged ideas, thoughts, and any copyrighted material in accordance with the standard referencing rules. I certify that any part of this thesis has not been submitted for a degree or diploma in another educational institution.

Merdan Batyrov

ABSTRACT

Powder X-ray diffraction is a powerful method to characterize structure of materials in a non-destructive way. Conventionally, diffraction pattern of powder material consisting of crystallites is analyzed using Rietveld analysis, which provides structural parameters such as lattice parameter, atomic displacement parameter, and crystallite size. The technique is proven to work well when crystallite sizes are in micrometer-scale, that can be considered as a bulk with surface to volume ratio negligible. Therefore, infinite atomic plane assumption in Rietveld algorithm is satisfied. However, when crystallite size is in nanometer-scale, number of atomic planes is limited due to finite dimension of nanocrystal. Moreover, realistic nanocrystals exhibit different properties on surface region compared to core region, indicating non-periodic structure. We showed that the inconsistency between the algorithm and nanocrystal structure causes errors in extracted structural parameters. These errors are orders of magnitude higher than precision of lab diffractometers. The computational work was extended to Pair Distribution Function (PDF) analysis, which also showed similar trends. All of these errors were size-dependent and became negligible with increasing particle size or decreasing surface to volume ratio. Finally, we measured X-ray diffraction pattern of 14 nm gold nanocrystal using laboratory diffractometer. The measured PDF suffered from low X-ray energy accessible by such diffractometers. However, we showed that PDF analysis can still extract structural parameters using Attenuated Crystal Modeling (ACM). The better fit quality was achieved when realistic nanocrystals obtained from Molecular Dynamics (MD) simulation were modeled as polydispersed system.

Keywords: X-ray Diffraction Analysis, Nanocrystals, Pair Distribution Function Analysis, Molecular Dynamics simulation

ÖZET

Toz X-ışını kırınımı, malzemelerin yapısını tahribatsız bir şekilde karakterize etmek için güçlü bir yöntemdir. Geleneksel olarak, kristalitlerden oluşan toz malzemenin kırınım deseni, kafes parametresi, atomik yer değiştirme parametresi ve kristalit boyutu gibi yapısal parametreler sağlayan Rietveld analizi kullanılarak analiz edilir. Tekniğin, kristalit boyutları mikron ölçeğinde olduğunda, yani yüzey hacim oranı ihmal edilebilir bir kütle olarak düşünüldüğünde iyi çalıştığı kanıtlanmıştır. Bu nedenle, Rietveld algoritmasındaki sonsuz atomik düzlem varsayımı karşılanır. Ancak, kristalit boyutu nanometre ölçeğinde olduğunda, nanokristalin sonlu boyutundan dolayı atomik düzlemlerin sayısı sınırlıdır. Dahası, gerçekçi nanokristaller, çekirdek bölgesine kıyasla yüzey bölgesinde farklı özellikler sergiler ve bu da periyodik olmayan bir yapıyı gösterir. Algoritma ve nanokristal yapısı arasındaki tutarsızlığın, çıkarılan yapısal parametrelerde hatalara neden olduğunu gösterdik. Bu hatalar, laboratuvar difraktometrelerinin hassasiyetinden kat kat daha yüksektir. Hesaplamalı çalışma, benzer eğilimler gösteren Çift Dağılım Fonksiyonu (PDF) analizine genişletildi. Bu hataların tümü boyuta bağlıydı ve artan parçacık boyutu veya azalan yüzey hacim oranıyla ihmal edilebilir hale geldi. Son olarak, laboratuvar difraktometresi kullanarak 14 nm altın nanokristalinin X-ışını kırınım desenini ölçtük. Ölçülen PDF, bu tür difraktometreler tarafından erişilebilen düşük X-ışını enerjisinden etkilenmişti. Ancak, PDF analizinin Zayıflatılmış Kristal Modelleme (ACM) kullanarak yapısal parametreleri hala elde edilebileceğini gösterdik. Moleküler Dinamik (MD) simülasyonundan elde edilen gerçekçi nanokristaller polidispers sistem olarak modellendiğinde daha iyi uyum kalitesi elde edildi.

Anahtar Kelimeler: X-ışını Kırınımı Analizi, Nanokristaller, Çift Dağılım Fonksiyonu Analizi, Moleküler Dinamik simülasyonu

ACKNOWLEDGEMENTS

First, I want to thank my supervisor Prof. Hande Öztürk. I am grateful for her support. She provided me with opportunities that enabled me to study freely and travel to conferences abroad. I want to thank my coadvisor Prof. İlknur Eruçar for teaching me molecular dynamics simulations. I appreciate her guidance and support during paper writing. I feel lucky that I took an R programming course from Prof. Alper Yılmaz during my undergraduate study at Yıldız Technical University. I used the R language for most of my work during my Ph.D. studies.

I thank Mr. Remzi for helping me perform simulations at Ozyegin High Performance Computing Center (HPC); Mr. Yashar for helping me conduct an X-ray diffraction experiment at OzUBEX; My old lab mates: Taner for helping me perform atomic simulations during my first year, Abolfazl for good discussions about research, Büşra Palabıyık for her collaboration about MD simulations, Hamidreza for his preliminary works with Rietveld analysis; Ayşe Nur for her support while I was in the Materials laboratory; İlkin Yapıcı for introducing me macromolecular crystallography; Current CORAL lab members for sharing good moments; Vahid for sharing a cup of coffee with me every morning; My friends Marianna and Batyr for their support and help. I am grateful to my dissertation committee members, Prof. Polat Şendur, Prof. Mehmet Burçin Ünlü, Prof. Erkan Şenses, and Prof. Sedat Nizamoğlu for their time and efforts in helping me develop my thesis.

I gratefully acknowledge the Scientific and Technological Research Council of Turkey (TUBITAK) with grant 118C238 for supporting the works in this thesis.

TABLE OF CONTENTS

DECLARATION OF ORIGINALITY iv

ABSTRACT v

ÖZET vi

ACKNOWLEDGEMENTS vii

LIST OF TABLES xi

LIST OF FIGURES xii

LIST OF ACRONYMS AND ABBREVIATIONS xx

1 INTRODUCTION 1

2 THEORETICAL BACKGROUND 6

2.1 Introduction 6

2.2 Scattering by Free Electron 7

2.3 Scattering by Single Atom 9

2.4 Scattering by Small Crystal 12

2.4.1 Atomic Summation 13

2.4.2 Unit Cell Summation 15

2.5 Reciprocal Lattice and Bragg Law 19

3 MOLECULAR DYNAMICS SIMULATIONS AND CALCULATION OF POWDER X-RAY DIFFRACTION DATA OF THE REALISTIC NANOCRYSTALS . 22

3.1 Introduction 22

3.2 Creating Ideal Nanocrystals 23

3.3 Simulation Methodology 23

3.4 Structural Parameters in Real Space 25

3.4.1 Calculation of Local and Average Structural Parameters 25

3.4.2 Mean Square Displacement 26

3.4.3 Lattice Parameter and Lattice Strain 28

3.4.4 Particle Size 31
3.5 Effect of Force-Field Selection on the Core Lattice Parameter 32
3.6 Derivation of Debye Scattering Equation 35
3.7 Summary and Conclusions 36
4 RIETVELD ANALYSIS OF REALISTIC GOLD NANOCRYSTALS 38
4.1 Introduction 38
4.2 Rietveld Refinement Algorithm 40
4.2.1 Total Powder Intensity 40
4.2.2 Structure Factor 41
4.2.3 Profile Function – Size and Strain Broadening 42
4.3 Thermal Diffuse Scattering 43
4.4 Rietveld Refinement Methodology 47
4.5 Comparision of the Real Space and Extracted Structural Parameters from the Rietveld Refinement 50
4.5.1 Lattice Parameter and CTE 50
4.5.2 Static Displacement 56
4.5.3 MSD 59
4.6 Summary and Conclusions 65
5 PDF ANALYSIS OF REALISTIC GOLD NANOCRYSTSALS 68
5.1 Introduction 68
5.2 Obtaining the PDF of the Realistic Nanocrystals by Debye Scattering Equation 72
5.2.1 Generating X-ray Diffraction Data from Atom Coordinates of the Realistic Nanocrystals 72
5.2.2 Generating PDF Data from X-ray Diffraction Data 72
5.3 Small-Box PDF Refinement Algorithm 74
5.3.1 The G(r) Function 74
5.3.2 Atomic Disorder 75
5.3.3 Including Finite Q_{max} Effect with Window Function 76
5.4 PDF Refinement Methodology 78

5.5 Finite Q_{max} Effect on Extracted Structural Parameters from the PDF Refinement 81
5.6 Effect of Nanocrystal Surface on the Quality of PDF Refinement..... 83
5.7 Comparison of the Real Space and Extracted Structural Parameters from the PDF Refinement..... 87
5.7.1 Lattice Parameter 87
5.7.2 Particle Size..... 93
5.7.3 MSD..... 97
5.8 Summary and Conclusions 102
6 PERFORMING THE PDF REFINEMENT ON EXPERIMENTALLY MEASURED PDF WITH A LABORATORY X-RAY DIFFRACTOMETER 107
6.1 Introduction..... 107
6.2 Diffraction Pattern Measurement of 14 nm Gold Nanoparticle Powder with Lab Diffractometer 108
6.3 Model-Free Analysis of Measured PDF 111
6.4 PDF Refinement of Measured PDF by Including Finite Q_{max} Effect 115
6.4.1 Attenuated Crystal Modeling of PDF from Gold Nanocrystals 115
6.4.2 MD-Assisted Modelling of PDF from Polydispersed Realistic Gold Nanocrystals 118
6.5 Summary and Conclusions 121
7 CONCLUSIONS 126
REFERENCES 130
VITA 137

LIST OF TABLES

Table 3.1: The core lattice parameter dependence of 5 nm nanocrystal (300 K) on interatomic potential. 33

Table 4.1: Results of the two-step Rietveld scheme on snapshot intensities of our gold nanocrystals. (Only at 0 K the refined values are from static diffraction data.) % wR stands for the weighted residuals of the refinement reported by GSAS II, and it is used to evaluate the success of the refined crystallographic model. Values in parentheses are uncertainties reported by the software. 49

Table 5.1: Lattice parameters of the investigated nanopowders computed by real space calculations and by PDF refinement of the diffraction data. The three different refinement results from PDF analysis belong to three different peak-width models employed in DiffpyCMI. 90

Table 5.2: Average diameters of the investigated nanopowders computed in real space and by PDF refinement of the diffraction data. Three different refinement results are presented from PDF analysis where different peak broadening models were employed in each refinement scheme. 97

Table 5.3: Average MSDs of the investigated nanopowders calculated in real space and by PDF refinement of the simulated diffraction data. Three different refinement results are presented from PDF analysis where different peak broadening models were employed in each refinement scheme. 100

Table 6.1: PDF refined structural parameters. ACM modeling strategy is used. 117

Table 6.2: PDF refined structural parameters. MD-assisted modeling strategy is used. 120

LIST OF FIGURES

Figure 2.1: Unpolarized primary X-ray beam propagating in X-direction is scattered by free electron, causing electric field at observation point P in XY-plane. 8

Figure 2.2: Polarized primary X-ray beam propagating along $\mathbf{s}_0$ vector is scattered by a cluster of electrons around atom at origin O, causing electric field at observation point P. 10

Figure 2.3: Left) Small crystal is illustrated with cubic unit cells shown as dashed lines on $\mathbf{a}_1\mathbf{a}_2$ face. Atomic coordinate vector for i^{th} atom in the crystal is shown with $\mathbf{r}_i$ vector. Right) Diffraction geometry of the small crystal shown at left. $\mathbf{s}$ and $\mathbf{s}_0$ are primary and scattered beam directions, respectively. P is the detector position that is R distance away from crystal origin. 14

Figure 2.4: Left) A small crystal is illustrated with cubic unit cells shown as dashed lines on $\mathbf{a}_1\mathbf{a}_2$ face. The fractional atomic coordinate for the n^{th} atom in the unit cell is shown with $\mathbf{r}_n$ vector. Unit cell vector for m^{th} unit cell is shown with $\mathbf{R}_m$ vector, and $\mathbf{R}_m^n$ vector is atomic position for n^{th} atom in m^{th} unit cell. Right) Diffraction by small crystal shown at left. $\mathbf{s}$ and $\mathbf{s}_0$ are primary and scattered beam directions, respectively. P is the detector position that is R distance away from the crystal origin. 16

Figure 2.5: a) Diffraction from an atomic plane in real space. b) Ewald construction in reciprocal lattice. c) Powder X-ray diffraction measurement in reflection geometry. 20

Figure 3.1: Left) Change in the total energy of the spherical gold nanocrystal during MD simulations performed on ideal nanocrystalline atomic configuration. The resulting energy-minimized atomic configuration has less total energy and is thermodynamically stable. Right) The atomic configurations of ideal (blue markers) and energy-minimized versions (yellow markers) of the gold nanocrystal with 5 nm nominal diameter. The blue arrows show the displacement vector. 24

Figure 3.2: Atomic coordinates of a 5 nm diameter gold nanocrystal with a) ideal and b) equilibrated structure at 300 K temperature (surface view of the nanoparticles). Simulation box is shown as green lines around the particle. Inner arrows show the extra side lengths equivalent to 2 nm in each direction. 26

Figure 3.3: Left) Illustration of an atomic layer at a radial distance, r, on the nanoparticle. Layer thickness, dr is 0.25 Å. Right) Illustration of surface and core region. 27

Figure 3.4: Particle-wide average dynamic MSD vs. temperature for different sizes of gold nanoparticles from real-space calculations (Error bars are standard deviations from the mean)..... 28

Figure 3.5: a) Particle-wide average lattice parameter vs. temperature, b) rms strain vs. temperature..... 31

Figure 3.6: Left) 3D illustration of a 5 nm ideal crystalline nanoparticle model. Right) The distribution of atoms on the midplane intersecting the 3D particle model. Red and blue arrows represent one of the shortest (Min) and longest (Max) diameters, respectively; while the Mean diameter indicates the average diameter. 33

Figure 3.7: Temperature dependence of the Min, Max and Mean diameters computed from gold nanoparticles with nominal sizes of 5, 10, 15, 20 and 30 nm. Error bars of Mean diameters refer to the standard deviations... 34

Figure 4.1: Rietveld refinement result of the diffraction profile of 5-nm-diameter gold nanoparticle at 300 K. The inset shows the observed and calculated (refined) intensities from 100° to 150°. TDS indicates the thermal diffuse scattering, which was subtracted before refinement. 48

Figure 4.2: Temperature (a-e) and particle size dependence (f-i) of lattice parameters obtained from real-space and diffraction analyses. 50

Figure 4.3: (a-b) Local variation of average lattice parameters within concentric shell volumes with respect to their distance from the particle center. The areas shaded in red indicate surface thickness. (c-f) Average lattice parameters over the particle volume (red), over the core volume (green) and over the outermost surface layer (blue) with respect to the nominal particle size at 10, 100, 200 and 300 K. Stars shown in black refer to Rietveld-refined lattice parameters..... 53

Figure 4.4: Thermal strain vs. temperature obtained from real-space calculations using average lattice parameter (red markers), average particle diameter (blue markers), and from Rietveld refinement using average lattice parameter (orange markers) for 5 nm, 10 nm, 15 nm, 20 nm, and 30 nm nanoparticles and bulk gold crystal (5 nm). Dashed lines are linear fits..... 54

Figure 4.5: a) CTE vs. nanoparticle size based on average lattice parameters and diameters from real-space calculations (MD) and Rietveld analysis (100-300 K). Error bars refer to fitting errors of the slopes for MD-based calculations (obtained from Figure 4.4). b) MD-based average CTEs computed from mean lattice parameters for different reference temperatures. 55

Figure 4.6: Root-mean-square (rms) strain vs. temperature for a) 5 nm, b) 10 nm, c) 15 nm, d) 20 nm, and e) 30 nm diameter gold nanocrystals (empty circles show rms strains computed at 0 K) and rms strain vs particle diameter at f) 10 K, g) 100 K, h) 200 K and i) 300 K obtained from real-space analysis and Rietveld refinement of snapshot intensities. (error bars are within marker size in Rietveld refinement). 58

Figure 4.7: Local (discrete markers) and particle-averaged rms strains (solid lines) obtained by real-space calculations for the gold nanocrystals with a) 5 nm, b) 10 nm, c) 15 nm, d) 20 nm, e) 30 nm diameters and f) bulk crystal model (5 nm) at 4 different temperatures between 10 and 300 K. Dashed lines are Rietveld-refined rms strains. 60

Figure 4.8: MSD vs. temperature for a) 5 nm, b) 10 nm, c) 15 nm, d) 20 nm, and e) 30 nm diameter gold nanocrystals and MSD vs. particle diameter at f) 10 K, g) 100 K, h) 200 K and i) 300 K temperature obtained from real-space and Rietveld refinement analyses. Error bar results indicate standard deviations in real-space calculations and fitting errors in Rietveld refinement. 61

Figure 4.9: a-b) Radial change of MSD at 300 K for 5 and 10 nm particles, respectively. The colored region is the surface region with a thickness of 10 Å. c-f) Size-dependent change of real-space and Rietveld MSD at temperature range 10-300 K. Definitions of each data are given throughout the text. 64

Figure 5.1: Left) PDF of 5 nm nanocrystal at 300 K obtained from the MD simulation. The inset figure shows the 5 nm nanocrystal within the MD box. Gold atoms are colored orange. The particle diameter is illustrated with a blue line inside the simulation box. Right) 3 FCC unit cells of crystal gold structure are shown. In each unit cell, a red arrow is drawn to illustrate interatomic distance. These three interatomic distances correspond to red vertical dashed lines shown in the PDF figure. 69

Figure 5.2: First 3 PDF peaks of 5 nm nanocrystal at 100 K, 200 K, and 300 K temperatures obtained from the MD simulations. Note that peaks get broader with increasing temperature, indicating increased thermal disorder. 70

Figure 5.3: Simulated powder diffraction data for finite-sized a) 5 nm and b) 30 nm diameter gold nanocrystals at 0 and 300 K. The insets show the intensities over the range of $25° < 2\theta < 50°$ and the assumed wavelength of X-rays is 0.21 Å. Note that the Bragg peaks at higher scattering angles disappear at 300 K due to the Debye-Waller factor. 73

Figure 5.4: Normalized (by Q_{max}) Fourier transform of the window function, at two different Q_{max}: $8\,\text{Å}^{-1}$ (blue line) and $50\,\text{Å}^{-1}$ (red line). 77

Figure 5.5: *Top*) Ideal or unconvoluted PDF, *Middle*) convoluted PDF with the Fourier transform of the window function of Q_{max}: $8\,\text{Å}^{-1}$, and *Bottom*) Q_{max}: $50\,\text{Å}^{-1}$. The ideal PDF was generated artificially at given r positions with constant peak width being equal to $\sqrt{2MSD}$ where MSD is room temperature (300 K) MSD of 5 nm finite-sized particle (see the caption of top figure for exact MSD). Peak heights are randomly scaled to imitate real PDF. Note that, MSD is fixed, only Q_{max} changes between middle and bottom PDF. 79

Figure 5.6: Effect of peak width (or MSD) on convoluted PDF for a fixed Q_{max}. Only *r* up to 15 Å is shown for clarity. Similarly, PDF data is artificially generated as in Figure 5.5. *Top left*) Ideal PDF at 10 K, and *Top right*) Convoluted PDF with Q_{max}: $26\,\text{Å}^{-1}$. *Bottom left*) Ideal PDF at 300 K, and *Bottom right*) Convoluted PDF with Q_{max}: $26\,\text{Å}^{-1}$. Note that, Q_{max} is fixed, only MSD changes between top and bottom PDFs.. 80

Figure 5.7: Variation in refined lattice parameters (a-d), MSD (e-h) and crystallite size (i-l) from PDF analysis with respect to the angular range and step size of the diffraction data from a single snapshot of atomic coordinates. Each subfigure depicts the variations for 5 nm truncated-bulk or finite-sized nanocrystal model at 0 or 300 K indicated in the title. Values on each window report the refined parameter values corresponding to the step size and angular range selected in this study (left) and for $2\theta_{\max} = 180°$. 82

Figure 5.8: PDF refinement of diffraction data simulated from 5 nm truncated-bulk and finite-sized spherical gold nanocrystals at 300 K. Blue markers indicate the PDF data evaluated from Fourier transforming the diffraction data while the red plots indicate the fitted PDFs by Diffpy-CMI. Peak widths were refined by δ_1. 84

Figure 5.9: PDF refinement of diffraction data simulated from 5 nm truncated-bulk and finite-sized spherical gold nanocrystals at 300 K over the mid-r range (4 Å < r < 30 Å). Blue markers indicate the PDF data evaluated from Fourier transforming the diffraction data while the red markers indicate the fitted PDFs by DiffpyCMI. Peak widths were refined by δ_1..... 85

Figure 5.10: PDF refinement of diffraction data simulated from 5 nm truncated-bulk and finite-sized spherical gold nanocrystals at 300 K. Blue markers indicate the PDF data evaluated from Fourier transforming the diffraction data after thermal diffuse scattering intensity is subtracted while the red plots indicate the fitted PDFs by DiffpyCMI. Peak widths were refined by δ_1..... 86

Figure 5.11: Average lattice parameters with respect to temperature calculated from atomic coordinates (Real) and extracted by PDF (PDF) and Rietveld refinement (Rietveld) of the corresponding diffraction data are shown for *a*) 5 nm truncated-bulk crystal and *b-f*) 5-30 nm finite-sized nanocrystals. The peak-width parameter selected during PDF refinement is δ_1... 88

Figure 5.12: Real space calculations of core, surface and particle-wide average lattice parameters of finite-sized gold nanocrystals with respect to crystal size at *a*) 0 K and *b*) 300 K. 91

Figure 5.13: *a*) First three peaks of $G_{forward,Snapshot}$ from 5 nm finite-sized gold nanocrystal. 5000 snapshot coordinates were used to compute the PDF peaks. The fitted Gaussian function is shown as a red line. *b*) $G_{forward,Static}$ of 5 nm finite-sized, static gold nanocrystal model at 300 K. Fitted Gaussian function is shown as a red line. The inset shows the third PDF peak centered at around 5 Å. *c*) Difference between lattice parameters from the snapshot and static $G_{forward}$ as a function of peak position. The dashed black line at 0 is added as a reference, whereas a red solid horizontal line passing from -0.00214 Å shows the lattice parameter differences between PDF-refined snapshot and static intensities of 5 nm finite-sized nanocrystal at 300 K. Fluctuations at high *r* are due to poor fits on diminished PDF peaks. *d*) Skewness distribution of $G_{forward}$ from the snapshot (blue) and static (red) coordinates of finite-sized 5 nm gold nanocrystal at 300 K.. 94

Figure 5.14: Average *a*) dynamic, *b*) static and *c*) total MSD as a function of radial distance from the particle center computed over spherical shell volumes (with 0.125 Å thickness) at 0 and 300 K for finite-sized 10 nm gold nanocrystal..... 95

Figure 5.15: Mean and maximum crystallite sizes over 0-300 K calculated in real space and refined from PDF analysis are shown for *a*) truncated-bulk (5 nm) and *b-f*) 5-30 nm finite-size nanocrystals. The peak-width parameter selected in PDF refinement is δ_1..... 96

Figure 5.16: Dynamic MSD vs. temperature calculated from atomic coordinates (Real), PDF refinement (PDF) and Rietveld refinement of diffraction data for a) 5 nm truncated-bulk crystal and b-f) 5-30 nm finite-sized nanocrystals. PDF-nodelta indicates the refinement result with no peak sharpening factor. A fifth-order Chebyshev polynomial was used to subtract thermal diffuse scattering during Rietveld refinement..... 99

Figure 5.17: PDF-refined MSDs obtained by δ_1 from finite-sized nanocrystals with respect to crystal size (error bars reported from DiffpyCMI) along with real space calculations of core, surface and particle-wide averaged a) dynamic displacements at 0 K, b) static displacements at 0 K, c) dynamic displacements at 300 K, d) combined dynamic and static displacements at 300 K..... 101

Figure 5.18: Particle size and temperature dependent deviation of PDF-refined a) particle-averaged lattice parameters, b) core lattice parameters, c) particle-averaged MSDs, d) core MSDs, e) crystallite size from real space calculations..... 106

Figure 6.1: Simulated diffraction intensity of 15 nm gold nanoparticle at room temperature. The dashed vertical line is the upper limit for our lab X-ray diffractometer. Wavelength corresponds to 0.21 Å. 108

Figure 6.2: Top left) Measuring the 100 mg of powder in the lab, top middle) sealed glass bottle containing the powder and cleaned sample holder - "zero-background", right) poured powder on the sample holder, bottom left) XRD measurement in reflection geometry with Bruker D8 DISCOVER diffractometer (with Cu tube) in the OzUBEX. 109

Figure 6.3: PXRD pattern of gold nanoparticle with background intensity for 50 and 100 mg of powder sample. The amount of sample has a negligible effect on measured data..... 110

Figure 6.4: Measured PXRD pattern (background subtracted and polarization corrected) of gold nanoparticle as a function of diffraction vector magnitude. Other corrections such as smoothening and $\mathrm{K}\alpha_2$ stripping were applied with the QualX software [78]. 111

Figure 6.5: PDF pattern of gold nanoparticle obtained by Fourier transformation using the measured intensity shown in Figure 6.4. Note that particle size is obtained as 150 Å, which is the position in the x-axis of the PDF plot beyond which no significant peaks exist. 112

Figure 6.6: Unit cell model for FCC gold structure is shown. Red arrows show the first 10 interatomic distances between atom pairs. In case of distances exceeding one unit cell, a second unit cell is added with a blue plane separating two unit cells. 113

Figure 6.7: Measured PDF pattern of gold nanoparticle. Only r-range up to 15 Å is shown. The first 10 vertical dashed lines correspond to atomic pairs shown inside FCC unit cell as illustrated in Figure 6.6. 114

Figure 6.8: Simulated PDF pattern of gold nanoparticle obtained at two different Q_{max}: 8.08 Å^{-1} and 21 Å^{-1}. Peaks are broadened at low Q, and some of the peaks are lost. 114

Figure 6.9: Comparison of fit quality between the measured and calculated PDF from ACM modeling. The difference between the two PDFs is shifted below for clarity and shown as green line. Fitting range was between 0-150 Å. For clarity, r-range is divided into three ranges: a) low-r range (0-50 Å), b) mid-r range (50-100 Å), c) high-r range (100-150 Å). Note the disagreement at the high-r range. 117

Figure 6.10: PDFs for particles used in polydispersed system. The particle sizes are 5, 10, 15, 20, and 30 nm. 119

Figure 6.11: Lattice parameter - MSD space of polydispersed systems. Each point in the contour plot is a polydispersed system and is colored based on agreement factor Rw. The smaller Rw is, the better the agreement between the calculated PDF and measured PDF. The polydispersed system is composed of 5, 10, 15, 20, and 30 nm diameter gold nanocrystals. 120

Figure 6.12: Size distribution in polydispersed system as obtained from MD-assisted PDF modeling. 121

Figure 6.13: Comparison of fit quality between the measured and calculated PDF from MD-assisted polydisperse modeling. The difference between the two PDFs is shifted below for clarity and shown as green line. Fitting range was between 0-150 Å. For clarity, r-range is divided into three ranges: a) low-r range (0-50 Å), b) mid-r range (50-100 Å), c) high-r range (100-150 Å). Note the improved agreement at the high-r range compared to that of ACM modeling shown in Figure 6.9. . 122

Figure 6.14: SE-STEM images of the gold powder sample. 123

Figure 6.15: Top figure, from left to right: electron image of the nanocrystal region, mapped elements with EDX in the selected region, only gold element is mapped in the selected region. Bottom figure: EDX map. The Cu signal comes from the copper gird used in the TEM. 123

Figure 6.16: From left to right: TEM, HRTEM, lattice planes, and FFT of the selected region. 124

LIST OF ACRONYMS AND ABBREVIATIONS

ACM	Attenuated Crystal Modeling
ADP	Atomic Displacement Parameter
BCDI	Bragg Coherent Diffraction Imaging
CIF	Crystallographic Information File
CN	Coordination Number
CTE	Coefficient of Thermal Expansion
DFT	Density Functional Theory
DSE	Debye Scattering Equation
EAM	Embedded Atom Method
EDX	Energy Dispersive X-ray Spectroscopy
FCC	Face-Centered Cubic
FWHM	Full Width at Half Maximum
HPC	High Performance Computing Center
HRTEM	High-Resolution Transmission Electron Microscopy
JCPDS	Joint Committee on Powder Diffraction Standards
LAMMPS	Large-scale Atomic/Molecular Massively Parallel Simulator
LDA	Local-Density Approximation
MD	Molecular Dynamics
MEAM	Modified Embedded-Atom Method
ML	Machine Learning

MSD	Mean Square Displacement
PDF	Pair Distribution Function
PXRD	Powder X-ray Diffraction
rPBE	Revised Perdew-Burke-Ernzerhof
RMC	Reverse Monte Carlo
SEM	Scanning Electron Microscopy
SE-STEM	Secondary Electron Scanning Transmission Electron Microscopy
SRM	Standard Reference Material
TDS	Thermal Diffuse Scattering
TEM	Transmission Electron Microscopy

1. INTRODUCTION

Diffraction analysis is a non-destructive structure characterization technique used widely in material science. The sample is irradiated with an incoming X-ray beam, and its scattered intensity is detected by an X-ray detector. The measured X-ray diffraction pattern is then analyzed with computer programs to know about the phases and structures of the material. In general, diffraction experiments are performed in one of two ways depending on the sample. If the sample is a large single crystal, then single X-ray diffraction is used. However, synthesizing such crystals is difficult due to the requirement of a controlled environment in experiments. On the other hand, most samples can be synthesized in powder form consisting of crystalline grains. In this case, the powder X-ray diffraction method is used. This thesis also uses the powder X-ray diffraction method for nanocrystals. Powder diffraction analysis is a reliable technique in structural characterization since it provides volume-averaged properties of all grains in powder. Examples of other structural characterization techniques are Bragg Coherent Diffraction Imaging (BCDI), Transmission Electron Microscopy (TEM), and Scanning Electron Microscopy (SEM). They are categorized as local techniques since they visualize only a small number of grains in the powder.

Currently, powder diffraction analysis of nanocrystals can be done in two different ways: Rietveld analysis and Pair Distribution Function (PDF) analysis. In the Rietveld analysis algorithm, a unit cell model is built, and its structure properties, such as lattice parameter, thermal displacement parameter, and atomic positions, are refined against measured diffraction data. The methodology used to calculate diffraction data from the unit cell model is similar to what we will explain as the unit cell summation method in Chapter 2. In both, a critical function is the structure factor, even though the profile function is defined to include size and strain effects in the Rietveld analysis. Similarly, diffraction analysis can be done in real space with a PDF refinement algorithm. Again, the unit cell

model is built in PDF refinement, and its structural parameters are refined against measured PDF. This type of modeling is called small-box modeling in the PDF community. Even though there are more sophisticated methods, such as big-box modeling, which uses the Reverse Monte Carlo (RMC) algorithm by building a large box of atoms and moving their positions to match with measured PDF, we will not use it in this thesis since it is out of scope of the thesis. Moreover, the computational demand is relatively high compared to small-box modeling.

Unit cell modeling strategy, implemented in diffraction analysis software, works best for crystalline structures with the same atomic environments everywhere within the structure. In the case of realistic nanocrystals, atomic environments differ in core and surface regions. While atoms in the core region of nanocrystal have their neighbor atoms in place, surface atoms have missing neighbors. This causes surface atoms to behave differently than core atoms. As a result, local variation of properties emerges, resulting in different unit cells at both surface and core. For example, atoms at the surface have more kinetic energy, and they are more dynamic compared to core atoms. Similarly, bond lengths at the surface become shorter compared to the core region that has a similar bond length as that of bulk structure. Under these circumstances, it is not clear whether refined structural parameters represent average properties within the core region, surface region, or particle when unit cell refinement methodology is applied to realistic nanocrystals. Hence, the interpretation of the extracted parameters becomes complex. Still, both Rietveld refinement and PDF refinement methodologies are commonly used for diffraction analysis of nanomaterials in the literature. However, the reliability of the refined parameters is not quantitatively resolved yet, making the main motivation of this thesis.

Several studies have been done about the applicability of diffraction analysis in nanocrystals. The problem is also known as nanodiffraction problem. Preliminary work about the subject was done by Palosz group [1]. They conducted a computational X-ray

diffraction study of SiC nanocrystals. Rietveld analysis was applied to the ideal nanocrystal to extract lattice parameters. Their results showed that the calculated lattice parameter from the Rietveld analysis deviated from the true lattice parameter of the ideal nanocrystal. Moreover, the deviation was size-dependent and can be ignored for particles over 10 nm. The authors mentioned that the primary reason for the deviation was the incompatibility of infinite atomic planes assumed in the Rietveld algorithm compared to the finite size of real particles. In the diffraction analysis of nanocrystals, they suggested the usage of the "apparent lattice parameter", which is reflection dependent lattice parameter. At high diffraction vectors, they observed convergence of the apparent lattice parameter to the real space lattice parameter of the nanocrystal. Another similar computational study was conducted by the Noyan group for both ideal and energy-minimized gold nanocrystals with a size range between 3.3 and 40 nm at 0 K [2, 3]. They generated X-ray diffraction data using the Debye Scattering Equation (DSE) and then applied Rietveld analysis to extract lattice parameters. The extracted lattice parameters showed particle size-dependent deviations from true lattice parameters. Moreover, deviations became significant for particle sizes as small as 5 nm in diameter. In addition, their real-space analysis showed that lattice strains were distributed heterogeneously along the radial directions at 0 K. Most of the strains, resulting from static atomic displacements towards the particle center, were concentrated at the surface region of gold nanocrystal. However, lattice strains calculated from Rietveld analysis significantly underestimated real-space average lattice strain. Their results also supported the results of the Palosz group.

An alternative to Rietveld analysis is the PDF analysis of diffraction data of nanocrystals using the small-box methodology, also known as the "real-space Rietveld" method. PDF data is obtained by Fourier transformation of diffraction data, resulting in real-space from reciprocal-space. To the best of our knowledge, there is no detailed analysis of the accuracy of refined structural parameters from PDF refinement of nanocrystals. In 2024,

the Billinge group developed a fast and robust small-box PDF refinement workflow to extract morphology, phase and size distributions, lattice parameters, and atomic displacement parameters from the measured PDF data of TiO_2 nanoparticles synthesized at different temperatures [4]. Validation of these results is difficult since there are both sample and instrument-related complexities in real experiments. The former includes defects, texture (preferred orientation of grains in powder), and polydispersity in phase, shape, and size of nanoparticles, which increases the number of refinable parameters. This might result in fitting problems such as overfitting and underfitting. The instrument-related complexities might include instrument-related resolution due to the optics of diffractometers. The instrument resolution results in additional r-dependent peak broadening in PDF peaks, which is not always easy to measure accurately. However, ideal experimental conditions are necessary to validate the calculated structural parameters. In an ideal experiment, first, we can avoid instrument resolution problems; second, we are able to control all of the mentioned parameters and change one variable at a time to see its effect on results. We can create such a condition with computer simulations, as explained in this thesis.

In this thesis, we developed a workflow to quantify expected errors from diffraction analysis of realistic nanocrystals. First, molecular dynamics simulation methodology is built to obtain an atomic model of realistic nanocrystals with different sizes at different temperatures. Second, structural properties such as lattice parameter, Atomic Displacement Parameter (ADP), and particle size are calculated from the atomic model. The former two properties are calculated locally, i.e., radial change of property from particle center to surface. Third, diffraction data is calculated from the atomic model. Fourth, Rietveld and PDF refinements using a unit cell model are performed on diffraction data of realistic nanocrystals. From these analyses, structural parameters (lattice parameter, ADP, and particle size) are extracted. Finally, the accuracy of the extracted structural parameters is evaluated against both known local and average properties from an atomic model

of realistic nanocrystals at different sizes and temperatures. In some parts, a comparison between Rietveld and PDF methods was done.

Structure of the Thesis

In Chapter 2, we will provide theoretical background related to diffraction analysis of nanocrystals. Derivations will start with scattering by free electron and end with scattering by small crystal. Assumptions used in derivation will be explained as well. In Chapter 3, we will explain our Molecular Dynamics (MD) methodology used to create realistic nanocrystals at different temperatures. In addition, particle types (snapshot and static), calculation of structural parameters, force-field validation, and diffraction data calculation will be given. In Chapter 4, the Rietveld algorithm, analysis methodology, and correlation of extracted structural parameters with true structural parameters will be explained. In Chapter 5, PDF analysis will be explained in a similar way to Rietveld analysis. Especially the effect of finite Q_{max} on PDF profile and refinement results will be discussed along with its relationship with temperature. At some parts, Rietveld-PDF comparisons will be done. In Chapter 6, we performed PDF analysis on experimentally measured PDF of 14 nm gold nanocrystal. Challenges due to low Q_{max} provided by lab diffractometer will be explained. Also, we will show that polydispersed systems obtained from MD simulation can increase fit quality, resulting in reliable Mean Square Displacement (MSD) compared to Attenuated Crystal Modeling (ACM).

2. THEORETICAL BACKGROUND

2.1 Introduction

In this chapter, we are going to derive the necessary relations to calculate the intensity scattered from the irradiated material. First, we will start explaining scattering by free electron, then by an atom, and finally, by small crystal. Derivation of equations is based on the kinematic regime of X-ray diffraction. In this regime, it is assumed that the incoming primary beam is scattered once along its path in the crystal structure, avoiding multiple scattering events. Moreover, scattered beams and incoming primary beams do not interact with each other. The kinematic regime is applicable in the case of small coherent volumes of structures such as nanocrystals. There is not enough space in nanocrystals for multiple scattering events to occur. On the other hand, the dynamic regime of X-ray diffraction is more accurate for bulk crystals, in which multiple scattering is expected. Since we study diffraction analysis of nanocrystals, we used a kinematic regime.

In the derivation of intensity, we also assumed the plane-wave approximation of beams. This treatment allows us to derive scattered fields in terms of total path lengths expressed using a scatterer position vector and momentum transfer vector. In order for the plane-wave approximation to be applicable, both the distance between the X-ray source and irradiated sample, and sample and detector should be long enough compared to irradiated sample size. If this condition is satisfied, then both incoming beams at the irradiated sample and scattered beams at the detector position are parallel to each other.

Scattered intensity from small crystal can be calculated using two different approaches, which are full atomistic summation of electric fields and unit cell summation of electric fields. While the former method assumes no periodicity in structure, the latter requires perfect crystal with repeating unit cells. The full atomistic summation method is

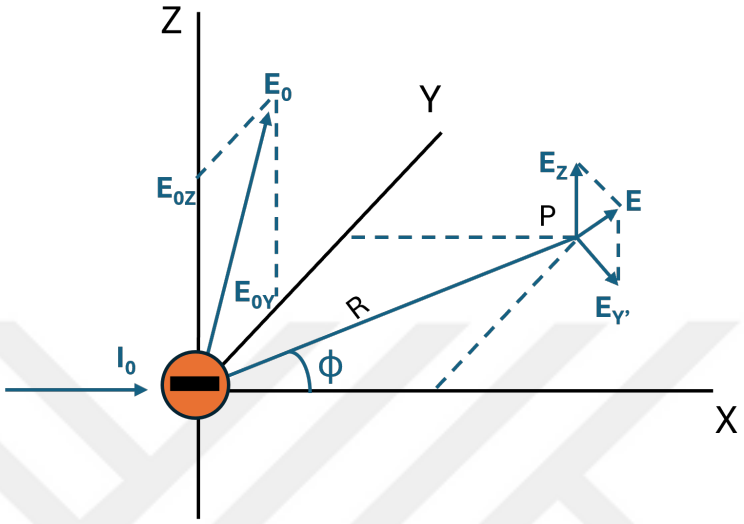
considered superior to the unit cell method since it can be used to model both crystalline and non-crystalline materials. The net scattered electric field from the whole structure is obtained by summing fields from each atom. Therefore, accurate calculation of intensity from the realistic nanocrystals, in which local variation of structural properties exists, is possible with this method. However, intensity calculation has a high computational demand. For example, computation time scales with N^2 for a structure with N atoms since the distance between each atomic pair is evaluated. Therefore, the method is limited to very small nanomaterials in application. On the other hand, the unit cell summation method is commonly used in X-ray diffraction analysis, and it is relatively fast. In this method, the structure factor is defined for scattering from the single unit cell that represents the whole crystal structure. The calculation is fast since the number of atoms in a single unit cell is relatively small. However, this method assumes the particle is crystal, and it works best for crystal structures. Now, the question we want to answer is: can we apply the unit cell method in diffraction analysis of nanocrystals? Realistic nanocrystals are not perfect crystal due to surface and core regions having different unit cells.

2.2 Scattering by Free Electron

When X-rays interact with electron, an electric field exerts force on the electron, causing its acceleration. An accelerated electron radiates scattered waves. The scattering can occur in two different ways: unmodified and modified scattering. While a scattered wave has the same wavelength as the primary beam in unmodified scattering, the wavelength can be larger in the latter one due to some portion of the energy of the primary beam being absorbed by an electron. In X-ray studies of materials, unmodified scattering is the one that gives rise to Bragg reflections used in structural determination. Therefore, we will derive fundamental equations to find the intensity of scattered radiation due to unmodified scattering by an electron, atom, and small crystal at some observation point,

which is an X-ray detector used in experiments. We will use classical wave treatment.

Figure 2.1: *Unpolarized primary X-ray beam propagating in X-direction is scattered by free electron, causing electric field at observation point P in XY-plane.*



Unpolarized primary beam is directed toward *X*-direction at an electron at point *O* in Figure 2.1. Since the primary beam is unpolarized, its electric vector can take any direction in *YZ* plane. One such direction is shown as $\mathbf{E}_0$, with its components E_{0Y} and E_{0Z}, in *Y* and *Z* directions, respectively. Instantaneous electric field in *Y* and *Z* directions is given as:

$$\epsilon_{0Y} = E_{0Y} \sin 2\pi\nu t, \quad \epsilon_{0Z} = E_{0Z} \sin 2\pi\nu t$$

The ϵ_{0Y} causes electron acceleration in *Y*-dir as:

$$a_Y = \frac{f_Y}{m} = \frac{eE_{0Y}}{m} \sin 2\pi\upsilon t$$

where *e* and *m* are the charge and mass of the electron. An accelerated charge radiates, causing an electric field. This electric field along Y'-direction at point *P* can be expressed according to classical electromagnetic theory as:

$$\epsilon_{Y'} = E_{Y'} \sin 2\pi\upsilon t$$

where an amplitude is given by

$$E_{Y'} = \frac{e^2 E_{0Y}}{mc^2 R} \cos\phi$$

where *c* is velocity of light. Similarly, E_Z component is given as:

$$E_Z = \frac{e^2 E_{0Z}}{mc^2 R}$$

Then, resultant amplitude at point *P* becomes:

$$E^2 = E_Z^2 + E_{Y'}^2 = \frac{e^4}{m^2 c^4 R^2} \left(E_{0Z}^2 + E_{0Y}^2 \cos^2\phi \right)$$

$\mathbf{E}_0$ can take all orientations in the *YZ*-plane with equal probability. Also, *Y*- and *Z*-axes are equivalent, leading to $\langle E_{0Y}^2 \rangle = \langle E_{0Z}^2 \rangle = \frac{1}{2} \langle E_0^2 \rangle$. After orientational averaging, above equation becomes:

$$\left\langle E^2 \right\rangle = \left\langle E_0^2 \right\rangle \frac{e^4}{m^2 c^4 R^2} \left(\frac{1 + \cos^2\phi}{2} \right). \tag{2.1}$$

Experimentally, we observe intensity, which is energy per unit area per unit time. It is related to $\langle E^2 \rangle$ as

$$I = \frac{c}{8\pi} \left\langle E^2 \right\rangle \tag{2.2}$$

By inserting (2.1) into (2.2), we obtain intensity of classical scattering by a single free electron. This intensity is also called Thomson scattering, and given as:

$$I_e = I_0 \frac{e^4}{m^2 c^4 R^2} \left(\frac{1 + \cos^2\phi}{2} \right) \tag{2.3}$$

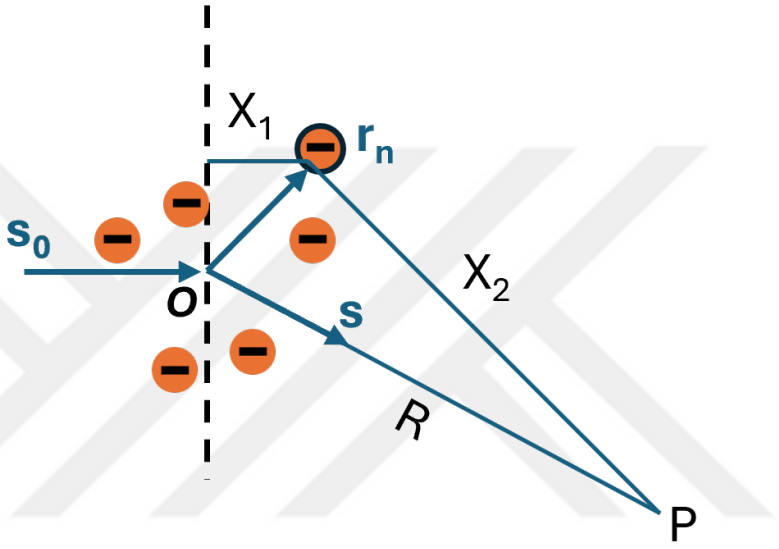
where last factor with parenthesis is a polarization factor for unpolarized beam.

2.3 Scattering by Single Atom

Consider the classical scattering from a group of electrons confined to a small volume, such as the volume of an atom. The primary beam, with amplitude E_0, is polarized and directed toward point *O* along unit vector $\mathbf{s}_0$. E_0 has a direction normal to the plane

of the page. Electrons of atom are localized around point *O*, with the position of each electron $\mathbf{r}_n$. The detector is placed at point *P*, that is *R* distance away from the atom at *O* with unit vector $\mathbf{s}$ pointing towards point *P*. We want to find the scattered intensity that is recorded on the detector at point *P* as illustrated in Figure 2.2.

Figure 2.2: *Polarized primary X-ray beam propagating along* $\mathbf{s}_0$ *vector is scattered by a cluster of electrons around atom at origin O, causing electric field at observation point P.*



Instantaneous value of electric field of primary beam at $\mathbf{r}_n$ can be expressed in terms of a wave front through *O* as:

$$\epsilon_0 = E_0 \cos\left(2\pi\nu t - \frac{2\pi X_1}{\lambda}\right) \tag{2.4}$$

An electric field of the scattered wave at point *P* due to accelerated electron can be obtained by multiplying the above relation with classical factor and considering the total free path, $X_1 + X_2$, as:

$$\epsilon_e = \frac{E_0 e^2}{mc^2 X_2} \cos\left[2\pi\nu t - \frac{2\pi}{\lambda}(X_1 + X_2)\right] \tag{2.5}$$

Note that there is an additional π phase shift in scattered waves, but it is ignored in the above relation since it is constant for all scatterers. Assuming both the source of primary

beam and observation point for scattered wave are far away than length $|\mathbf{r}_n|$, plane wave approximation can be used as $X_1 \rightarrow$ R in denominator, and $X_1 + X_2 \rightarrow (\mathbf{r}_n \cdot \mathbf{s}_0) + (R - \mathbf{r}_n \cdot \mathbf{s}) = R - (\mathbf{s} - \mathbf{s}_0) \cdot \mathbf{r}_n$ in cosine term. A sum of the instantaneous fields at *P*, expressed in terms of the complex exponential, is then given by:

$$\epsilon_a = \frac{E_0 e^2}{mc^2 R} e^{2\pi i[vt-(R/\lambda)]} \sum_n e^{(2\pi i/\lambda)(\mathbf{s}-\mathbf{s}_0)\cdot\mathbf{r}_n} \tag{2.6}$$

We consider each electron as a cloud of negative charge rather than a single point. The electron cloud is characterized by charge density ρ. The amount of charge in volume element dV can be expressed as ρdV, such that $\int \rho dV = 1$ for each electron. The instantaneous value of an electric field for unmodified scattering by one electron can be obtained by replacing summation over $\mathbf{r}_n$ in (2.6) with integration over charge element ρdV as:

$$\epsilon_e = \frac{E_0 e^2}{mc^2 R} e^{2\pi i[vt-(R/\lambda)]} \int e^{(2\pi i/\lambda)(\mathbf{s}-\mathbf{s}_0)\cdot\mathbf{r}_n} \rho dV \tag{2.7}$$

where the quantity in integral is called the scattering factor per electron and defined as:

$$f_e = \int e^{(2\pi i/\lambda)(\mathbf{s}-\mathbf{s}_0)\cdot\mathbf{r}_n} \rho dV \tag{2.8}$$

If we assume spherical symmetry for charge distribution, the above equation is evaluated into the following:

$$f_e = \int_0^\infty 4\pi r^2 \rho(r) \frac{\sin kr}{kr} dr, \quad k = \frac{4\pi \sin\theta}{\lambda} \tag{2.9}$$

where $\rho(r)$ is the radial dependence of electron density. For an atom containing *n* electrons, the sum over f_e for each electron in an atom results in atomic scattering factor, *f*, as:

$$f = \sum_n f_{en} = \sum_n \int_0^\infty 4\pi r^2 \rho_n(r) \frac{\sin kr}{kr} dr \tag{2.10}$$

At small values of *k*, the atomic scattering factor approaches to the total number of electrons *Z* in an atom as:

$$\sum_n \int_0^\infty 4\pi r^2 \rho_n(r) dr = Z$$

If the X-ray wavelength is much smaller than any of the absorption edge wavelengths in the atom, a dispersion correction is necessary, which can be expressed as:

$$f = f_0 + \Delta f' + i\Delta f'' \tag{2.11}$$

where $\Delta f'$ and $\Delta f''$ are the real and imaginary parts of the dispersion correction. The angular dependence of $\Delta f'$ and $\Delta f''$ is much smaller than f_0.

We can re-write (2.6) by replacing summation part with (2.10) as:

$$\epsilon_a = \frac{E_0 e^2}{mc^2 R} e^{2\pi i[vt-(R/\lambda)]} f \tag{2.12}$$

By multiplying ϵ_a with its conjugate complex ϵ_a^*, we get E^2 as:

$$\epsilon_a \epsilon_a^* = E^2 = \frac{E_0^2 e^4}{m^2 c^4 R^2} f^2 \tag{2.13}$$

If both sides are multiplied with $c/8\pi$, the scattered intensity from a single atom is obtained as:

$$I_a = \frac{c}{8\pi} E^2 = \left(\frac{c E_0^2 e^4}{8\pi m^2 c^4 R^2} \right) f^2 \tag{2.14}$$

Noting $I_0 = \frac{c}{8\pi} E_0^2$, the first factor in (2.14) is the same as (2.3) (intensity scattered by single free electron) without polarization factor. Hence, the above equation can be written simply as: $I_a = I_e f^2$

2.4 Scattering by Small Crystal

In general, the scattered intensity from small crystal can be calculated with two different approaches: a local and global approach. The local approach performs discrete summation over scattering centers that can be either atom or unit cells. In contrast, the global approach assumes that a small crystal is composed of continuous electron density; hence, crystal region can be found by multiplying infinitely continuous electron density function with particle shape function. The Fourier transform of particle electron density

is related to its scattering amplitude in the far-field region. The method is also called the Patterson formulation. In this study, we will not use the global approach; however, its comparison with local approaches for cubic particles was given by Öztürk [5]. Below, we will find the scattered intensity using two types of local methods: atomic summation and unit cell summation methods. The atomic summation assumes no periodicity in crystal structure since it calculates the instantaneous scattered electric field of the whole particle by summing over the instantaneous scattered electric field of each atom in the particle. Thus, it can be applied to both crystal and amorphous structures. On the other hand, the unit cell summation is based on the assumption that the structure is composed of repeating unit cells; hence, summation over all atoms in a crystal reduces to only summation over atoms in a single unit cell. Thus, the unit cell summation works best for crystal structures.

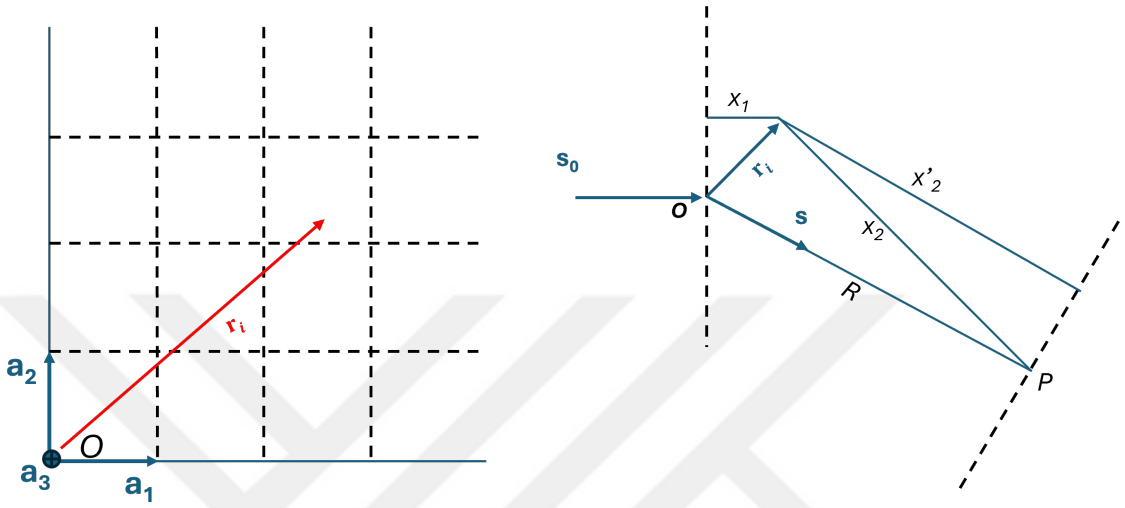
2.4.1 Atomic Summation

Plane polarized beam propagating in unit vector $\mathbf{s}_0$ direction, with electric field normal to the plane of the paper, falls on a small single crystal as illustrated in Figure 2.3 (left). We want to find scattered intensity at observation *P* that is *R* distance away from the crystal origin *O* in scattering direction $\mathbf{s}$. Atom coordinate for i^{th} atom in crystal is indicated with $\mathbf{r}_i$ vector.

For simplicity, we assume that the small crystal has the shape of a parallelopipedon. Moreover, the distance between the beam source and crystal, and between crystal and observation point, is large enough compared to crystal size so that plane-wave approximation can be applied. The instantaneous electric field at observation point *P* due to unmodified scattering from i^{th} atom in crystal is given in terms of total path length from wavefront at origin *O* to observation point *P* (see Figure 2.3 (right)) as:

$$\epsilon_p = \frac{E_0 e^2}{mc^2 R} f_n \cos\left[2\pi\nu t - \frac{2\pi}{\lambda}\left(x_1 + x_2\right)\right] \tag{2.15}$$

Figure 2.3: *Left) Small crystal is illustrated with cubic unit cells shown as dashed lines on* $\mathbf{a}_1\mathbf{a}_2$ *face. Atomic coordinate vector for* i^{th} *atom in the crystal is shown with* $\mathbf{r}_i$ *vector. Right) Diffraction geometry of the small crystal shown at left.* $\mathbf{s}$ *and* $\mathbf{s}_0$ *are primary and scattered beam directions, respectively. P is the detector position that is R distance away from crystal origin.*



The plane-wave approximation expresses the total path length as:

$$(x_1 + x_2) \rightarrow (x_1 + x_2') = [(\mathbf{r_i} \cdot \mathbf{s}_0) + (R - \mathbf{r_i} \cdot \mathbf{s})] = R - (\mathbf{s} - \mathbf{s}_0) \cdot \mathbf{r_i}$$

By inserting the new total path length into (2.15), and expressing the new relation in complex function, we get the following relation:

$$\begin{aligned} \epsilon_{P,i} &= \frac{E_0 e^2}{mc^2 R} f_\mathrm{i} e^{i\{2\pi vt - (2\pi/\lambda)[R - (\mathbf{s}-\mathbf{s}_0)\cdot \mathbf{r}_\mathrm{i}]\}} \\ &= \frac{E_0 e^2}{mc^2 R} e^{2\pi i(vt - R/\lambda)} f_\mathrm{i} e^{(2\pi i/\lambda)(\mathbf{s}-\mathbf{s}_0)\cdot \mathbf{r}_\mathrm{i}} \end{aligned} \tag{2.16}$$

To get the instantaneous electric field due to particle, summation over the instantaneous electric field of atoms in particle is performed as:

$$\epsilon_{P,\text{ particle}} = \sum_{\mathrm{i}=1}^{N} \epsilon_{P,\mathrm{i}} = \frac{E_0 e^2}{mc^2 R} e^{2\pi i(vt - R/\lambda)} \sum_{i=1}^{N} f_\mathrm{i} e^{(2\pi i/\lambda)(\mathrm{s}-\mathrm{s}_0)\cdot \mathrm{r}_\mathrm{i}} \tag{2.17}$$

Multiplying $\epsilon_{P,\text{ particle}}$ with its conjugate complex $\epsilon^*_{P,\text{ particle}}$ we get E^2:

$$\epsilon_{P,\text{ particle}}\, \epsilon^*_{P,\text{ particle}} = \frac{E_0^2 e^4}{m^2 c^4 R^2} \sum_{\mathrm{i}=1}^{N} \sum_{\mathrm{j}=1}^{N} f_\mathrm{i} f_\mathrm{j}^* e^{(2\pi i/\lambda)(\mathbf{s}-\mathbf{s}_0)\cdot\left(\mathbf{r}_\mathrm{i} - \mathbf{r}_\mathrm{j}\right)} \tag{2.18}$$

Then, the scattered intensity from particle, $I_{particle}$, is obtained by multiplying both sides of the above relation with $c/8\pi$. If we recognize I_e in (2.3) (intensity scattered by a single free electron) without polarization factor, the final relation for $I_{particle}$ can be expressed as:

$$I_{\text{particle}} = I_e \sum_{\text{i}=1}^{N} \sum_{\text{j}=1}^{N} f_{\text{i}} f_{\text{j}}^{*} e^{(2\pi i/\lambda)(\mathbf{s}-\mathbf{s}_0)\cdot\left(\mathbf{r}_{\text{i}}-\mathbf{r}_{\text{j}}\right)} \tag{2.19}$$

where N, $(\mathbf{s}-\mathbf{s}_0)$, $(\mathbf{r}_{\text{i}}-\mathbf{r}_{\text{j}})$, f_{i}, and f_{j}^{*} are the number of atoms in particle, momentum transfer vector direction, interatomic distance vector connecting i^{th} and j^{th} atoms, atomic scattering factor for i^{th} atom, atomic scattering factor for j^{th} atom, respectively.

2.4.2 Unit Cell Summation

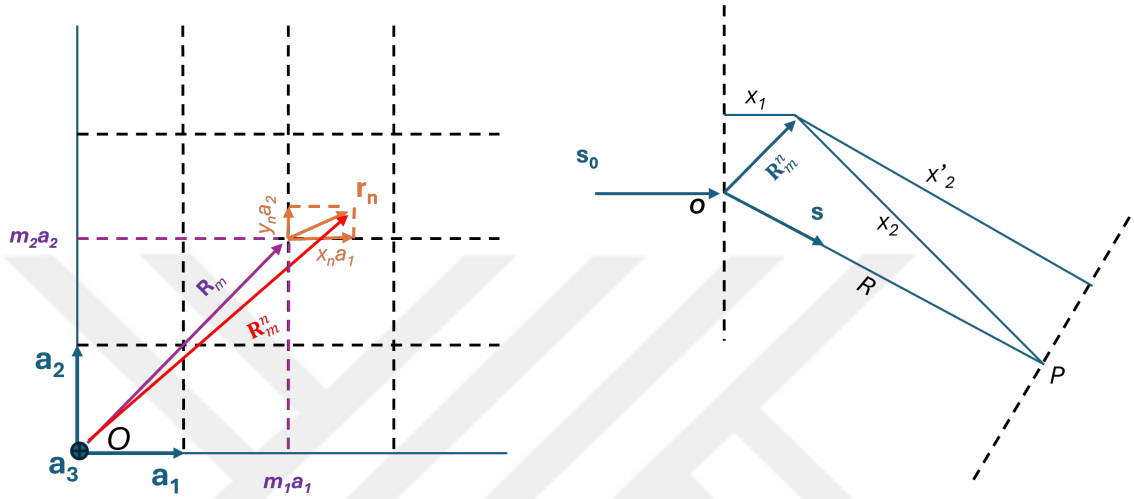
When an atomic environment is the same everywhere within a crystal, we can define the crystal in terms of a single unit cell to represent the whole crystal. In this case, the position of an n^{th} atom in unit cell $m_1m_2m_3$ can be given by $\mathbf{R}_m^n = m_1\mathbf{a_1} + m_2\mathbf{a_2} + m_3\mathbf{a_3} + \mathbf{r}_n$ relative to a crystal origin at *O*. We consider scattered intensity at point *P* along s direction with *R* distance away from origin at *O* as illustrated in 2.4

The instantaneous value of the electric field at observation point *P* due to the unmodified scattering from the atom (m,n) can be expressed by changing $\mathbf{r}_n$ coordinate vector in (2.16) with new coordinate vector $\mathbf{R}_m^n$ as:

$$\epsilon_p = \frac{E_0 e^2}{mc^2 R} f_n e^{i\{2\pi vt-(2\pi/\lambda)[R-(\mathbf{s}-\mathbf{s}_0)\cdot(m_1\mathbf{a}_1+m_2\mathbf{a}_2+m_3\mathbf{a}_3+\mathbf{r}_n)]\}} \tag{2.20}$$

The resultant field at *P* due to all the atoms in the crystal can be obtained by summing fields over atoms in unit cell, then over unit cells in the crystal. We assume that our small crystal has the shape of a parallelopipedon with lengths N_1a_1, N_2a_2, and N_3a_3 parallel to the crystal axes $\mathbf{a_1}\mathbf{a_2}\mathbf{a_3}$. Here, N_1, N_2, and N_3 are the number of unit cells in $\mathbf{a_1}$, $\mathbf{a_2}$, and

Figure 2.4: *Left) A small crystal is illustrated with cubic unit cells shown as dashed lines on* $\mathbf{a}_1\mathbf{a}_2$ *face. The fractional atomic coordinate for the* n^{th} *atom in the unit cell is shown with* $\mathbf{r}_n$ *vector. Unit cell vector for* m^{th} *unit cell is shown with* $\mathbf{R}_m$ *vector, and* $\mathbf{R}_m^n$ *vector is atomic position for* n^{th} *atom in* m^{th} *unit cell. Right) Diffraction by small crystal shown at left.* $\mathbf{s}$ *and* $\mathbf{s}_0$ *are primary and scattered beam directions, respectively. P is the detector position that is R distance away from the crystal origin.*



$\mathbf{a_3}$ directions, respectively. Then, (2.20) can be re-written in terms of 4 summations as:

$$\epsilon_p = \frac{E_0 e^2}{mc^2 R} e^{2\pi i[vt-(R/\lambda)]} \sum_n f_n e^{(2\pi i/\lambda)(\mathbf{s}-\mathbf{s}_0)\cdot\mathbf{r}_n} \sum_{m_1=0}^{N_1-1} e^{(2\pi i/\lambda)(\mathbf{s}-\mathbf{s}_0)\cdot m_1\mathbf{a}_1} \times \sum_{m_2=0}^{N_2-1} e^{(2\pi i/\lambda)(\mathbf{s}-\mathbf{s}_0)\cdot m_2\mathbf{a}_2} \sum_{m_3=0}^{N_3-1} e^{(2\pi i/\lambda)(\mathbf{s}-\mathbf{s}_0)\cdot m_3\mathbf{a}_3} \tag{2.21}$$

The last 3 summations involve sum over unit cells in directions, and the first summation involves atoms with position $\mathbf{r}_n$ in unit cell, and it is called the structure factor since $\mathbf{r}_n$ is structure-dependent. The structure factor is designated by *F*, and expressed as:

$$F = \sum_n f_n e^{(2\pi i/\lambda)(\mathbf{s}-\mathbf{s}_0)\cdot\mathbf{r}_n} \tag{2.22}$$

Note that atomic positions in (2.21) appear only in the structure factor. Hence, *F* plays an important role in crystal structure determination in X-ray diffraction experiments. Multiplying ϵ_p with its conjugate complex ϵ_p^*, and applying some geometric progress for 3

summations over unit cells $m_1 m_2 m_3$ result in:

$$\epsilon_p \epsilon_p^* = \frac{E_0^2 e^4}{m^2 c^4 R^2} F F^* \frac{\sin^2(\pi/\lambda)\,(\mathbf{s}-\mathbf{s}_0)\cdot N_1\mathbf{a}_1}{\sin^2(\pi/\lambda)\,(\mathbf{s}-\mathbf{s}_0)\cdot \mathbf{a}_1} \frac{\sin^2(\pi/\lambda)\,(\mathbf{s}-\mathbf{s}_0)\cdot N_2\mathbf{a}_2}{\sin^2(\pi/\lambda)\,(\mathbf{s}-\mathbf{s}_0)\cdot \mathbf{a}_2} \times \frac{\sin^2(\pi/\lambda)\,(\mathbf{s}-\mathbf{s}_0)\cdot N_3\mathbf{a}_3}{\sin^2(\pi/\lambda)\,(\mathbf{s}-\mathbf{s}_0)\cdot \mathbf{a}_3}. \tag{2.23}$$

Note that the right-hand side of the above equation is equal to E^2 [6], and multiplying both sides of the equation by $c/8\pi$, we obtain the intensity at the point of observation, $I_p = E^2 c/8\pi$. If the primary beam is polarized with an electric field in the plane of the paper, (2.23) is multiplied with $cos^2 2\theta$. If it is unpolarized, then (2.23) is multiplied with polarization factor derived before as $(1+\cos^2 2\theta)/2$. If FF^* is abbreviated as F^2, and $I_e = I_0 \frac{e^4}{m^2 c^4 R^2}\left(\frac{1+\cos^2 2\theta}{2}\right)$ relation is used, we can express the intensity I_p from a small parallelopipedon crystal at distance *R* away from the detector for an unpolarized primary beam of intensity I_0 as:

$$I_p = I_e F^2 \frac{\sin^2(\pi/\lambda)\,(\mathbf{s}-\mathbf{s}_0)\cdot N_1\mathbf{a}_1}{\sin^2(\pi/\lambda)\,(\mathbf{s}-\mathbf{s}_0)\cdot \mathbf{a}_1} \frac{\sin^2(\pi/\lambda)\,(\mathbf{s}-\mathbf{s}_0)\cdot N_2\mathbf{a}_2}{\sin^2(\pi/\lambda)\,(\mathbf{s}-\mathbf{s}_0)\cdot \mathbf{a}_2} \times \frac{\sin^2(\pi/\lambda)\,(\mathbf{s}-\mathbf{s}_0)\cdot N_3\mathbf{a}_3}{\sin^2(\pi/\lambda)\,(\mathbf{s}-\mathbf{s}_0)\cdot \mathbf{a}_3} \tag{2.24}$$

Three quotients in the above equation affect the value of intensity at the point of observation. These quotients are in the following form:

$$y = \frac{\sin^2 Nx}{\sin^2 x}$$

where $x_i = (\pi/\lambda)\,(\mathbf{s}-\mathbf{s}_0)\cdot \mathbf{a}_i$. Whenever *x* is an integer multiple of π, as $x = n\pi$, we observe sharp peaks in *y*. Intensity maxima scales with N^2, and it is centered at $x = n\pi$. As the number of unit cells increases in crystal, peaks get narrower and have zero intensity everywhere else outside $x = n\pi$. Similarly, for the intensity I_p to be maximum, the following three conditions must be satisfied simultaneously:

$$(\pi/\lambda)\,(\mathbf{s}-\mathbf{s}_0)\cdot \mathbf{a}_1 = h'\pi$$

$$(\pi/\lambda)\,(\mathbf{s}-\mathbf{s}_0)\cdot \mathbf{a}_2 = k'\pi$$

$$(\pi/\lambda)\,(\mathbf{s}-\mathbf{s}_0)\cdot \mathbf{a}_3 = l'\pi$$

where h', k', and l' are integers. Rearranging above relation in the following form gives rise to the 3 Laue equations:

$$\begin{aligned}(\mathbf{s}-\mathbf{s}_0)\cdot\mathbf{a}_1 &= h'\lambda \\ (\mathbf{s}-\mathbf{s}_0)\cdot\mathbf{a}_2 &= k'\lambda \\ (\mathbf{s}-\mathbf{s}_0)\cdot\mathbf{a}_3 &= l'\lambda\end{aligned} \tag{2.25}$$

These three equations together are equivalent to the Bragg law [6].

Structure function, *F*, depends on atomic positions in a unit cell. If we represent atomic positions as a fractional coordinate x_n, y_n, z_n that are between 0 and 1, then the basis vector $\mathbf{r}_n$ for an atom in unit cell can be written in terms of direct space lattice vectors $\mathbf{a}_1$, $\mathbf{a}_2$, $\mathbf{a}_3$ and fractional coordinates as:

$$\mathbf{r}_n = x_n\mathbf{a}_1 + y_n\mathbf{a}_2 + z_n\mathbf{a}_3$$

When Bragg's law is satisfied for an hkl-reflection, structure factor in (2.22) can be given by using reciprocal lattice vectors $\mathbf{b}_1$, $\mathbf{b}_2$, $\mathbf{b}_3$ as $\mathbf{s}-\mathbf{s}_0 = \lambda\mathbf{H}_{hkl} = \lambda\left(h\mathbf{b}_1 + k\mathbf{b}_2 + l\mathbf{b}_3\right)$ and expressing the cell vectors in terms of fractional coordinates as:

$$F_{hkl} = \sum_n f_n e^{2\pi i(h\mathbf{b}_1+k\mathbf{b}_2+l\mathbf{b}_3)\cdot(x_n\mathbf{a}_1+y_n\mathbf{a}_2+z_n\mathbf{a}_3)} = \sum_n f_n e^{2\pi i(hx_n+ly_n+lz_n)} \tag{2.26}$$

In the Face-Centered Cubic (FCC) unit cell of monatomic crystal structure, there are 4 atoms which have fractional coordinates as 0,0,0; 1/2,1/2,0; 1/2,0,1/2; 0,1/2,1/2. Summing over all 4 atoms in (2.26) results in following expression [7]:

$$F_{hkl} = f\left[1 + e^{\pi i(h+k)} + e^{\pi i(h+l)} + e^{\pi i(k+l)}\right] \tag{2.27}$$

Using the relation $e^{\pi im} = (-1)^m$, where *m* is an integer, we can simplify the structure factor as:

hkl unmixed (all odd or even): $F_{hkl} = 4f$

hkl mixed: $F_{hkl} = 0$

Based on the above rule, we can observe reflections from planes such as (111), (200), and (220) but not for the planes (100), (210), (112), etc.

To include the effect of atomic vibrations on intensity, (2.26) is multiplied by e^{-M} as

$$F_T = \sum_n f_n e^{-M_n} e^{2\pi i(hx_n+ky_n+lz_n)} \tag{2.28}$$

where $M = B\sin^2\theta/\lambda^2$ with $B = 8\pi^2\langle u_s^2\rangle$. Here, $\langle u_s^2\rangle$ is the mean square of the component of displacement normal to the diffracting plane (or along $\mathbf{s}-\mathbf{s}_0$). In case of only one kind of atom in a unit cell, e^{-M} goes outside of the sum in (2.28), and necessary quantity F_T^2 can be written as:

$$F_T^2 = e^{-M} F_{hkl}^2 \tag{2.29}$$

where the first factor is often called the Debye temperature factor. Thus, the final equation for intensity from a small crystal can be written as:

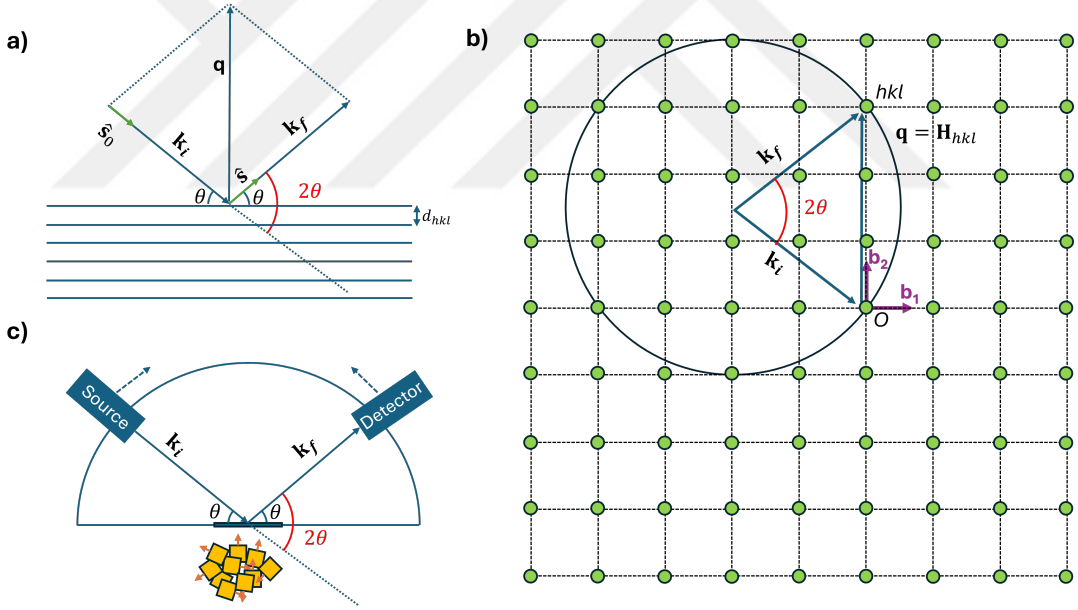
$$\begin{aligned} I_{particle,ucell} = I_e F_T^2 &\frac{\sin^2(\pi/\lambda)\,(\mathbf{s}-\mathbf{s}_0)\cdot N_1\mathbf{a}_1}{\sin^2(\pi/\lambda)\,(\mathbf{s}-\mathbf{s}_0)\cdot \mathbf{a}_1} \frac{\sin^2(\pi/\lambda)\,(\mathbf{s}-\mathbf{s}_0)\cdot N_2\mathbf{a}_2}{\sin^2(\pi/\lambda)\,(\mathbf{s}-\mathbf{s}_0)\cdot \mathbf{a}_2} \\ &\times \frac{\sin^2(\pi/\lambda)\,(\mathbf{s}-\mathbf{s}_0)\cdot N_3\mathbf{a}_3}{\sin^2(\pi/\lambda)\,(\mathbf{s}-\mathbf{s}_0)\cdot \mathbf{a}_3} \end{aligned} \tag{2.30}$$

2.5 Reciprocal Lattice and Bragg Law

A brief introduction about the reciprocal lattice and Bragg's law for diffraction is given in this section. This will help a better understanding of the Rietveld analysis in reciprocal space as we will use it in Chapter 4. Atomic planes are shown as a set of horizontal lines in Figure 2.5(a). These sets of atomic planes are parallel to each other, and the distance between the two closest planes is d_{hkl} (hkl in the subscript is the Miller indices). The primary beam, $\mathbf{k}_i$, is incident on the plane with angle θ. The primary beam has direction along unit vector $\mathbf{s}_0$, and it has a magnitude equal to the reciprocal of wavelength, $1/\lambda$. Similarly, we define the scattered beam with $\mathbf{k}_f$ that makes an angle θ with the irradiated atomic plane, hkl. The scattered beam has direction along unit vector $\mathbf{s}$, and it has a magnitude equal to the reciprocal of wavelength, $1/\lambda$. Thus, both the primary

and scattered beams have the same magnitude, $1/\lambda$, and they make the same angle, θ, with atomic plane, hkl. The angle between the $\mathbf{k}_i$ and $\mathbf{k}_f$ is 2θ. The difference between these vectors, $\mathbf{k}_f - \mathbf{k}_i$, is called the momentum transfer vector, $\mathbf{q}$, and its direction is always normal to the atomic plane at all scattering angles, θ. When θ is equal to the Bragg angle, θ_B, we observe diffraction from a set of atomic planes according to Bragg's law, $2d_{hkl}sin\,(\theta_B) = \lambda$. Diffraction is a constructive interference of scattered waves from all atoms, that give rise to strong intensity on detector. At angles other than the Bragg angle, negligiblie intensity is created due to destructive interference. A better interpretation of Bragg's law is represented in a reciprocal lattice.

Figure 2.5: *a) Diffraction from an atomic plane in real space. b) Ewald construction in reciprocal lattice. c) Powder X-ray diffraction measurement in reflection geometry.*



Reciprocal lattice shown in Figure 2.5(b) is another representation of crystal structure. Each point in the reciprocal lattice is an atomic plane, with Miller indices hkl. Reciprocal lattice is built by 1) finding reciprocal vectors $\mathbf{b}_1$, $\mathbf{b}_2$, $\mathbf{b}_3$ from crystal axes $\mathbf{a}_1$, $\mathbf{a}_2$, $\mathbf{a}_3$ [7], and, 2) creating points with vector $\mathbf{H}_{hkl} = h\mathbf{b}_1 + k\mathbf{b}_2 + l\mathbf{b}_3$ for all Miller

indices, hkl. Bragg's law in reciprocal lattice states that whenever momentum transfer vector $\mathbf{q}$ equals to $\mathbf{H}_{hkl}$, diffraction is observed. This is best illustrated by the Ewald construction. In the Ewald construction, the primary beam terminates at the origin of the reciprocal lattice O, and it originates from the center of the sphere that has a radius equal to the length of $\mathbf{q}$ as $|\mathbf{q}| = 1/\lambda$ such that the sphere's surface touches the origin, O. All reciprocal points that touch the surface of the sphere satisfy Bragg's law, that is $\mathbf{q} = \mathbf{H}_{hkl}$. The magnitude of $\mathbf{H}_{hkl}$ is equal to inverse of interplanar distance $|\mathbf{H}_{hkl}| = 1/d_{hkl}$. The Magnitude of $\mathbf{q}$ is found as $|\mathbf{q}| = 2\pi sin\,(\theta)\,/\lambda$ from the geometric relation shown in Figure 2.5(b). Then, we can show that $|\mathbf{q}| = |\mathbf{H}_{hkl}|$ is equivalent to usual form of Bragg's law $2dsin\,(\theta) = \lambda$ as:

$$\begin{aligned} |\mathbf{q}| &= |\mathbf{H_{hkl}}| \\ \frac{2\sin(\theta_B)}{\lambda} &= \frac{1}{d_{hkl}} \end{aligned} \tag{2.31}$$

The powder X-ray diffraction technique can measure the diffraction pattern, called Powder X-ray Diffraction (PXRD) pattern, from a powder sample in two different geometries: reflection or transmission geometry. In this study, we used the X-ray diffractometer that allowed reflection geometry (also known as Bragg-Brentano geometry) as illustrated in Figure 2.5(c). In reflection geometry, both the X-ray source and detector move simultaneously at the same angle. At each angle, the diffracted intensity is measured for a certain amount of time. Ideally, the powder sample contains an ensemble of crystallite particles with random orientations. Thus, all reciprocal lattice points that fall on the Ewald sphere can be measured when angular space is scanned. This is because a certain portion of particles will have the proper orientation to diffract at a given diffraction angle.

3. MOLECULAR DYNAMICS SIMULATIONS AND CALCULATION OF POWDER X-RAY DIFFRACTION DATA OF THE REALISTIC NANOCRYSTALS

3.1 Introduction

MD simulation is a computer simulation algorithm that can be used to study the physical interactions of atoms and molecules as a function of time under different conditions, such as temperature and pressure. The MD algorithm provides the trajectory of a simulated system by numerically solving Newton's equations of motion. Forces and potential energies between particles are calculated with interatomic potential or force field (FF). In this study, we used the MD simulation to obtain realistic nanocrystals at different temperatures.

One of the most used interatomic potentials for metals is the Embedded Atom Method (EAM) which was proposed by Daw and Baskes [8, 9]. The total energy of a system consisting of n atoms can be expressed as a sum of individual atomic energies [10]:

$$E_{tot} = \sum_{i}^{n} E_i \tag{3.1}$$

In the EAM, E_i is calculated as:

$$E_i = \frac{1}{2} \sum_{j} \phi(r_{ij}\,) + F(\bar{\rho}_i) \quad and \quad \bar{\rho}_i = \sum_{j} \rho(r_{ij}). \tag{3.2}$$

where $\phi\,(r_{ij})$, $\rho(r_{ij})$, and $F(\bar{\rho}_i)$ are the pair, density, and embedded functions and r_{ij} is the distance between atom pairs *i* and *j*.

In this chapter, first, we will explain our developed MD methodology, then, calculate the structural parameters of realistic nanocrystals obtained from the MD simulation. Finally, the derivation of the DSE and its optimized version to calculate PXRD data will

be given.

3.2 Creating Ideal Nanocrystals

First, a large cubic box of atoms was created by replicating the FCC unit cell with a lattice parameter of 4.0626 Å corresponding to that of bulk gold at 0 K. The edge length of the box was larger than the maximum nanocrystal diameter desired (30 nm). Then, five spherical nanocrystals with nominal diameters of 5, 10, 15, 20, and 30 nm were carved out from the created cubic box. These nanocrystals are called ideal nanocrystals and have the same interatomic distances both at the core and the surface layers. The total number of atoms for 5, 10, 15, 20, and 30 nm nanocrystals is 3589, 28897, 106114, 231477, and 781145, respectively.

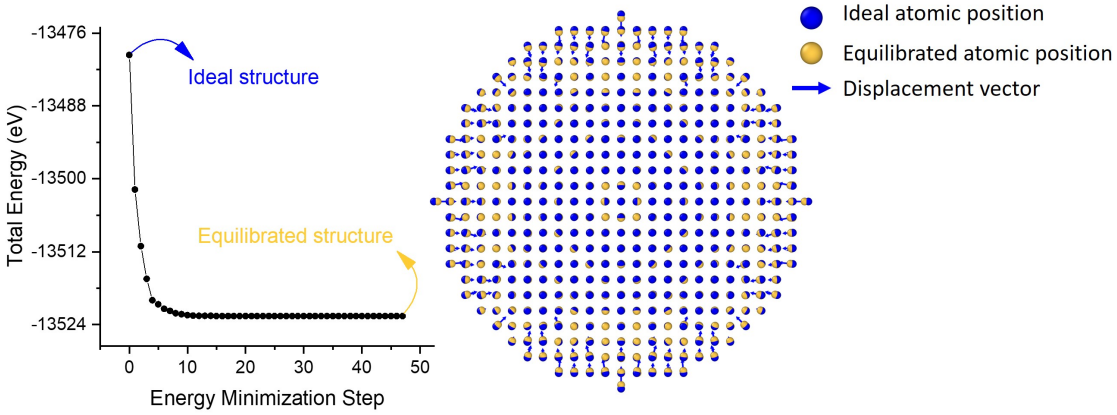
3.3 Simulation Methodology

In MD simulations, first, the force field governing the behavior of the system at various ambient conditions was selected [11]. We used the modified EAM interatomic potential developed by Sheng et al. [12] since its validity for gold nanocrystals was previously tested and confirmed against ab initio Density Functional Theory (DFT) calculations [3]. This potential was also shown to reliably generate the elastic stiffness constants of gold nanocrystals from 100 to 1000 K [13]. Then, each nanocrystal was placed inside a non-periodic simulation box with dimensions that were 2 nm longer than the nominal diameter of the nanocrystal to allow for the expansion of particle dimensions with increasing temperature.

Afterward, energy minimization was performed at 0 K with a conjugate gradient algorithm as implemented in Large-scale Atomic/Molecular Massively Parallel Simulator (LAMMPS) [14]. During this process, the potential energy of nanocrystals was iteratively minimized by changing atomic positions until the relative energy difference

between two subsequent configurations was stabilized within 10^{-12} or interatomic forces converged to 10^{-12} eV/Å within a maximum of 8×10^4 steps as shown in Figure 3.1 (left). The final configuration obtained from the energy minimization corresponded to the minimum energy configurations and was saved as the 0 K static coordinates. The resulting realistic nanocrystal configuration has large atomic displacements on the surface, as shown in Figure 3.1 (right).

Figure 3.1: *Left) Change in the total energy of the spherical gold nanocrystal during MD simulations performed on ideal nanocrystalline atomic configuration. The resulting energy-minimized atomic configuration has less total energy and is thermodynamically stable. Right) The atomic configurations of ideal (blue markers) and energy-minimized versions (yellow markers) of the gold nanocrystal with 5 nm nominal diameter. The blue arrows show the displacement vector.*

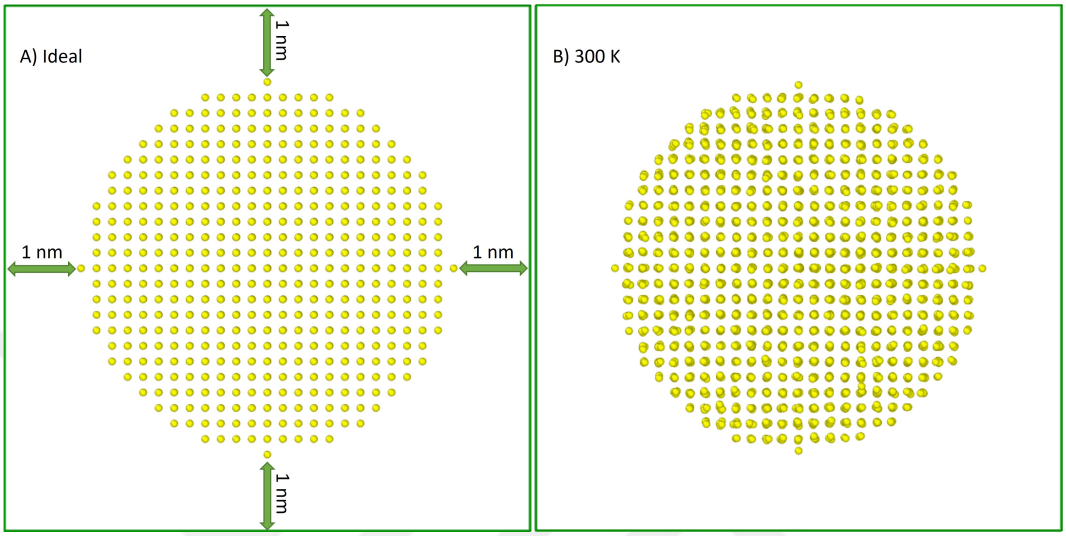


Following energy minimization, atomic velocities with Gaussian distribution were assigned to 0 K static coordinates to initialize their kinetic energy at 2 K and nanocrystals were equilibrated again at the desired finite temperatures with the following steps: 1) heat from 2 K to 600 K for 50 ps, equilibrate at 600 K for 50 ps to allow the system to evolve, 2) cool back to 300 K during 100 ps, 3) equilibrate at 300 K for 1000 ps. From 300 K and on, a production run was performed for 1 ns, during which 5000 snapshots of atomic coordinates with a time interval of 0.2 ps were saved. Similarly, configurations

were cooled continuously from high to targeted low temperatures during 100 ps and then equilibrated at 200 K, 100 K, and 10 K for 1000 ps. Snapshots were saved during the 1 ns production run. At the selected temperatures, two versions of atomic configurations were created for each nanocrystal model: 1) instantaneous atomic coordinates of nanocrystals called snapshot coordinates, and 2) static atomic coordinates, which were computed from the average of 5000 snapshot coordinates. Snapshot coordinates included dynamic atom displacements from static coordinates resulting from thermal vibrations. In contrast, static coordinates included only static atom displacements from ideal lattice positions at a particular temperature which resulted from surface reconstruction and/or relaxation. In all MD simulations, 1 fs timestep was used, and the temperature was controlled with Nose–Hoover thermostat [15] in NVT (N: constant number of atoms, V: constant volume, T: constant temperature) ensemble with a damping parameter of 0.1 ps. These 5000 final snapshot coordinates were saved, as well as their average configuration, i.e., finite-temperature static coordinates. The method we used to create our nanocrystal models here is consistent with previous studies in the literature [16, 17]. Validation of the atomic configurations thus obtained has been reported [18] using the melting point, where we confirmed the agreement between experimental measurements and the calculated melting points of 5 and 10 nm gold nanocrystals, which were 1140 and 1220 K, respectively.

Gold nanocrystal in the simulation box can be seen in Figure 3.2. The ideal configuration illustrated in Figure 3.2(a) was converted to the one in Figure 3.2(b) with some atomic displacement after equilibration at 300 K.

Figure 3.2: *Atomic coordinates of a 5 nm diameter gold nanocrystal with a) ideal and b) equilibrated structure at 300 K temperature (surface view of the nanoparticles). Simulation box is shown as green lines around the particle. Inner arrows show the extra side lengths equivalent to 2 nm in each direction.*

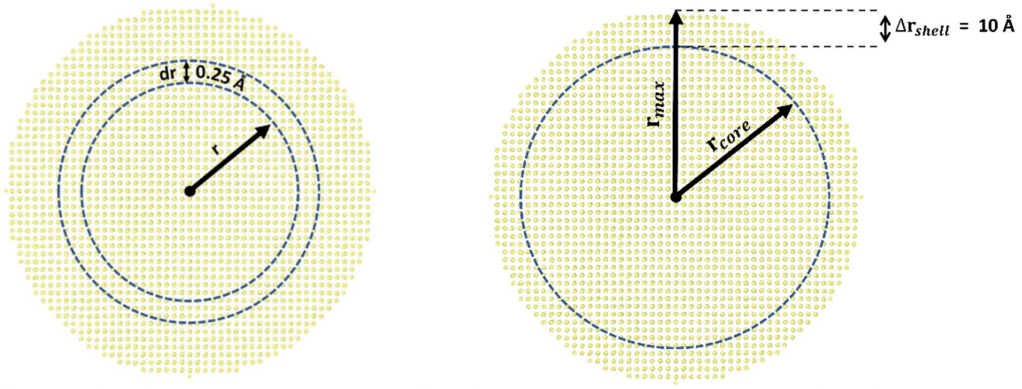


3.4 Structural Parameters in Real Space

3.4.1 Calculation of Local and Average Structural Parameters

Structural properties of nanocrystals can be represented in two different ways: local and particle-wide average. While the particle-wide average property includes all atoms in the particle, the local property can be obtained as a function of radial distance or volume region. To calculate the radial change of any property, averaging is performed over atoms inside the atomic layer at a given radial distance as illustrated in Figure 3.3 (left). To calculate the property in the volume region, averaging is performed over atoms inside the volume region. The volume region can be surface or core as illustrated in Figure 3.3 (right). The surface region is a shell with a thickness of approximately 10 Å. This thickness was selected based on the fluctuation of radial change of the lattice parameter, as will be shown later.

Figure 3.3: *Left) Illustration of an atomic layer at a radial distance, r, on the nanoparticle. Layer thickness, dr is 0.25 Å. Right) Illustration of surface and core region.*



3.4.2 Mean Square Displacement

Atoms in materials are subject to thermal displacements from their equilibrium positions at finite temperatures. In the case of solids, they oscillate around equilibrium positions, meaning they are confined to certain positions [19]. The ensemble average of the square of displacements of atoms from their equilibrium position is called MSD [20]. This average is taken over both the time and number of atoms in MD. There are two kinds of MSD, static and dynamic MSDs. In addition, a sum of them can be considered as total MSD. The static MSD is given as:

$$\left\langle \vec{u}^2 \right\rangle_{\text{static}} = \frac{1}{N} \sum_{i=1}^{N} \left[\langle \vec{r}_i \rangle_t - \vec{r}_i^{\,\text{ideal}} \right]^2 \tag{3.3}$$

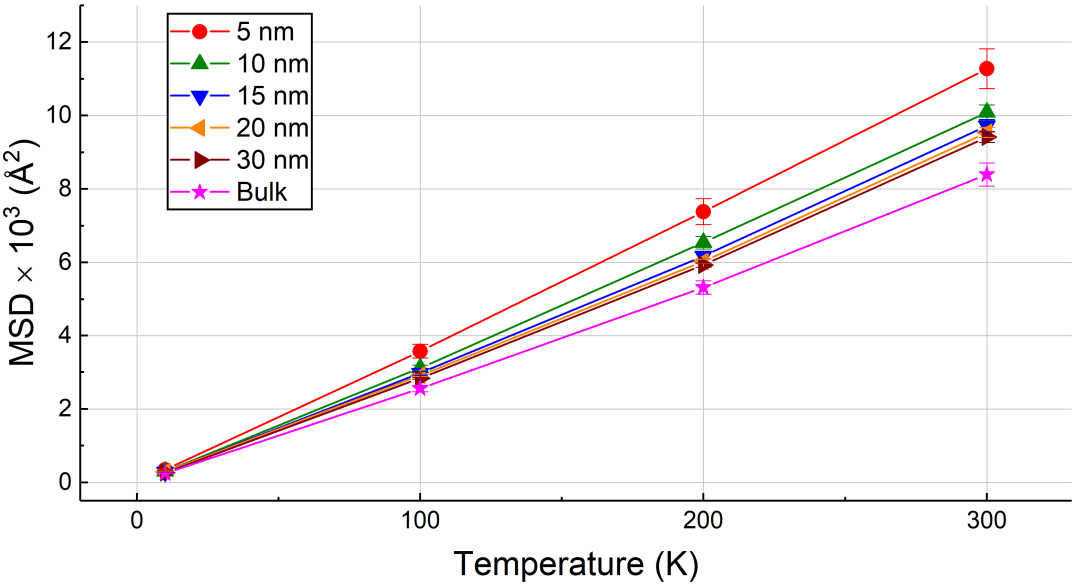
where $\vec{u}$ is the displacement vector, $\langle \vec{r}_i \rangle_t$ is the time-averaged coordinate vector of *i*'th atom, $\vec{r}_i^{\,\text{ideal}}$ is the coordinate of its ideal lattice point (at a particular temperature) and *N* is the total number of atoms in the nanocrystal. The dynamic MSD is based on the following expression:

$$\left\langle \vec{u}^2 \right\rangle_{\text{dynamic}} = \left\langle \vec{u}^2 \right\rangle = \frac{1}{t_0} \int_0^{t_0} \frac{1}{N} \sum_{i=1}^{N} \left[\vec{r}_i(t) - \langle \vec{r}_i \rangle_t \right]^2 dt \tag{3.4}$$

where $\vec{r}_i(t)$ and $\langle \vec{r}_i \rangle_t$ are the snapshot and static lattice coordinate of atom *i*; *dt* and t_0 are the timestep and simulation time, respectively.

In this study, the dynamic MSD was calculated with 5000 snapshots using (3.4) at 10 K, 100 K, 200 K and 300 K temperatures. The particle-wide average dynamic MSD is shown in Figure 3.4. The MSDs corresponding to bulk nanocrystal were also calculated with an NPT ensemble (N: constant number of atoms, P: constant pressure, T: constant temperature) where temperature settings were the same as those of our nanoparticle simulations. Calculated MSD values from our bulk system agreed well with measurements in the literature [21] and showed a linear dependence on the temperature [6]. Similar relationships can be observed for all nanocrystals, and an inverse relationship between particle size and MSD is clearly visible at all temperatures. These can be attributed to the increasing proportion of surface atoms in smaller nanocrystals.

Figure 3.4: *Particle-wide average dynamic MSD vs. temperature for different sizes of gold nanoparticles from real-space calculations (Error bars are standard deviations from the mean).*



3.4.3 Lattice Parameter and Lattice Strain

Calculation of root-mean-square (rms) lattice strains was performed on static atom coordinates in three steps. First, each ideal nanocrystal model was decomposed into repeating unit cells. These nanocrystal models did not contain any atomic displacements and were used as reference; hence it was trivial to identify the relative positions of atoms in the corresponding equilibrated nanocrystals. For each atom in the nanocrystal, one unit cell was created by considering three second nearest neighbours located along [011], [101], and [110] directions. Equivalent positions of edge atoms along [100], [010], and [001] directions were calculated by combinations of these atoms as:

$$\vec{r}_{100} = \frac{\vec{r}_{000} - \vec{r}_{011} + \vec{r}_{101} + \vec{r}_{110}}{2}$$
$$\vec{r}_{010} = \frac{\vec{r}_{000} + \vec{r}_{011} - \vec{r}_{101} + \vec{r}_{110}}{2}$$
$$\vec{r}_{001} = \frac{\vec{r}_{000} + \vec{r}_{011} + \vec{r}_{101} - \vec{r}_{110}}{2}$$

Similarly, other nearest neighbours in opposite directions were searched. If any of the three neighbours of the origin atom were missing, which was the case for the outermost surface layer of the particle, this atom did not form a unit cell. Once all unit cells were obtained, their center positions were calculated, and overlapping unit cells were excluded from the calculation. This process was repeated on all energy-minimized and finite-temperature atomistic models of our gold nanocrystals by mapping the same atomic indices of each unit cell found in ideal crystalline configurations, ($\vec{r}_{000}$, $\vec{r}_{100}$, $\vec{r}_{010}$, and $\vec{r}_{001}$) to their equilibrated or finite-temperature counterparts ($\vec{r}'_{000}$, $\vec{r}'_{100}$, $\vec{r}'_{010}$, and $\vec{r}'_{001}$,). Unlike ideal nanocrystal models, atoms that were displaced from their ideal positions in excess of 2 Å (around 5-10 atoms) were excluded from the unit cells of these equilibrated or finite-temperature nanocrystals, since such displacements were much larger than typical values of gold at room temperature. This is consistent with past literature reporting average rms displacements of simple structures at room temperature to be around 5% of first nearest

neighbour distance, approximately 0.14 Å in gold [6].

In the second step, we calculated the displacement gradient tensor for each unit cell using the infinitesimal strain theory [3]. The diagonal of these tensors yielded lattice strain in normal directions as follows:

$$\varepsilon_{xx} = \frac{\partial u}{\partial x} \approx \frac{\left(r'_{100,x} - r'_{000,x}\right) - \left(r_{100,x} - r_{000,x}\right)}{r_{100,x} - r_{000,x}}$$
$$\varepsilon_{yy} = \frac{\partial v}{\partial y} \approx \frac{\left(r'_{010,y} - r'_{000,y}\right) - \left(r_{010,y} - r_{000,y}\right)}{r_{010,y} - r_{000,y}}$$
$$\varepsilon_{zz} = \frac{\partial w}{\partial z} \approx \frac{\left(r'_{001,z} - r'_{000,z}\right) - \left(r_{001,z} - r_{000,z}\right)}{r_{001,z} - r_{000,z}}$$

where *u*, *v*, and *w* were displacement vectors along [100], [010], and [001], respectively, and the subscript of vectors (e.g., "100,x" in $r'_{100,x}$) indicated their component along normal directions. Once normal strains were evaluated, we obtained local and mean lattice parameters using

$$\begin{aligned} a_i &= \varepsilon_i \cdot a_0 + a_0 \\ \bar{a} &= \bar{\varepsilon} \cdot a_0 + a_0 \end{aligned} \tag{3.5}$$

where ε_i and a_i are normal strain and lattice parameters of any given unit cell *i* of equilibrated particle with i $\in (1,\ 3N_c)$ and *Nc* the number of unit cells created from each nanocrystal, $\bar{\varepsilon}$ and $\bar{a}$ are average normal strain and lattice parameters of the equilibrated nanocrystal and a_0 is the lattice parameter of the reference particle (ideal crystal), which was 4.0626 Å in our study. Once local and average lattice parameters were obtained for each nanocrystal, the rms strain was calculated by

$$\varepsilon_{rms} = \left[\frac{\sum_{i=1}^{3N_c}\left(\frac{a_i - \bar{a}}{\bar{a}}\right)^2}{3N_c}\right]^{1/2} \tag{3.6}$$

where $3N_c$ stands for the three normal strains (along x, y and z directions) of N_c unit cells.

The results of these calculations are seen in Figure 3.5 along with their temperature and crystallite-size dependence. Here we also included the average lattice parameter and rms strain values from a bulk crystal model, which was obtained from MD by creating a simulation box of 30 unit cells in each lattice direction under periodic boundary

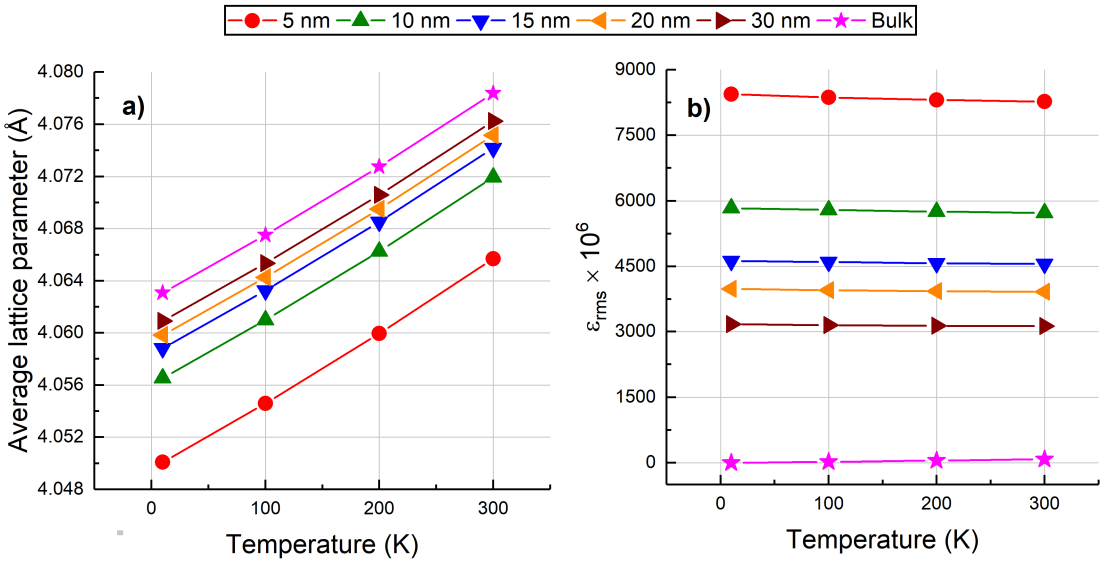
conditions and carving spherical shapes. This bulk model was used to investigate the limiting values of rms strains when crystallite size approached infinity, and no free surface was present, completely eliminating surface effects from our calculations. From Figure 3.5(a), we see that the average lattice parameters increase with increasing temperature for all nanocrystals. Average lattice parameters of larger nanocrystals (15, 20 and 30 nm) are close to each other and are larger than those of smaller particles (5 and 10 nm). This is because a larger proportion of the total atoms was contributed by surface atoms in smaller nanocrystals, which also experienced the largest radial displacements due to the energy-minimization step (inward movement) and subsequent MD simulations (outward movement), resulting in much smaller unit cells on average for the smaller nanoparticles. Looking at Figure 3.5(b), we observe that rms strains are independent of temperature for all nanocrystals. They are maximized for the smallest nanocrystal and decrease with increasing particle size. For the bulk crystal model, no rms strains are detected. This confirms that the rms strains in our nanocrystal models are not thermally induced but result solely from surface atoms and their relatively higher static displacements compared to atoms in the core regions. Therefore, as the proportion of surface atoms increases, rms strains also increase.

3.4.4 Particle Size

Due to the discrete nature of our nanocrystal models, their characteristic diameters had a distribution of lengths. Figure 3.6 demonstrates three representative nanoparticle dimensions for a 5 nm nominal diameter gold nanocrystal[1]. The distributions of diameters for our nanocrystal models at finite-temperature static atomic configurations were calculated by considering surface atoms (solid points on Figure 3.6, right side) whose

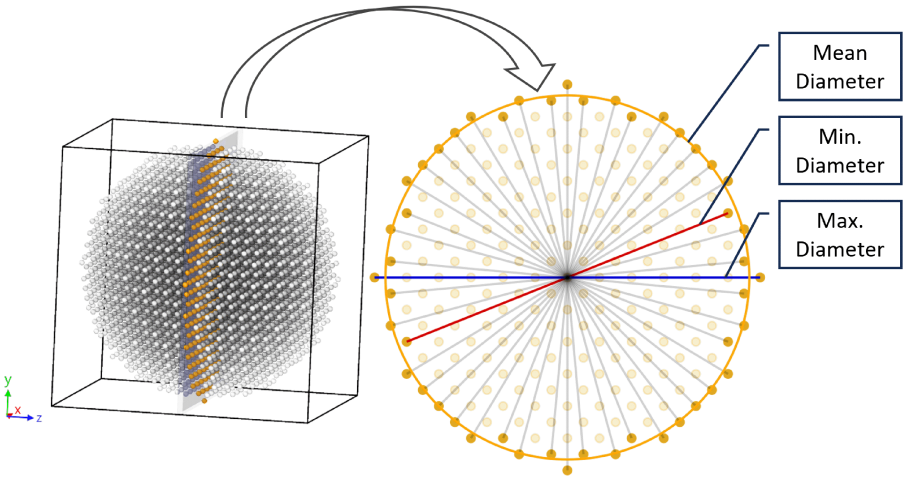
[1]Nominal size in this study refers to rounded-up Max dimensions of the ideal nanocrystal and is used in naming different sizes of gold nanoparticles.

Figure 3.5: *a) Particle-wide average lattice parameter vs. temperature, b) rms strain vs. temperature.*



Coordination Number (CN) was lower than the ideal coordination number, which was 12 for FCC lattice (These atoms were undercoordinated and formed a thin shell on the surface of the spherical nanoparticle). To do this, first, the CN of each atom was calculated by counting the number of the first-nearest-neighbour atoms inside a shell with 3.2 Å of inner radius centered on each atom. Then, core atoms with full (12) CN were eliminated so that only undercoordinated surface atoms were left. Note that only the line connecting such a pair of atoms that crossed through the center of the nanoparticle was accepted as diameter. Here, the neighbour atoms were searched within ± 0.5 Å range due to the slight shifting of atoms caused by finite temperature increases. This calculation resulted in approximately 525, 2205, 5359, 9105, and 20673 total number of diameters for 5, 10, 15, 20, and 30 nm nanoparticles, respectively. The minimum (Min), maximum (Max), mean, and standard deviation of these diameters for each nanoparticle, along with their temperature-dependent variations, are shown in Figure 3.7.

Figure 3.6: *Left) 3D illustration of a 5 nm ideal crystalline nanoparticle model. Right) The distribution of atoms on the midplane intersecting the 3D particle model. Red and blue arrows represent one of the shortest (Min) and longest (Max) diameters, respectively; while the Mean diameter indicates the average diameter.*



3.5 Effect of Force-Field Selection on the Core Lattice Parameter

The current interatomic potential (Sheng EAM) used in our MD study was compared with other commonly used interatomic potentials in the literature. We selected one different EAM potential (Foiles EAM) [9], one Modified Embedded-Atom Method (MEAM) [22], and three Machine Learning (ML) force fields. The three different ML force fields, Local-Density Approximation (LDA) ML-FF, Revised Perdew-Burke-Ernzerhof (rPBE) ML-FF, and Hybrid ML-FF, were developed by Zeni et al. [23]. The accuracy of these force fields was compared in terms of the core lattice parameter of 5 nm nanocrystal at 300 K measured experimentally [24]. The results suggest that the Sheng EAM interatomic potential is much more accurate, and it predicted the core lattice parameter (a=4.07125 Å) close to the experimental value (a=4.0729 Å) as shown in Table 3.1.

[2]The experimental values are corrected for the heating effect of the electron beam as suggested by the authors (see Fig.1 and eq.3 of the article).

Figure 3.7: *Temperature dependence of the Min, Max and Mean diameters computed from gold nanoparticles with nominal sizes of 5, 10, 15, 20 and 30 nm. Error bars of Mean diameters refer to the standard deviations.*

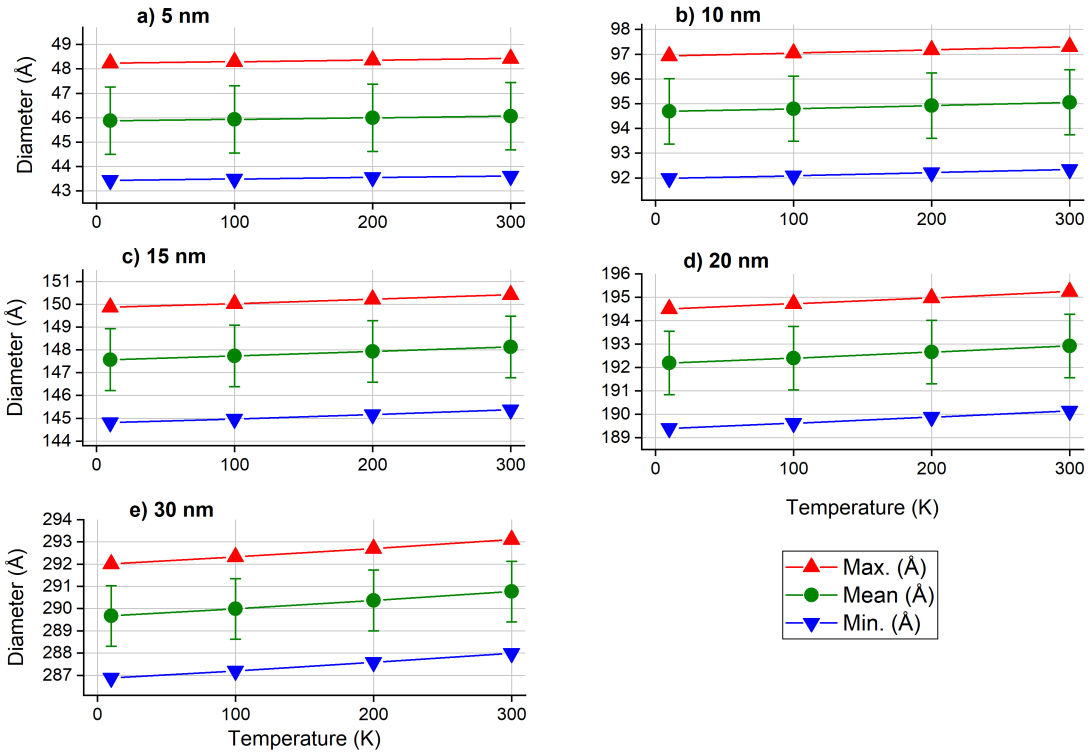


Table 3.1: *The core lattice parameter dependence of 5 nm nanocrystal (300 K) on interatomic potential.*

Force Field Type	**Core a (Å)**	**sd a (Å)**
LDA ML-FF	4.05595	0.009
rPBE ML-FF	4.24105	0.003
Hybrid ML-FF	4.12585	0.007
Sheng EAM	4.07125	0.004
Foiles EAM	4.08773	0.007
Baskes MEAM	4.08888	0.007
Experimental	4.0729[2]	-

3.6 Derivation of Debye Scattering Equation

X-ray diffraction patterns of nanopowders containing monodispersed, non-interacting, and randomly oriented ensemble of nanocrystals were simulated using the DSE. The DSE assumes no periodicity in structure, hence, can be used for both crystalline and disordered systems. Atomic coordinates obtained from the MD simulations and element type were used as an input to the DSE along with experimental settings such as wavelength and desired angular range. In Chapter 2, we derived scattered intensity from small single crystal using atomic summation method. That relation was derived for single orientation of nanocrystal. Now, we will extend it to the nanopowder system by performing orientational averaging. The detailed derivation is given below.

In the kinematical limit, scattering amplitude from a set of i atoms at $\mathbf{r}_i$ position can be expressed as:

$$\psi(\mathbf{Q}) = \sum_i \psi_i = \sum_i f_i \exp\left(i\mathbf{Q} \cdot \mathbf{r}_i\right) \tag{3.7}$$

where f and $\mathbf{Q}$ are atomic scattering factor and scattering vector, respectively. The atomic scattering factor is Q-dependent, but it is dropped for simplicity. Scattered intensity can be expressed by multiplying scattering amplitude with its conjugate as:

$$I(\mathbf{Q}) = \psi^*(\mathbf{Q})\psi(\mathbf{Q}) = \sum_i \sum_j f_j^* f_i \exp\left[i\mathbf{Q} \cdot (\mathbf{r}_i - \mathbf{r}_j)\right] = \sum_{i,j} f_j^* f_i \exp\left(i\mathbf{Q} \cdot \mathbf{r}_{ij}\right) \tag{3.8}$$

where $\mathbf{r}_{ij}$ is the interatomic vector connecting atom pairs i and j. In the case of a powder ensemble of particles, orientational averaging of $I(\mathbf{Q})$ is necessary. Assuming $\mathbf{Q}$ is fixed along z-axis and using the relation of $sinx = (e^{ix} - e^{-ix})/2i$, we can perform orientational averaging as

$$\langle I(\mathbf{Q}) \rangle = \sum_{i,j} f_j^* f_i \left\langle \exp\left(i\mathbf{Q} \cdot \mathbf{r}_{ij}\right) \right\rangle \tag{3.9}$$

where

$$\langle \exp\left(i\mathbf{Q}\cdot\mathbf{r}_{ij}\right)\rangle = \langle \exp\left(iQr_{ij}\cos\theta\right)\rangle = \frac{\int \exp\left(iQr_{ij}\cos\theta\right)\mathrm{d}A}{\int \mathrm{d}A} = \frac{\int_{\theta=0}^{\pi}\int_{\phi=0}^{2\pi}\exp\left(iQr_{ij}\cos\theta\right)r_{ij}^2\sin\theta\,\mathrm{d}\theta\,\mathrm{d}\phi}{4\pi r_{ij}^2} = \frac{2\pi r_{ij}^2\int_{\theta=0}^{\pi}\exp\left(iQr_{ij}\cos\theta\right)r_{ij}^2\sin\theta\,\mathrm{d}\theta}{4\pi r_{ij}^2} = \frac{\left[-\exp\left(iQr_{ij}\cos\theta\right)\right]_0^{\pi}}{2iQr_{ij}} = \frac{\exp\left(iQr_{ij}\right)-\exp\left(-iQr_{ij}\right)}{2iQr_{ij}} = \frac{\sin\left(Qr_{ij}\right)}{Qr_{ij}}$$

Thus (3.9) becomes (3.10) as,

$$\langle I(\mathbf{Q})\rangle = I(Q) = \sum_{i,j} f_j^* f_i \frac{\sin\left(Qr_{ij}\right)}{Qr_{ij}} \tag{3.10}$$

If atomic form factors are real ($f^*=f$) and the system is monoatomic, the DSE equation can be simplified as:

$$I(Q) = f^2 \sum_{i,j} \frac{\sin\left(Qr_{ij}\right)}{Qr_{ij}} \tag{3.11}$$

To optimize the DSE equation in terms of computation time, interatomic distances are grouped as histogram bins in the Debyer [25] software as follows:

$$I(Q) = f^2 \sum_{i,j} \frac{\sin\left(Qr_{ij}\right)}{Qr_{ij}} = f^2\left(N + 2\sum_{i,j>i}\frac{\sin\left(Qr_{ij}\right)}{Qr_{ij}}\right) \approx f^2\left(N + 2\sum_{k} n_k \frac{\sin\left(Qr_k\right)}{Qr_k}\right) \tag{3.12}$$

where n_k and r_k are the number of pairs and the distance corresponding to the k-th bin.

3.7 Summary and Conclusions

In this chapter, first, we explained the developed MD methodology to create realistic nanocrystals at different temperatures. Unlike ideal nanocrystals, where each atom is

at a lattice point, realistic nanocrystals include surface effects due to undercoordination. Therefore, the periodicity of the structure is not preserved in the realistic nanocrystals. Following the MD simulations, we derived the DSE equation used to simulate the diffraction data from the powder ensemble of particles. These diffraction data will be used in both Rietveld and PDF refinements in the following chapters. We can list the following conclusions from the chapter:

- The MD simulations provided realistic nanocrystal structures.
- In realistic nanocrystals, the surface region has a smaller lattice parameter than the core region. In other words, bonds between atoms at the surface are shorter than the core region.
- In the realistic nanocrystals, the surface region has higher MSD than the core region.
- Both MSD and lattice parameters were size-dependent since the surface-to-volume atom ratio is size-dependent.
- Selection of appropriate interatomic potential is a must to have realistic nanocrystals from the MD simulations. When compared to the experimentally measured core lattice parameter of a spherical 5 nm nanocrystal at 300 K, the Sheng EAM potential provided a better core lattice parameter than other potentials.
- The DSE equation can be optimized with a histogram approach as implemented in the Debyer software.

4. RIETVELD ANALYSIS OF REALISTIC GOLD NANOCRYSTALS

4.1 Introduction

Powder diffraction data can be analyzed with line profile analysis methods, which treat Bragg peaks separately to extract structural parameters. This method is less useful when Bragg peaks overlap with each other. However, a more powerful method to analyze the diffraction data is Rietveld refinement. Rietveld refinement is a widely used crystallographic solution algorithm, which can characterize samples containing multiple phases even when the individual phases and their proportions are largely unknown and/or significant overlap exists between different Bragg peaks. The power behind Rietveld refinement lies in treating the whole diffraction profile at once and imposing constraints and compatibility between different Bragg peaks related to the assumed crystal phases in the diffracting sample, which effectively reduces the number of fitting parameters that describe the microstructure of each phase to manageable numbers. These constraints result from the assumed unit cell parameter representing each phase present in the investigated powder, and their microstructural parameters are refined through cycles of a least square minimization scheme. This optimization algorithm aims to find a structure model whose calculated diffraction data $I_{c,\theta}$ closely matches with the observed (measured) diffraction data $I_{o,\theta}$ by a predefined tolerance, minimizing a residual of the form [26, 27] $\sum_\theta w_\theta (I_{c,\theta} - I_{o,\theta})^2$ where w_θ is the weight derived from the error propagation scheme, and the summation is over all measured angular range.

For the past few decades, diffraction data from nanocrystalline materials have been analyzed by Rietveld refinement. However, while it has been proven successful in the

diffraction analysis of powdered bulk crystalline materials, its applicability to nanocrystalline powders has been an active area of debate [2, 28]. The problem stems from the structure factor $|F_k|^2$ used to represent the scattering power of the unit cells in nanocrystals: while powdered bulk crystals can reliably be approximated by 3D periodic stacks of atoms with a single unit cell capturing the full atomic configuration information, a single, average unit cell is insufficient to model atomic stacking for the surface atoms in nanocrystals which make up a large proportion of total atoms in such particles.

In Chapter 3, we showed that the realistic nanocrystals deviated from the periodic structure as they exhibited different lattice parameters and MSD at the core and surface region. The surface effect was much more significant at smaller nanocrystals as surface to volume ratio increases with decreasing nanocrystal size. Then, we showed how to calculate orientational averaged diffraction data from the realistic nanocrystals using the optimized DSE. Therefore, these diffraction data contain the mentioned surface effects. In this chapter, we aim to evaluate the performance of the Rietveld analysis on nanocrystal diffraction data. This is achieved by performing Rietveld analysis on nanocrystal diffraction data and then comparing extracted structural parameters from the Rietveld analysis with actual values obtained from the MD simulations.

In this chapter, we will first describe the Rietveld refinement algorithm used to calculate diffraction data from a unit cell model. Second, we will derive the necessary equations for thermal diffuse scattering. Third, our Rietveld refinement methodology to extract structural parameters (lattice parameter, MSD, and lattice strain) will be explained. Finally, we will evaluate the accuracy of the extracted structural parameters with respect to the actual ones calculated from the MD simulation. The results of this chapter will help the interpretation of Rietlved refinement results from powder nanocrystals.

4.2 Rietveld Refinement Algorithm

4.2.1 Total Powder Intensity

Calculated intensity at angle θ for a given reflection *HKL* at Bragg angle θ_B from a unit cell model in Rietveld refinement can be written as:

$$I_c(\theta) = I_b(\theta) + S_h \sum_p S_{ph} Y_{ph}(\theta) \tag{4.1}$$

where $I_b(\theta)$ is a background intensity (including diffuse scattering) which can be modeled with different functions such as linear or Chebyshev functions; S_h is a scale factor; S_{ph} is a scale factor for p^{th} phase of h^{th} reflection and it is used to determine relative amount of phases in a system; $Y_{ph}(\theta)$ is a Bragg intensity from h^{th} reflection of p^{th} phase. The summation is over phases in a system. Once the intensity for each reflection is calculated for an angular range that is wide enough to include the peak fully, they can be summed to get the total intensity. The Bragg intensity in (4.1) can be written as:

$$Y_{ph}(\theta) = F_{ph}^2(\theta_B)\, H(\theta - \theta_B)\, K_{ph}(\theta_B) \tag{4.2}$$

where F_{ph}, $H(\theta - \theta_B)$, and $K_{ph}(\theta_B)$ are a structure factor, a value of profile function at θ, and a product of various correction factors, respectively.

Intensity correction factors can be expressed as:

$$K_{ph} = \frac{E_{ph} A_h O_{ph} M_p L}{V_p} \tag{4.3}$$

where E_{ph}, A_h, O_{ph}, M_p, L, and V_p are extinction correction, absorption correction, preferred orientation correction, multiplicity, Lorentz-polarization, and unit cell volume, respectively. The functional form of each of these corrections can be found in the GSAS manual [27]. In our MD simulated diffraction data, only the last three functions apply.

4.2.2 Structure Factor

Structure factor is calculated from atom coordinates in the unit cell, temperature factors, and atom form factors. It can be expressed as:

$$F_{ph} = A_{ph} + iB_{ph} \tag{4.4}$$

where A and B are real and imaginary parts of the structure factor. We need the square of this quantity since it is proportional to intensity:

$$F_{ph}^2 = A_{ph}^2 + B_{ph}^2 \tag{4.5}$$

where A_{ph} and B_{ph} are given as:

$$A_{ph} = A_0 + A' - B''$$

$$B_{ph} = B_0 + B' + A''$$

Putting above relation, into (4.5):

$$F_{ph}^2 = \left(A_0 + A'\right)^2 + B''^2 + \left(B_0 + B'\right)^2 + A''^2$$

with,

$$A_0 = \textstyle\sum_i x_i T_i f_{oi} \cos\left(2\pi \mathbf{h} \cdot \mathbf{r}_i\right) \quad B_0 = \sum_i x_i T_i f_{oi} \sin\left(2\pi \mathbf{h} \cdot \mathbf{r}_i\right)$$

$$A' = \textstyle\sum_i x_i T_i f_i' \cos\left(2\pi \mathbf{h} \cdot \mathbf{r}_i\right) \quad B' = \sum_{\mathrm{i}} x_i T_i f_i' \sin\left(2\pi \mathbf{h} \cdot \mathbf{r}_i\right)$$

$$A'' = \textstyle\sum_i x_i T_i f_i'' \cos\left(2\pi \mathbf{h} \cdot \mathbf{r}_i\right) \quad B'' = \sum_i x_i T_i f_i'' \sin\left(2\pi \mathbf{h} \cdot \mathbf{r}_i\right)$$

where, x_i, T_i, $\mathbf{h}$, and $\mathbf{r}_i$ are atomic site fraction, temperature factor, reflection vector, and fractional coordinate of i^{th} atom in the unit cell, respectively. Summation is performed over all atoms in the unit cell. f_{oi}, f_i', and f_i'' are components of atom form factor for i^{th} atom. The reason for 3 components in A_{ph} and B_{ph} is because of atomic form factor containing anomalous scattering factors, f' and f'', in addition to X-ray scattering factor

f_o as:

$$
\begin{aligned}
f &= xT\left(f_o + f' + \mathrm{i}f''\right) \\
f_o &= c + \sum_{i=1}^{4} a_i \exp\left(\frac{-b_i \sin^2(\theta)}{\lambda^2}\right) \\
f' &= -4.421, \quad f'' = 7.293 \quad (\text{at } \lambda = 1.54 \text{ Å for gold})
\end{aligned}
\tag{4.6}
$$

Values of a_i, b_i, and c were tabulated in International Tables for Crystallography C [29], and of f' and f'' can be readily calculated by module in GSAS II software at selected wavelength and element type [30].

For isotropic thermal motion, the temperature factor, *T*, can be expressed in terms of either U_{iso} (MSD) or B_{iso} as:

$$
\begin{aligned}
T = \exp\left(-\frac{8\pi^2 U_{\text{iso}} \sin^2(\theta)}{\lambda^2}\right) &= \exp\left(-\frac{B_{iso} \sin^2(\theta)}{\lambda^2}\right) \\
B_{\text{iso}} &= 8\pi^2 U_{\text{iso}}
\end{aligned}
\tag{4.7}
$$

4.2.3 Profile Function – Size and Strain Broadening

Powder peak profiles are created with pseudo-Voigt functions, $P(\Delta T)$, that are broadened due to axial divergence [27]. The pseudo-Voigt function is defined as:

$$
P(\Delta T) = \eta L(\Delta T, \Gamma) + (1 - \eta) G(\Delta T, \Gamma) \tag{4.8}
$$

where η, Γ, $L(\Delta T, \Gamma)$, and $G(\Delta T, \Gamma)$ are mixing parameter, total peak width, Lorentzian, and Gaussian functions, respectively. The mixing parameter and total peak width can be expressed as:

$$
\begin{aligned}
\eta &= 1.36603\left(\gamma/\Gamma - 0.47719(\gamma/\Gamma)^2 + 0.11116(\gamma/\Gamma)^3\right) \\
\Gamma &= \sqrt[5]{\Gamma_G^5 + 2.69269\Gamma_G^4\gamma + 2.42843\Gamma_G^3\gamma^2 + 4.47163\Gamma_G^2\gamma^3 + 0.07842\Gamma_G\gamma^4 + \gamma^5}
\end{aligned}
\tag{4.9}
$$

where Γ_G and γ are Gaussian Full Width at Half Maximum (FWHM) and Lorentzian coefficient, respectively. In case of isotropic size and strain, Gaussian FWHM is expressed

as:

$$\Gamma_G = \sqrt{(8\ln 2)\sigma^2}, \quad \sigma^2 = U\tan^2\theta + V\tan\theta + W + \frac{P}{\cos^2\theta} \tag{4.10}$$

where *U*, *V*, and *W* are Cagliotti coefficients [30]; first and last terms contain Gaussian strain and size broadening, respectively. In the case of isotropic size and strain, the Lorentzian coefficient is described as:

$$\gamma = \frac{X}{\cos\theta} + Y\tan\theta \tag{4.11}$$

where first and second terms are Lorentzian size and strain broadening, respectively. Note that any instrumental broadening component should be subtracted from the coefficients before obtaining size and strain-related broadening.

4.3 Thermal Diffuse Scattering

When atoms in the irradiated crystallites are located at their exact lattice points, the centers ($2\theta_B$) of Bragg peaks corresponding to a particular interplanar spacing of atoms d_{hkl} can be calculated from the Bragg's law, i.e. $2d_{hkl}\sin\theta_B = \lambda$. However, this scenario is realized exactly only for an ideal crystal at 0 K. (Zero point fluctuation of atoms is expected even at 0 K; however, their effect on the total atomic displacement of gold can be neglected in molecular dynamics simulations performed above 100 K [13].) At finite temperatures above 0 K, the average thermal energy of the atoms increases, leading to the stretching of interatomic bonds and enhanced vibrational amplitude around new average lattice points [31]. To correctly relate the effects of static and dynamic atom displacements on the resulting diffraction data, several formulations have been proposed in the past literature. To start with the latter, the first-order treatment of dynamic displacements of atoms on the resulting intensity profiles assumes these displacements to be entirely uncorrelated. In this case, while a diffuse background scattering appears, the probability of constructive -and destructive- interference between scattered X-rays is also reduced,

leading to a concomitant decrease in the diffracted intensity distributions. The reduction in the scattering probability is absorbed into the atomic scattering factor as [7, 32]:

$$\begin{aligned} f &= f_0 \exp(-M) \\ M &= 2\pi^2 \left(\frac{< u^2 >}{d^2} \right) = 8\pi^2 < u^2 > \left(\frac{\sin\theta}{\lambda} \right)^2 = B \left(\frac{\sin\theta}{\lambda} \right)^2 \end{aligned} \tag{4.12}$$

where f and f_0 are the thermally modified and unmodified atomic scattering factors respectively, $< u^2 >$ is the mean squared projection of the atomic vibration amplitude from the lattice position along the particular hkl reciprocal space vector and d is the interplanar spacing with $d = \frac{\lambda}{2 \sin\theta_B}$. The formulation in (4.12) assumes that the displacement of atoms due to thermal vibrations is Gaussian distributed around their average lattice positions [33]. In this case, the expected diffraction intensity corresponding to several instantaneous positions of atoms, i.e. $I_{snapshot}$, is related to the intensity from the static or stationary lattice, i.e. I_{static}, through the Debye-Waller factor as:

$$I_{\text{snapshot}} = I_{\text{static}} \exp(-2M) + N f_0^2 [1 - \exp(-2M)] \tag{4.13}$$

where the first term is the reduced static intensity and the second term $I^u_{TDS} = N f_0^2 [1 - exp\,(-2M)]$ denotes the Thermal Diffuse Scattering (TDS) resulting from uncorrelated displacement of atoms [34], also known as Debye's assumption of independent atomic vibration. (4.13) suggests that if the atomic displacements in a crystal are totally random and uncorrelated, the Debye-Waller factor can be obtained by a simple division of diffraction intensities from dynamic atomic configurations by intensities from static coordinates after correcting the intensities from the effect of thermal diffuse scattering:

$$\begin{aligned} \exp(-2M) &= \frac{I_{\text{snapshot}} - N f_0^2}{I_{\text{static}} - N f_0^2} \\ 2M = -\ln \left(\frac{I_{\text{snapshot}} - N f_0^2}{I_{\text{static}} - N f_0^2} \right) &= \frac{16\pi^2 \langle u^2 \rangle \sin^2\theta}{3\lambda^2} = \frac{16\pi^2 U_{\text{iso}} \sin^2\theta}{\lambda^2} \end{aligned}$$

where U_{iso} is the isotropic displacement value assuming the particle is a monatomic cubic crystal [6]. U_{iso} can be related to the squared atomic displacements averaged over three

orthogonal directions as

$$U_{\text{iso}} = \frac{\langle u^2 \rangle}{3} \tag{4.14}$$

The above assumption of thermally induced dynamic atomic displacements being entirely uncorrelated becomes weak for crystalline solids. In these materials, the displacement of nearby neighbouring atoms always includes correlation effects, and they modify the form of the TDS. Incorporating correlation effects in the TDS calculations requires a more elaborate treatment of atomic displacements in the crystal than the first-order uncorrelated displacement formulation, and can be modelled by adding time-dependent displacement contribution accounting for the thermal fluctuations into scattering amplitude equation as:

$$A_{\text{ins}}\left(\vec{q}\right) = \sum_{j=1}^{N} f_j(2\theta) \exp\left(i\left[\vec{q}\cdot\left(\vec{r}_j + \vec{u}_j\right)\right]\right) \tag{4.15}$$

Here A_{ins} is the instantaneous complex scattering amplitude, $\vec{r}_j$ is the average (time independent) position of j^{th} atom in the crystal and $\vec{u}_j$ is its instantaneous displacement from $\vec{r}_j$. If enough number of instantaneous configurations of the crystal is considered, $< \vec{u}_j >_t = 0$ for each atom where $< >_t$ refers to a temporal average. By multiplying A_{ins} by its complex conjugate, we can formulate an expression for the instantaneous diffraction intensity. Its temporal average then can be written as [34, 35]:

$$\left\langle I_{\text{ins}}\left(\vec{q}\right)\right\rangle_t = \left\langle \sum_{k=1}^{N}\sum_{j=1}^{N} f_j(2\theta) f_k^*(2\theta) \exp\left(i\left[\vec{q}\cdot\left(\vec{r}_j + \vec{u}_j\right)\right]\right) \exp\left(-i\left[\vec{q}\cdot\left(\vec{r}_k + \vec{u}_k\right)\right]\right) \right\rangle$$

$$\left\langle I_{\text{ins}}\left(\vec{q}\right)\right\rangle_t = \sum_{k=1}^{N}\sum_{j=1}^{N} f_j(2\theta) f_k^*(2\theta) \exp\left(i\left[\vec{q}\cdot\left(\vec{r}_j - \vec{r}_k\right)\right]\right) \left\langle \exp\left(i\left[\vec{q}\cdot\left(\vec{u}_j - \vec{u}_k\right)\right]\right)\right\rangle_t$$

This expression can be simplified by replacing $\vec{q}.\left(\vec{u}_j - \vec{u}_k\right)$ by $q(u_{jq} - u_{kq})$, where terms without arrows refer to the magnitude of their counterparts; and u_{jq} and u_{kq} are projections of $\vec{u}$ on $\vec{q}$. If the multiplier of the imaginary term in the exponent has a Gaussian

distribution, further simplification is possible:

$$\langle \exp\left(iq\left(u_{jq}-u_{kq}\right)\right)\rangle = \exp\left(-\frac{1}{2}q^2\left\langle\left(u_{jq}-u_{kq}\right)^2\right\rangle\right)$$

$$\langle \exp\left(iq\left(u_{jq}-u_{kq}\right)\right)\rangle = \exp\left(-\frac{1}{2}q^2\left\langle {u_{jq}}^2\right\rangle\right)\exp\left(-\frac{1}{2}q^2\left\langle {u_{kq}}^2\right\rangle\right)\exp\left(q^2\left\langle u_{jq}u_{kq}\right\rangle\right)$$

Normally, $\langle u_{kq}^2\rangle$ and $\langle u_{jq}^2\rangle$ are not necessarily equal since surface and core regions have different MSDs. However, for computational reasons, we will treat them equally. Later, we will discuss the "local TDS" result that is calculated by using atom-specific MSD. By assuming $\langle u_{kq}^2\rangle = \langle u_{jq}^2\rangle = \langle u_q^2\rangle$ and using the definition of $\exp\left(-\frac{1}{2}q^2\left\langle {u_q}^2\right\rangle\right) = \exp(-M)$, we can rewrite the temporal average of the diffraction intensities in terms of those resulting from static and dynamic coordinates of atoms separately:

$$\begin{aligned}\langle I_{\text{ins}}\left(\vec{q}\right)\rangle_t = &\sum_{k=1}^{N}\sum_{j=1}^{N} f_j(2\theta)f_k^*(2\theta)\exp\left(i\left[\vec{q}\cdot\left(\vec{r}_j-\vec{r}_k\right)\right]\right)\exp(-2M)+\\ &\sum_{k=1}^{N}\sum_{j=1}^{N} f_j(2\theta)f_k^*(2\theta)\exp\left(i\left[\vec{q}\cdot\left(\vec{r}_j-\vec{r}_k\right)\right]\right)\exp(-2M)\left\{\exp\left(q^2\left\langle u_{jq}u_{kq}\right\rangle\right)-1\right\}\end{aligned} \tag{4.16}$$

In the above expression, the first term is the diffraction intensity resulting from static coordinates of atoms in the crystallite reduced by the Debye-Waller factor and the second term is the TDS intensity, $I_{TDS} = I_{TDS}^c + I_{TDS}^u$, resulting from both correlated (I_{TDS}^c) and uncorrelated I_{TDS}^u displacements of atoms. Unlike I_{TDS}^u, I_{TDS} shows peak-like features around Bragg angles, therefore smooth analytical functions are insufficient to approximate their intensity distribution over the scattering angle.

To obtain thermal diffuse scattering intensities, (4.16) was rewritten as:

$$\langle I_{\text{ins}}\left(\vec{q}\right)\rangle_t = I_{\text{static}}\,\exp(-2M) + I_{TDS} \tag{4.17}$$

where the left-hand side is the time average of instantaneous diffraction intensities over 5000 snapshots, i.e. $\langle I_{\text{ins}}\left(\vec{q}\right)\rangle_t = \sum_{i=1}^{5000}\frac{1}{5000}I_{\text{inst}}^i\left(\vec{q}\right)$, $I_{\text{inst}}^i\left(\vec{q}\right)$ is the diffraction intensity for i^{th} snapshot [34] and Debye-Waller factor, *M*, was obtained from real-space calculations of the MSDs presented in Table 1. (In reality, M is different for core and surface atoms

of a given nanocrystals [28]; however, a particle-wide average value resulted in negligible error as discussed later.) Next, I_{TDS} was isolated by subtracting from the time-average snapshot intensity the static intensities reduced by the Debye-Waller factor. These computed TDS intensities were later subtracted from the snapshot intensities before performing Rietveld refinement.

4.4 Rietveld Refinement Methodology

We used the open-access software GSAS II [30] to perform Rietveld refinement on our diffraction datasets. This step consisted of two consecutive Rietveld refinements in which the first refinement was performed on the diffraction data corresponding to the static coordinates (static intensities) and the second one to that of the average diffraction intensities from 5000 instantaneous coordinates for each gold nanocrystal (snapshot intensities). For all datasets, the fitting range of $2\theta \in (17^\circ, 152^\circ)$ was selected. A hypothetical instrument file with unpolarized and perfectly monochromatic X-rays with a wavelength of 1 Å was used.

In the first refinement step, where static intensities were analyzed, the initial values of refinable parameters were selected such that the lattice parameter was 4.07825 Å (from the Crystallographic Information File (CIF) of gold [36]), crystallite size was equal to the nominal size of the particle, profile shape factor (LGmix), microstrain[1] and U_{iso}^R, i.e. isotropic displacements from Rietveld refinement, were left at their default values, 1, 1000 and 0.01 respectively. Six parameters, namely, lattice parameter, arbitrary scale factor, particle size, profile shape factor, microstrain and U_{iso}^R were refined, even though these diffraction data did not include the effects of thermal displacement of atoms. Our goal was to confirm that the refined U_{iso}^R from static intensities was zero, which indeed

[1] Peak broadening in GSAS II is ascribed to microstrain and size. Hence the broadening associated with static atom displacements in our case were refined under isotropic microstrain refinement category.

was the case within the estimated uncertainties reported by the software. Once all static diffraction data were refined individually for the five gold nanocrystal models at all temperatures, the snapshot diffraction data were refined. In this refinement, we used the same initial values for the lattice parameter, LGmix, and particle size, except that 1) the microstrain values were initialized to the resulting microstrain value of the corresponding refined static intensity, and their further refinement was not allowed, and 2) U_{iso}^{R} was initialized at its default value (0.01) and allowed to refine. This refinement strategy was similar to a previous study [3] and consistent with the definitions of static and dynamic atomic displacements in our nanocrystalline particle models. An example of a successful Rietveld refinement can be seen in Figure 4.1, and the results of all Rietveld refinements are presented in Table 4.1.

Figure 4.1: *Rietveld refinement result of the diffraction profile of 5-nm-diameter gold nanoparticle at 300 K. The inset shows the observed and calculated (refined) intensities from 100° to 150°. TDS indicates the thermal diffuse scattering, which was subtracted before refinement.*

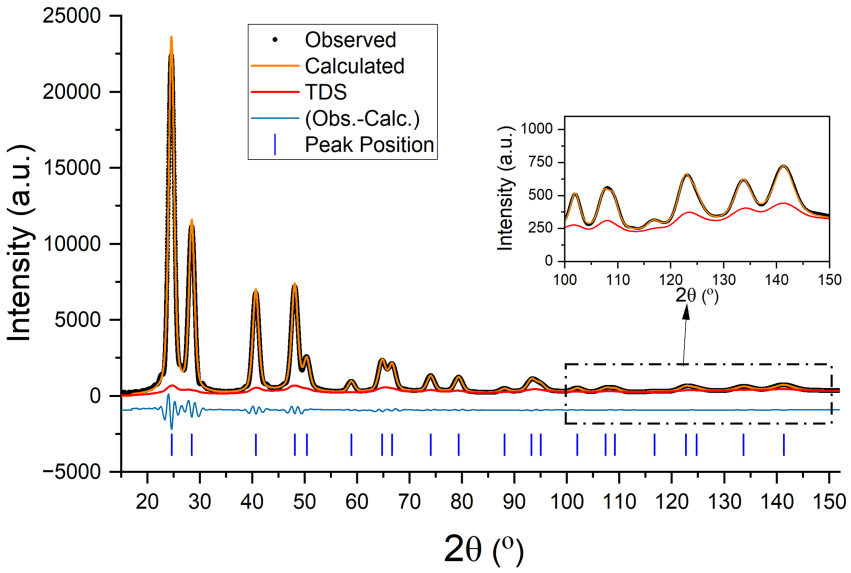


Table 4.1: *Results of the two-step Rietveld scheme on snapshot intensities of our gold nanocrystals. (Only at 0 K the refined values are from static diffraction data.) % wR stands for the weighted residuals of the refinement reported by GSAS II, and it is used to evaluate the success of the refined crystallographic model. Values in parentheses are uncertainties reported by the software.*

Size (nm)	Temp. (K)	Crystal size (nm)	Lattice parameter (Å)	LGmix	rms strain (x10^3)	U^R_{iso} (x10^{-3}Å^2)	% wR
5	0	4.3	4.05381 (7)	0.338 (2)	4.70 (9)	0.02 (2)	9.69
	10	4.29	4.05406 (7)	0.337 (2)	4.70 (9)	0.37 (2)	9.73
	100	4.27	4.05870 (8)	0.334 (2)	4.77 (9)	3.63 (3)	9.65
	200	4.31	4.06418 (8)	0.336 (2)	4.83 (9)	7.50 (3)	9.56
	300	4.29	4.07014 (9)	0.333 (2)	4.94 (9)	11.47 (3)	9.55
10	0	8.58	4.05940 (3)	0.339 (2)	1.45 (4)	0.03 (2)	9.85
	10	8.6	4.05909 (3)	0.339 (2)	1.52 (4)	0.31 (2)	9.80
	100	8.64	4.06355 (3)	0.339 (2)	1.52 (4)	3.14 (3)	9.69
	200	8.59	4.06879 (3)	0.335 (2)	1.53 (4)	6.59 (3)	9.54
	300	8.59	4.07445 (4)	0.334 (2)	1.54 (4)	10.16 (3)	9.45
15	0	13.06 (10)	4.06158 (2)	0.338 (2)	0.58 (2)	0.06 (2)	9.93
	10	13.19	4.06062 (2)	0.339 (2)	0.73 (2)	0.31 (2)	9.69
	100	13.16	4.06503 (2)	0.337 (2)	0.73 (2)	3.01 (2)	9.55
	200	13.24	4.07025 (2)	0.338 (2)	0.74 (2)	6.22 (3)	9.42
	300	13.24	4.07587 (2)	0.337 (2)	0.75 (2)	9.78 (3)	9.31
20	0	16.84 (10)	4.06232 (1)	0.337 (2)	0.31 (2)	0.05 (2)	9.43
	10	17.08 (10)	4.06122 (1)	0.338 (2)	0.51 (2)	0.32 (2)	9.59
	100	17.06 (10)	4.06563 (2)	0.337 (2)	0.51 (2)	2.95 (2)	9.46
	200	17.06 (10)	4.07085 (2)	0.336 (2)	0.51 (2)	6.07 (3)	9.33
	300	17.14 (10)	4.07646 (2)	0.336 (2)	0.51 (2)	9.59 (3)	9.22
30	0	25.15 (10)	4.06258	0.336 (1)	0.14 (1)	0.02 (2)	8.82
	10	25.58 (10)	4.06185	0.338 (2)	0.29 (1)	0.30 (2)	9.33
	100	25.51 (10)	4.06627	0.337 (2)	0.28 (1)	2.86 (2)	9.23
	200	25.53 (10)	4.07149 (1)	0.335 (1)	0.29 (1)	5.96 (3)	9.12
	300	25.47 (10)	4.07709 (1)	0.333 (1)	0.29 (1)	9.45 (3)	9.04

4.5 Comparision of the Real Space and Extracted Structural Parameters from the Rietveld Refinement

4.5.1 Lattice Parameter and CTE

Here, the extracted lattice parameters from the diffraction analysis are compared with true lattice parameters from the atomic model at finite temperatures. In addition, we look at the dependence of lattice parameters on temperature and compare thermal lattice strains (ε_{th}) and Coefficient of Thermal Expansion (CTE) from both analyses.

Figure 4.2: *Temperature (a-e) and particle size dependence (f-i) of lattice parameters obtained from real-space and diffraction analyses.*

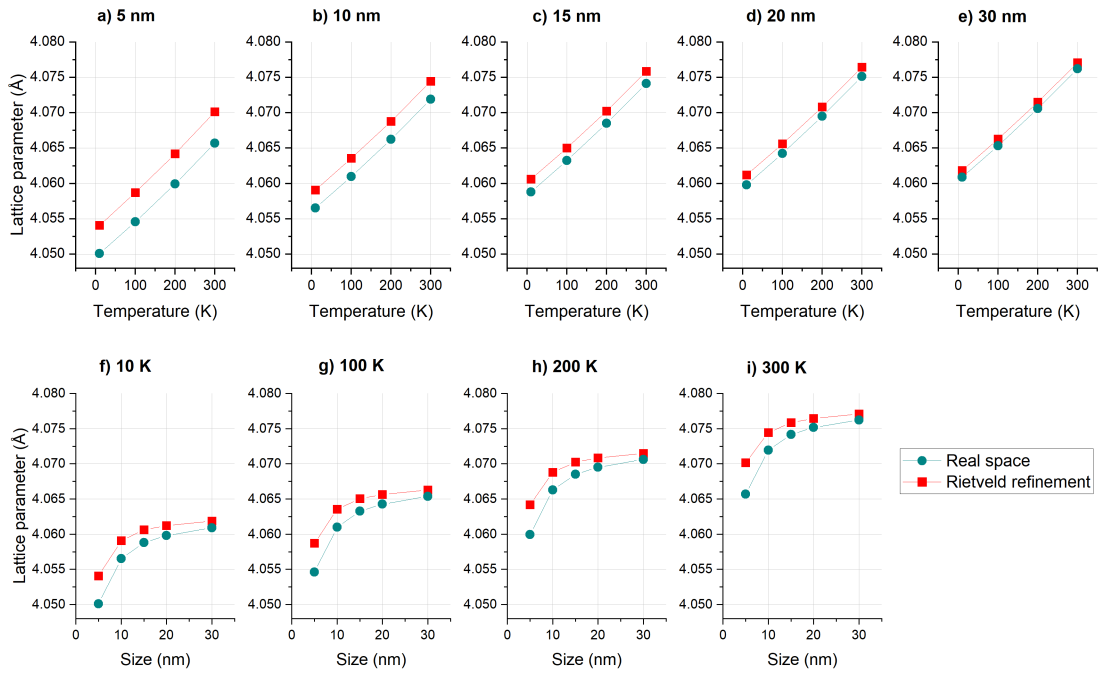


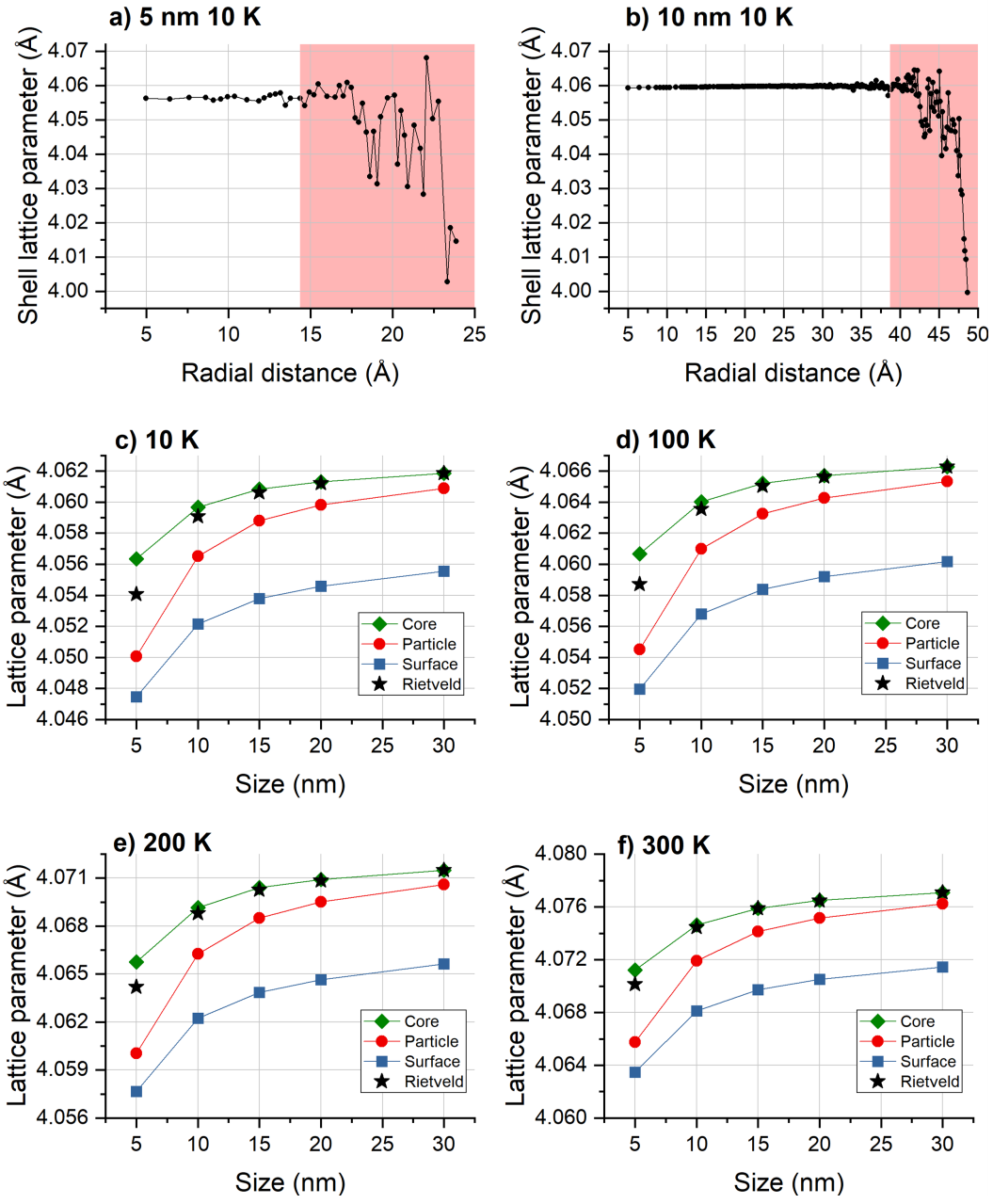
Figure 4.2 summarizes both the temperature and particle size dependencies of average lattice parameters obtained from real-space and diffraction analyses. At first sight, both methods agree quite well in capturing the size and temperature-related trends: Average lattice parameters are linearly dependent on temperature for all nanoparticle sizes

(Figure 4.2(a-e)), and they increase with increasing size for all temperatures considered (Figure 4.2(f-i)). Unlike temperature dependence, crystallite-size dependence is nonlinear for lattice parameters. Secondly, lattice parameters obtained from real-space analysis are always lower than those from diffraction analysis for all nanocrystal sizes and temperatures considered. Remembering that diffraction analysis, unlike real-space calculations, captures structural information mainly from the core region of the particle where a coherent crystalline domain is present, this indicates that the lattice parameters from surface regions of the nanocrystals must be smaller than those of the core regions. To confirm this, we divided our static nanocrystal models into concentric spherical shells and computed average lattice parameters within each shell volume. As Figure 4.3(a-b) show, large variations in local lattice parameters are noticeable within the outermost shell with 10 Å thickness for both 5 nm and 10 nm gold nanocrystals at 10 K. This trend repeats itself for all other nanocrystals and at higher temperatures as well. Hence, we selected the outermost 10 Å thickness as our effective surface-layer thickness and plotted the average lattice parameter within this layer in addition to the particle-wide and core volume averages of lattice parameters for all nanocrystal models and at all temperatures. These are shown in Figure 4.3(c-f). As expected, the lattice parameters from the surface layers of all nanocrystals are smaller than particle-wide average lattice parameters. Moreover, the deviation between particle- and surface-averaged lattice parameters increases with increasing particle size due to particle-averaged lattice parameters being more dominated by lattice parameters of the core for larger nanocrystals. Focusing on real-space and reciprocal-space discrepancy, the largest deviation between the Rietveld-refined lattice parameter and particle-wide average lattice parameter reaches 0.109 % and is observed at 300 K for the 5 nm particle. For the same temperature and particle, the deviation of the refined lattice parameter from the core and surface lattice parameter is found as 0.027 % and 0.166 %, respectively. These results confirm that Rietveld-refined lattice parameters

closely follow core lattice parameters which are larger than both the surface and particle-wide average lattice parameters. Interestingly, core lattice parameters, similar to surface-wide and particle-wide average values, also show a particle size dependence, increasing with increasing nanocrystal size. This indicates that atoms in the surface layers have an influence on the average periodicity of atoms in the core regions, and this influence is greater when the separation between the core and surface layer is small. Similar observations were reported in a previous study from MD simulations on CdSe nanocrystals [37]. All in all, particle-wide average lattice parameters computed from static coordinates of small gold nanocrystals are always below their counterparts from Rietveld refinement, and Rietveld-refined average lattice parameters agree better with core lattice parameters from real-space calculations. However, this agreement degrades for smaller nanocrystals at all temperatures. This is because of the extremely small number of unit cells within each nanocrystal violating the infinitely periodic electron distribution expected in the particle and was confirmed from the Rietveld analysis of simulated diffraction data from ideal crystalline gold nanoparticles as well [2].

Next, we investigate the thermal strains (ε_{th}) and CTE. Figures 4.4(a-e) show the variation of thermal strains with respect to temperature from real-space analysis of nanocrystals, using relative change in both average crystallite diameters and average lattice parameters, as well as from Rietveld refinement based on relative change in lattice parameters. Figure 4.4(f) reports the results of the same calculations on the bulk system. We can see that the results of all three calculations agree very well, and the thermal strains are almost identical. However, small variations in the thermal strains with respect to nanocrystal size are present at all temperatures. That means variations in CTE are expected with changing crystal size. We note that for the bulk system, the slight deviation between the thermal strains from Rietveld-refined and real-space-calculated lattice parameters results from the limited crystal size assumed in the bulk model. By increasing

Figure 4.3: *(a-b) Local variation of average lattice parameters within concentric shell volumes with respect to their distance from the particle center. The areas shaded in red indicate surface thickness. (c-f) Average lattice parameters over the particle volume (red), over the core volume (green) and over the outermost surface layer (blue) with respect to the nominal particle size at 10, 100, 200 and 300 K. Stars shown in black refer to Rietveld-refined lattice parameters.*



the size to 10 nm, we observed that the deviation almost disappeared.

Figure 4.4: *Thermal strain vs. temperature obtained from real-space calculations using average lattice parameter (red markers), average particle diameter (blue markers), and from Rietveld refinement using average lattice parameter (orange markers) for 5 nm, 10 nm, 15 nm, 20 nm, and 30 nm nanoparticles and bulk gold crystal (5 nm). Dashed lines are linear fits.*

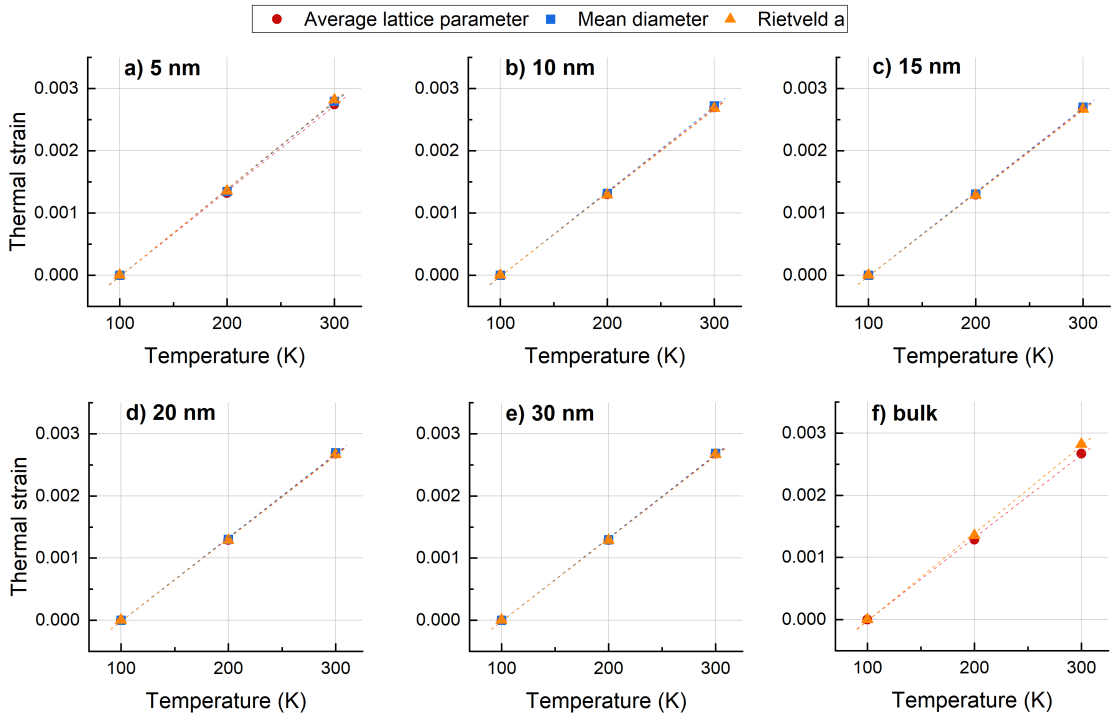
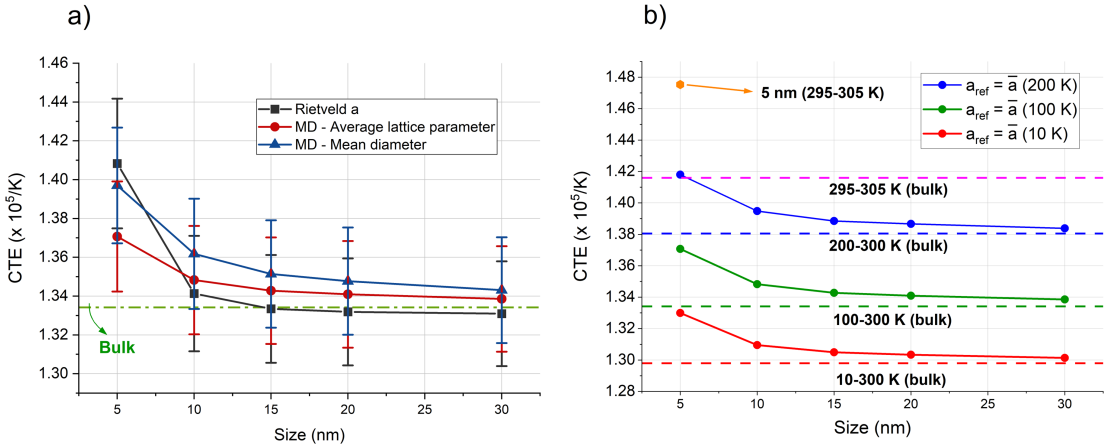


Figure 4.5(a) shows the variation of average CTEs with crystal size using both real-space and diffraction analyses. In both cases, values were obtained from the slopes of the best-fitting lines to the thermal strain (based on lattice parameter variations) vs. temperature plots over the interval of 100-300 K. As seen, the values obtained from both methods agree within error bars and a decrease in the CTEs is observed as the diameter of the particles increases. This can be explained by the effect of a decreased proportion of surface atoms as the size of the particle increases: Since atoms within the surface layer of the particles are undercoordinated, the average bond strength between them is

lower than those of core atoms. Hence a higher proportion of surface atoms within a particle results in a decrease in the overall interatomic bond strength. Since the amount of thermal expansion is inversely proportional to the bond strength, larger particles having a smaller proportion of surface atoms and, therefore stronger interatomic forces on average are expected to have smaller CTE values compared to smaller particles. Similar findings were reported for polycrystalline Ni and Cu thin films as well [38].

Figure 4.5: *a) CTE vs. nanoparticle size based on average lattice parameters and diameters from real-space calculations (MD) and Rietveld analysis (100-300 K). Error bars refer to fitting errors of the slopes for MD-based calculations (obtained from Figure 4.4). b) MD-based average CTEs computed from mean lattice parameters for different reference temperatures.*



One may note in Figure 4.5(a) that the MD-based calculation for bulk gold (green) is approximately 13.33 x 10^{-6} K^{-1} which is lower than the literature value of CTE for gold, 14.2 x 10^{-6} K^{-1} [39]. This difference results from the formulation of CTE we used in our calculations: as previously mentioned, the values shown in Figure 4.5(a) are the slopes of the thermal strain vs. temperature graphs seen in Figure 4.4, corresponding to average CTE of the material over the temperature interval of 100-300 K. Since CTE depends on

the temperature, its average value is influenced by the reference temperature interval selected in the calculation. The effect of the reference temperature on the computed CTEs is visualized in Figure 4.5(b). As seen, keeping the upper temperature bound constant at 300 K while increasing the lower bound of the temperature from 10 to 200 K causes a vertical shift in the computed CTEs for all sizes of gold nanocrystals (markers connected by solid lines), indicating that the computed CTEs increase with increasing reference temperature. Similar increase in the CTEs is obtained from the MD modelling of bulk gold crystal as well (dashed lines). The increase in the average CTE with decreasing temperature interval is a natural result of the temperature dependence of CTE [40]. However, regardless of the temperature interval selected in the calculation, CTEs of gold nanocrystals are always greater than that of the bulk gold model. The purple dashed lines seen in Figure 4.5(b) show the bulk CTE calculation over a much smaller temperature interval of 295-305 K and pass from a value that is slightly lower than 1.42 x 10^{-6} K^{-1}. This shows that if a much smaller temperature interval is selected in the MD runs, the CTE converges to the reference value of bulk gold and validates our MD calculations once more. Finally, over the limited temperature interval of 295-305 K, the CTE of the 5 nm gold nanocrystal is computed to be below 1.48 x 10^{-6} K^{-1}, which corresponds to a 4 % increase in the CTE with respect to that of bulk gold.

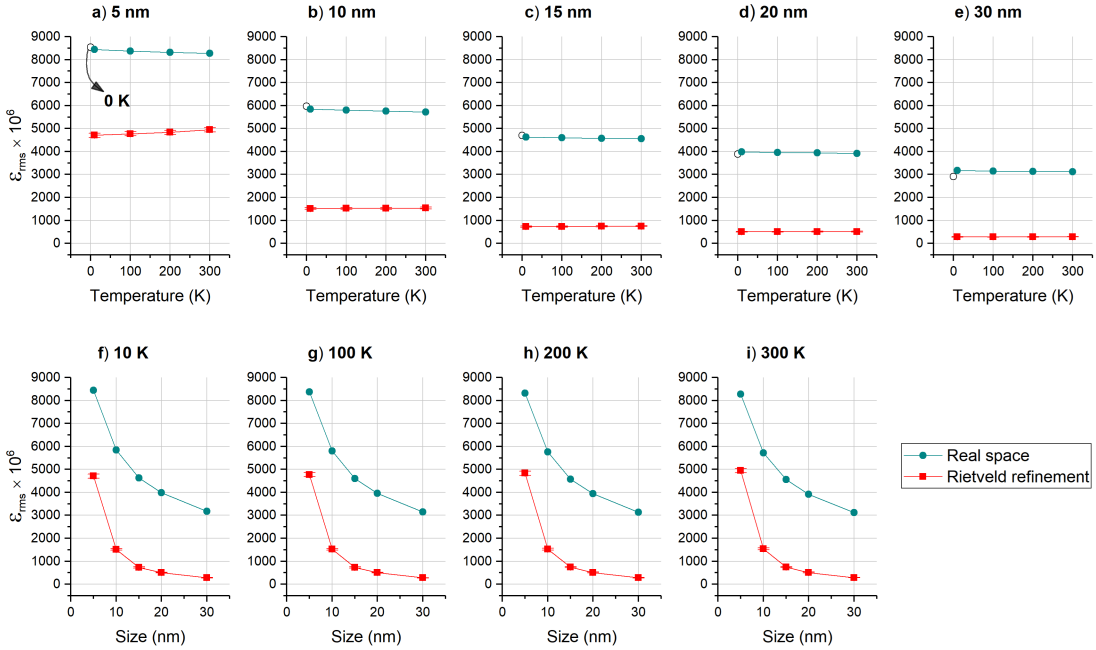
4.5.2 Static Displacement

Figure 4.6 presents the mean lattice strains (in rms form) computed from both real-space and Rietveld analyses and their variations with respect to temperature (Figure 4.5(a-e)) and crystallite size (Figure 4.5(f-i)). First, for all nanocrystal sizes, both real-space and Rietveld analyses predict almost no variation in rms strains with respect to temperature. This trend is supported by previous literature as well [41, 42]. It validates for nanocrystalline powders that if the temperature of a defect-free crystal increases, the reduction in

the Bragg intensities is accounted for by the Debye-Waller factor and the TDS component, satisfying energy conservation and leaving no room for additional peak broadening [32]. Real-space calculations show that among different nanocrystals, the smallest ones show the largest rms strains as expected. This can again be explained by the higher proportion of surface atoms in smaller nanocrystals and the enhanced static displacement amplitude of surface atoms compared to core atoms. Secondly, for all nanocrystals real-space calculations of rms strains are significantly higher than those from Rietveld refinement. (Our Rietveld-refined lattice strains are comparable with past literature [3] reporting Rietveld refinement results of small gold nanocrystals at 0 K: in Figure 12 of that study, the reported rms strain for a 10 nm gold nanocrystal is $\epsilon \approx 1400$, which is comparable with our calculation of 1454 for the same size and at 0 K.) This incompatibility stems from the following factors: 1) In Rietveld analysis, rms strains are computed from the remaining peak broadening after size-related peak broadening is accounted for. Since the fundamental portion of intensities to each Bragg peak is contributed by the core atoms of the particle, the refined lattice strains belong to the lattice strains of the core regions of the particle. In other words, enhanced static displacements of the outermost surface atoms are not fully visible to the Bragg peaks. 2) The accuracy of rms strains from Rietveld refinement depends on how accurately the crystal size is estimated. Hence, errors associated with the apparent crystallite sizes directly propagate to obtained rms strains as well. Unfortunately, large correlation between refined parameters (LGmix, average crystallite size, microstrain) makes it very difficult to isolate the source of inaccuracies in refined lattice strains from Rietveld refinement.

To understand the variation of rms strains from the core to the surface of the nanocrystals, we extracted local and particle-averaged rms strains from real space calculations, which can be seen in Figure 4.7. In addition, Rietveld-refined strains are added for comparison as dashed lines. Here the discrete markers show the computed local rms

Figure 4.6: *Root-mean-square (rms) strain vs. temperature for a) 5 nm, b) 10 nm, c) 15 nm, d) 20 nm, and e) 30 nm diameter gold nanocrystals (empty circles show rms strains computed at 0 K) and rms strain vs particle diameter at f) 10 K, g) 100 K, h) 200 K and i) 300 K obtained from real-space analysis and Rietveld refinement of snapshot intensities. (error bars are within marker size in Rietveld refinement).*



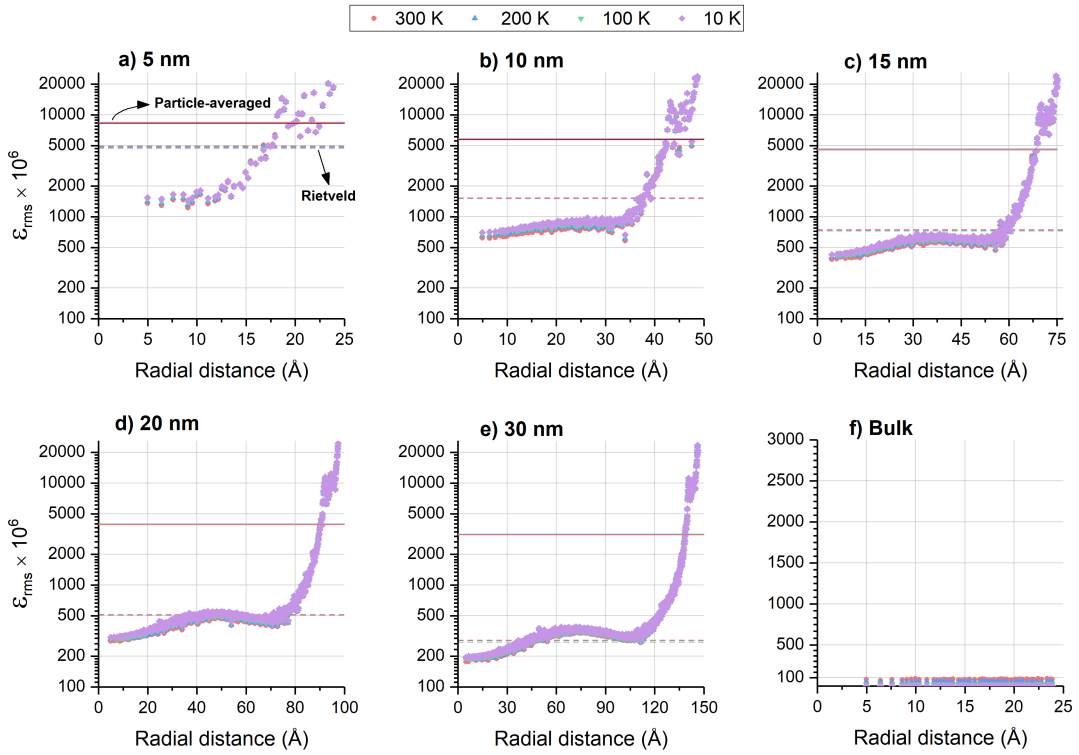
strains with respect to a particular radial distance from the particle center, and straight lines show the particle-wide mean rms strains. For all sizes considered, the local rms strains are relatively constant over the core region of the nanoparticles. Within the surface layer, the local rms strains shoot up exponentially. Although the rms strains of the surface layers all approach the same value ($\epsilon \approx 20000$) irrespective of the particle size, rms strains of the core regions are clearly dependent on particle size, and they decrease for larger nanocrystals. This also explains why we observe a nonlinear decay in both real-space and Rietveld-refined rms strains as the particle size increases: For larger nanocrystals, a larger proportion of the atoms sit in the core regions and core atoms of larger particles already have lower rms strains. As the particle size decreases, the core-region

rms strains increase simultaneously with increasing proportion of surface atoms both of which push the mean rms strains upward for smaller nanocrystals. However, compared to real-space calculations, the decay in the Rietveld-refined rms strains as particle size increases is faster than that of real-space calculations; because for larger nanocrystals a higher proportion of the atoms sits in the core and contributes intensity to the Bragg peak, making the relative intensity contribution of surface atoms to negligible values. These observations are similar to findings in past literature [3] and confirm the inadequacy of homogeneous strain description and mean rms strains to represent the static displacement field inside nanocrystalline particles. Moreover, they demonstrate that Rietveld-refined rms strains more closely follow the rms strains of the core regions as the particle size increases. Similar conclusions were reported in the past literature [43]. Finally, for the bulk nanocrystal model (Figure 4.7(f)), the rms strains both from real space calculations and from Rietveld refinement are negligible as expected.

4.5.3 MSD

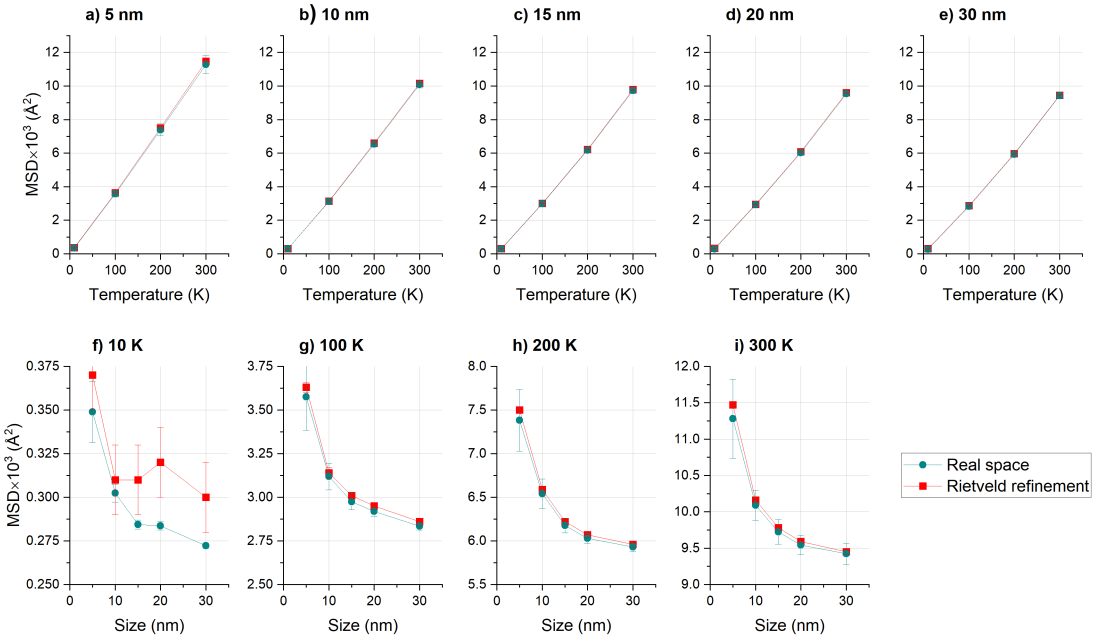
Lastly, we investigate how the MSDs computed from U_{iso} in Rietveld refinement compare with real-space calculations over different particle sizes and temperatures. Figure 4.8 summarizes our findings. Note that our real-space calculations did not include values at 0 K, and at 10 K, the MSD values were slightly higher than 0 regardless of particle size, since atomic vibration was not activated much at such low temperatures. (The validity of our selected force field at temperatures lower than 100 K is an active discussion [13]; however, we performed our calculations at 10 K to see how the extracted MSDs compared with higher temperatures as well as with 0 K). As seen in Figures 4.8(a-e), both diffraction and real-space analyses predict similar trends; MSDs increase appreciably with increasing temperature, and their variation seems to be linearly correlated with temperature for all nanocrystals. This linear relation between temperature and MSD is consistent

Figure 4.7: *Local (discrete markers) and particle-averaged rms strains (solid lines) obtained by real-space calculations for the gold nanocrystals with a) 5 nm, b) 10 nm, c) 15 nm, d) 20 nm, e) 30 nm diameters and f) bulk crystal model (5 nm) at 4 different temperatures between 10 and 300 K. Dashed lines are Rietveld-refined rms strains.*



with past studies both in experimental observations [41, 44] and theoretical calculations. Secondly, for all nanocrystal sizes, MSDs predicted by real-space calculations agree very well with those from the Rietveld analysis, indicating that TDS-corrected snapshot intensities closely match with the intensity predictions of the Rietveld model. Therefore for accurate Rietveld analysis of diffraction data from small nanocrystals, TDS correction is critical even at temperatures well below the melting point. Looking at size dependencies, Figures 4.8(f-i) show that increasing nanocrystal size is accompanied by a smooth decrease in the MSDs from both methods at all temperatures except 10 K: Rietveld-refined MSDs at 10 K are finite but very low indicating practically little to no atomic vibration;

Figure 4.8: *MSD vs. temperature for a) 5 nm, b) 10 nm, c) 15 nm, d) 20 nm, and e) 30 nm diameter gold nanocrystals and MSD vs. particle diameter at f) 10 K, g) 100 K, h) 200 K and i) 300 K temperature obtained from real-space and Rietveld refinement analyses. Error bar results indicate standard deviations in real-space calculations and fitting errors in Rietveld refinement.*



therefore their fluctuations must result from numerical errors associated with the refinement (The reported estimated uncertainty in MSD from GSAS II for 20 nm nanocrystal at 10 K is 0.02×10^{-3} Å^2). This size dependency of MSD is confirmed by past works [41, 45, 46].

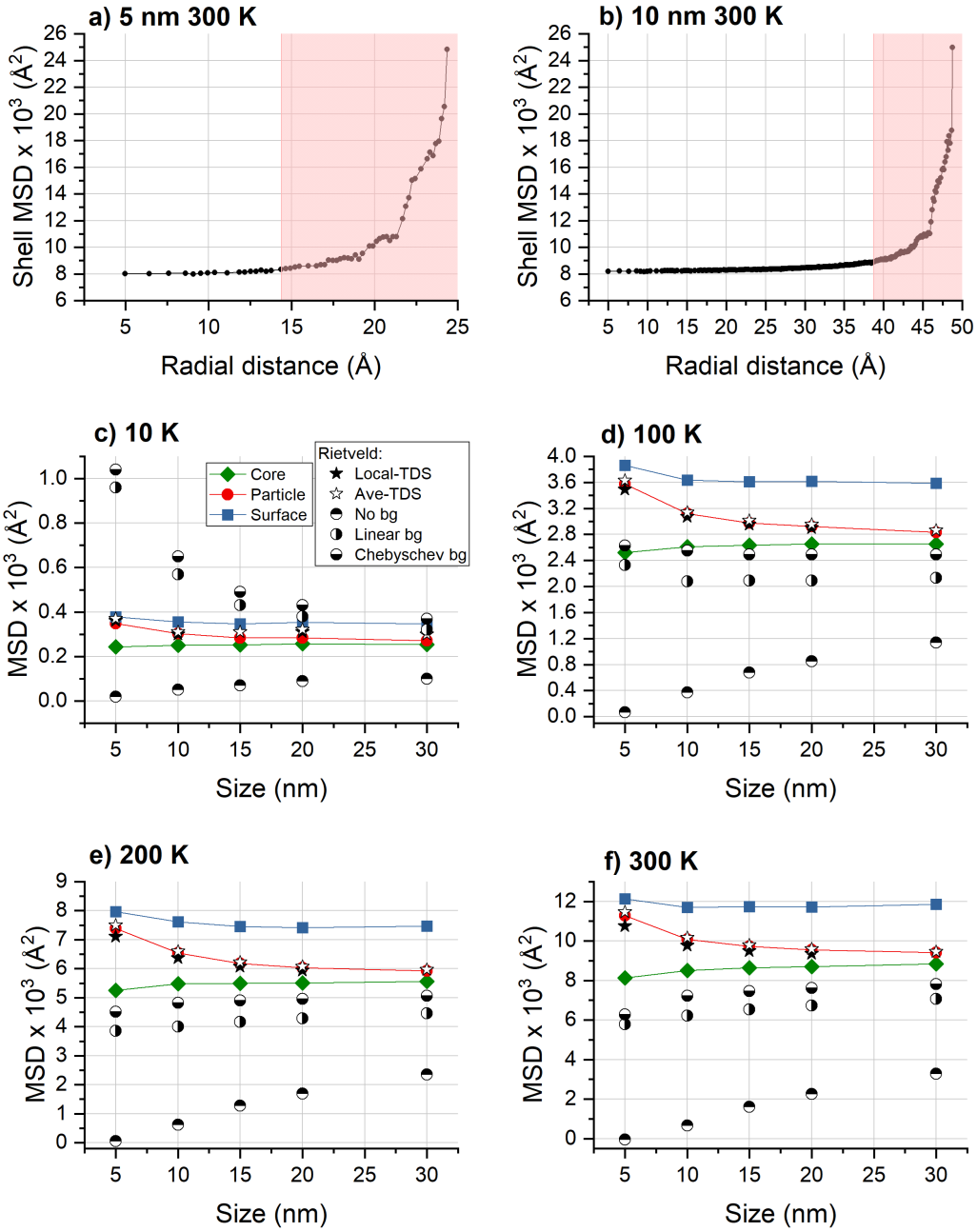
Looking at local variations, the radial change of MSDs from particle center to surface at 300 K (5 and 10 nm) is given in Figures 4.9(a-b). Similar to previous sections, the surface region (red) is the outermost layer with a thickness of 10 Å and atoms outside this region are considered within the core region. Each data point represents the average MSD of atoms in a spherical shell of thickness 0.125 Å located at that radial distance. From the figure, we see that local MSDs are independent of radial distance in the core region

while they increase non-linearly with radial distance in the surface region. The maximum MSD, which is approximately three times higher than that of the core region, is observed at the outermost layer [18]. To investigate whether such large local variations in MSD affect the Rietveld-refinement results, we calculated the average atomic MSDs in the core region, surface region, and whole particle and then compared them with those extracted from Rietveld refinement. In Figures 4.9(c-f), we observe that the particle-wide average MSD shows relatively stronger particle size dependence than the local core and surface MSDs at all temperatures and approaches to the core MSD as particle size increases. This is reasonable since the surface-to-volume atom ratio decreases as well. In the case of Rietveld-refined MSDs, we performed the refinement after subtracting from the snapshot intensities two different types of TDS contribution: the "Rietveld-ave" represents MSD from Rietveld refinement after modeling the TDS component based on a single, particle-averaged MSD (same as Figure 4.8). "Rietveld-local", however, models the TDS component based on the exact atomic MSDs of each atom. Obviously, the assumption of all atoms having the same MSD allowed the TDS calculation with less computation power since atom pairs could be grouped based on interatomic distance (similar to the Debyer algorithm [25]), while the latter case required evaluation of each atom pairs separately, making the calculations prohibitively expensive for larger particles. Still, we were able to obtain the local-atomistic TDS of particles up to 20 nm, as shown in the figure. It turned out that Rietveld refinement was almost insensitive to the local distribution of atomic MSDs throughout the particle since MSDs from "Rietveld-ave" and "Rietveld-local" were almost the same as shown in the figure. Their maximum difference was 0.00072 $Å^2$ at 5 nm 300 K, which decreased with increasing particle size. Comparing real-space and reciprocal-space analyses, we observe that Rietveld MSD agrees with the particle-wide MSD rather than the core MSD at all particle sizes. For example, deviations of "Rietveld-local" MSD from real-space "Particle", "Core", and "Surface" are found

as -4.71 %, 32.11 %, and -11.41 %, respectively, at 5 nm 300 K. This is different from the agreement observed in static atomic displacement parameters (r.m.s strain and average lattice parameter), in which Rietveld results agreed better with the nanocrystal 'core' rather than the particle-wide average.

Lastly, we performed Rietveld refinements of snapshot intensities without subtracting the analytical TDS component to observe the effect of TDS removal on the accuracy of the refined MSD. To be consistent with standard diffraction analysis, the refinement is performed in a single step, and no information was used from the refinement of static intensities. Rather than analytical calculations, here, TDS was approximated with two simple background functions: linear interpolation and Chebyshev polynomials. In addition, a third refinement with zero background was performed. For these refinements, scale factor, lattice parameter, microstrain, Uiso, background function, particle size and LGMix were refined in order, after initializing them with their default values in GSAS II and the CIF file of Au, except particle size, which can be independently obtained from TEM measurements. Unless it was assumed to be zero, the background was refined by a single parameter in linear interpolation and 3 parameters in the case of Chebyshev polynomial. We note that a high number of coefficients in background functions gave rise to correlations between parameters, and no improvement was obtained. Therefore we limited them to 3 coefficients for the Chebyshev polynomial. Results of these 3 separate refinements are labeled as "Rietveld-No bg", "Rietveld-Linear bg", and "Rietveld-Chebyshev bg" in Figures 4.9(c-f). The following comparisons are made by excluding 10 K data since MSD was too low to have a reliable comparison between different methods. As seen, when zero background is used in refinements of snapshot intensities, we observe high refinement error (Rw), and deviations of MSD from real-space calculations are relatively high. For example, the difference between MSD of "Rietveld-No bg" and "Particle"

Figure 4.9: *a-b) Radial change of MSD at 300 K for 5 and 10 nm particles, respectively. The colored region is the surface region with a thickness of 10 Å. c-f) Size-dependent change of real-space and Rietveld MSD at temperature range 10-300 K. Definitions of each data are given throughout the text.*



was found as -11.32$\times 10^{-3}$ Å^2 at 5 nm 300 K. Even though these deviations tend to decrease with increasing particle size, we classify this method as the poorest performer. In the case of linear interpolated background, MSDs are again underestimated. For example, the difference between "Rietveld-Linear bg" and "Particle" was calculated as -5.49$\times 10^{-3}$ Å^2 at 5 nm 300 K, which is less deviated compared to "Rietveld-No bg". Among the three methods, "Rietveld- Chebyshev bg" has higher accuracy with -5.01$\times 10^{-3}$ Å^2 deviation from "Particle" at 5 nm 300 K. Relatively better result of this method is attributed to the nonlinear behavior of TDS intensity. Furthermore, "Rietveld-Chebyshev bg" estimates MSDs to be similar to "Core" MSD in real-space. Finally, all of the above models are still insufficient at estimating actual TDS intensity, as obvious from the underestimated MSD values, and they also result in overestimated rms strains to compensate for the missing background.

4.6 Summary and Conclusions

In this chapter, we applied the Rietveld refinement on powder X-ray diffraction patterns of spherical nanocrystals with diameters below 30 nm at 10, 100, 200, and 300 K temperatures obtained from the MD simulations. The Rietveld refinement algorithm assumes the underlying structure is a lattice structure with periodic unit cells, which is not true in the case of realistic nanocrystals with surface contraction. This incompatibility resulted in some errors in extracted structural parameters - lattice parameters, rms strains, and isotropic displacement parameters. We can list the following conclusions from the chapter:

- Average lattice parameters from real-space and reciprocal-space analyses agreed within 0.1 % for 5 nm nanocrystals, and the agreement improved with increasing nanocrystal size. In both real-space and reciprocal-space calculations, average lattice parameters were found to increase with increasing temperature and nanocrystal

size. Real-space calculations of local lattice parameters showed a substantial decrease in the lattice parameters within the outermost shell of all nanocrystals; however, Rietveld-refined lattice parameters closely followed the lattice parameters of the core regions. In addition to the particle-wide average values, core lattice parameters were found to be size-dependent. This was explained by the close proximity of the surface atoms to the core regions in small nanocrystals. Finally, CTEs computed from average lattice parameters and nanocrystal diameters were consistent between real-space and reciprocal-space calculations.

- Average lattice strains in the form of rms strains remained constant with changing temperature but substantially decreased with increasing particle size in both Rietveld and real-space analyses. A hypothetical bulk crystallite of the same size as a 5 nm nanocrystal with no surface layer resulted in near zero lattice strains indicating that the finite lattice strains in smaller nanocrystals solely originated from the displacement of the undercoordinated surface atoms. Similar to the core lattice parameters, core rms strains were also size-dependent, and they decreased with increasing nanocrystal size. Rietveld refinement was found to significantly underestimate these rms strains of small gold nanocrystals within our temperature range. The reasons were; (1) static displacements of surface atoms were partially visible in the diffraction data and were not captured by the Rietveld refinement, (2) both small size and lattice strains were modelled in the peak broadening and refined average crystal sizes had errors associated with the refinement error, (3) the description of uniform strain was inapplicable to describe the static displacement field inside the investigated nanocrystals. Finally, Rietveld-refined rms strains closely followed the lattice strains from the core regions of the nanocrystals with better agreement as the particle size increased.

- MSDs followed a linear relationship with temperature for all particle sizes in both real-space and diffraction-based formulations, but a nonlinear size dependence was present at temperatures of 100 K and higher. Larger nanocrystals resulted in smaller MSDs compared to smaller particles. The agreement between MSDs from real-space and Rietveld refinement was within 5 %. This was attributed to the proper handling of TDS. We showed that, if information about TDS intensities is unavailable, a reasonable number of Chebyshev polynomials can be used to approximate the TDS component, albeit with an error of nearly 45 % for 5 nm gold nanocrystal at 300 K. For larger nanocrystals and at lower temperatures, this error is expected to decrease.

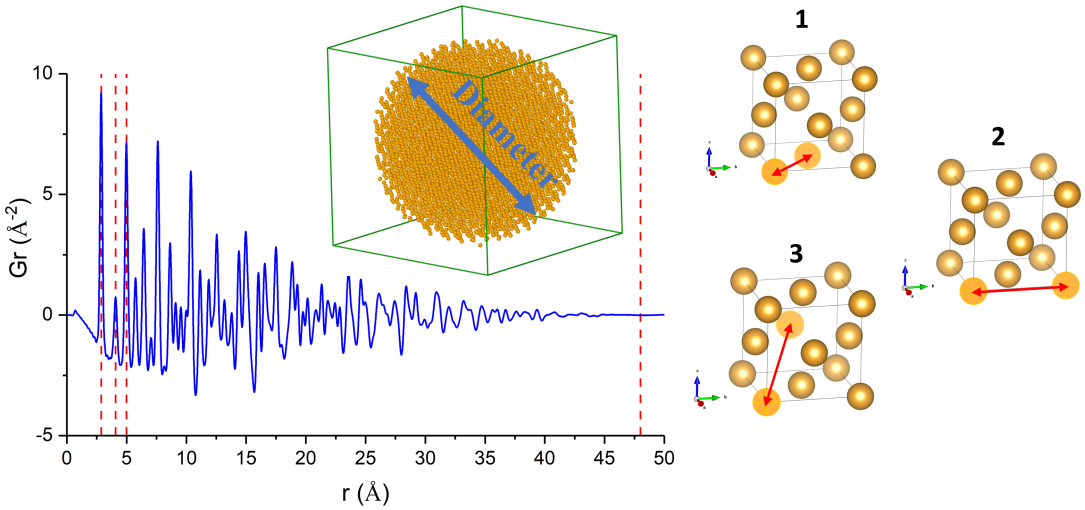
5. PDF ANALYSIS OF REALISTIC GOLD NANOCRYSTSALS

5.1 Introduction

PDF gives the probability of finding atom pairs at a given interatomic distance in a material, and it can be obtained by Fourier transforming normalized powder diffraction intensity. The technique is used to study short- and intermediate-range order in materials [47]. PDF plot for 5 nm nanocrystal at 300 K is shown in Figure 5.1 (left). In the figure, while the x-axis is interatomic distance, the y-axis is Gr function that gives a peak whenever there is a strong atom-atom correlation at that interatomic distance. For example, the first three peak positions shown with red vertical dashed line correspond to interatomic distances shown with the arrow in Figure 5.1 (right) inside an FCC unit cell of gold structure. While the first interatomic distance is observed between the corner and face-centered atom, the second and third interatomic distances correspond to corner-corner and corner-opposite face-centered atom pairs. Therefore, PDF can be considered as a map of interatomic distances. Obviously, the edge length (lattice parameter) of the cubic unit cell will shift PDF peaks to the right (if enlarges) or to the left (if shrinks). Hence, the lattice parameter can be obtained from the PDF peaks. In addition, particle size can be extracted from the PDF by detecting the interatomic distance at which almost all peaks are decayed. This can be explained by considering that no atom-atom correlation is possible beyond particle diameter. Here, the particle diameter for the 5 nm nanocrystal is shown as the last vertical dashed line in Figure 5.1 (left). Lastly, the amount of thermal disorder (or MSD) can be extracted from the PDF peak widths. With increasing temperature, the kinetic energy of nanoparticles increases as well. This is accompanied by atom vibrations to longer distances. Hence, atom-atom bond distances fluctuate around the mean bond distance. This is reflected as broadened PDF peaks as shown for the first 3 PDF peaks of 5 nm

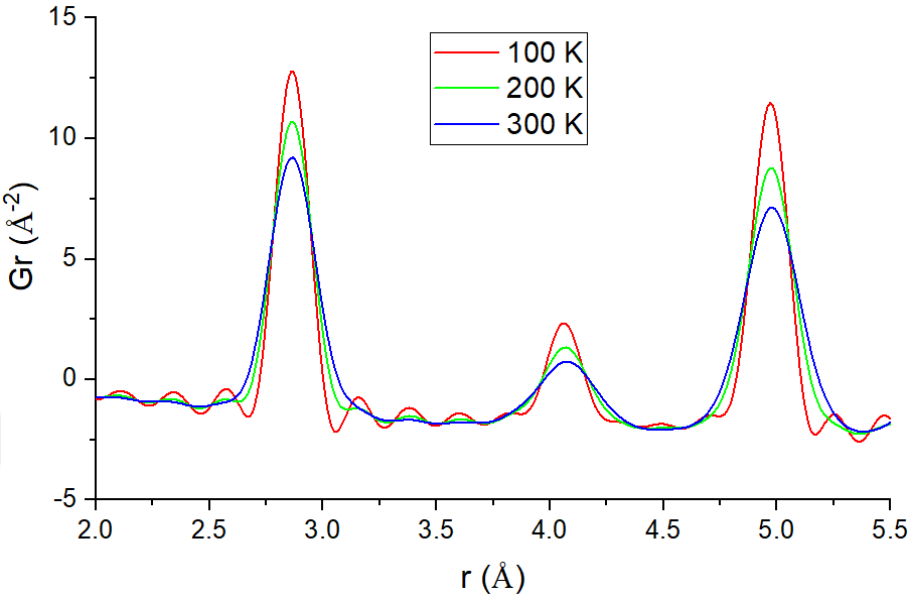
nanocrystal at 100 K, 200 K, and 300 K temperatures in Figure 5.2. All of these structural parameters can be extracted in a model-free way by fitting appropriate profile functions to the measured PDF. However, in the real world, nanocrystals are polydispersed, making particle size extraction challenging. In addition, the presence of more than one phase in the measured sample increases the complexity of doing a model-free analysis. Hence, PDF refinements, which consider whole PDF pattern at once rather than separate peaks using some model structure, are performed to extract structural parameters in a reliable way.

Figure 5.1: *Left) PDF of 5 nm nanocrystal at 300 K obtained from the MD simulation. The inset figure shows the 5 nm nanocrystal within the MD box. Gold atoms are colored orange. The particle diameter is illustrated with a blue line inside the simulation box. Right) 3 FCC unit cells of crystal gold structure are shown. In each unit cell, a red arrow is drawn to illustrate interatomic distance. These three interatomic distances correspond to red vertical dashed lines shown in the PDF figure.*



When the structure of a material is perfectly crystalline, where each atom sits at an exact lattice point, we observe sharp Bragg peaks in its corresponding powder X-ray diffraction pattern. In this case, an underlying atomic structure can be revealed with

Figure 5.2: *First 3 PDF peaks of 5 nm nanocrystal at 100 K, 200 K, and 300 K temperatures obtained from the MD simulations. Note that peaks get broader with increasing temperature, indicating increased thermal disorder.*



Rietveld analysis, which uses Bragg peaks to refine a unit cell model. However, structural disorders give rise to diffuse intensity under the Bragg peaks. The diffuse intensity, which contains information about the local structure, is typically discarded as a background intensity in Rietveld analysis. Therefore, the Rietveld analysis can obtain only structural parameters that correspond to long-range ordered or crystalline portions of a material. In contrast, the PDF contains both average and local structural information since both intensities are used during Fourier transformation. Thus, the PDF analysis can be used as a complementary tool to the traditional Rietveld analysis of powder diffraction patterns.

Even though PDF contains local structural information, extracting this information successfully depends on PDF refinement methodology. In general, there are two kinds of PDF refinement methods: small-box and big-box modeling. A small number of crystallographic parameters with a periodic structure model is used in the small-box

modelling programs such as PDFGUI, TOPAS, and Diffpy-cmi. On the other hand, big-box modelling uses a large box of atoms in a periodic box, which is larger than the r-distance desired. Big box modelling programs move large numbers of atoms to minimize the difference between the calculated and measured PDF. They implement the reverse Monte Carlo (RMC) method. The programs include RMCProfile, DISCUS, and Full-RMC [48, 49]. Although the RMC method is mostly applied to periodic structures, there are a few studies using the RMC method for non-periodic spherical nanoparticle models with diameters lesser than 5 nm [50, 51] in RMC_POT software [52]. A more sophisticated modelling strategy for disordered systems is a differential evolutionary algorithm, which is implemented in DIFFEV. Using the DISCUS and DIFFEV together, fully atomistic modelling of discrete nanoparticles with non-periodic structure and its refinement against measured PDF function is possible. The discrete nanoparticle modelling can handle surface relaxation and ligand capping of nanoparticles accurately using the Debye scattering equation. However, computational complexity increases with the square of the number of atoms, avoiding modelling of larger nanoparticles. Therefore, the discrete particle modelling method is mostly used for nanoparticles smaller than 5 nm. For larger particles, single unit cell (small-box) modelling is preferred. One study performed both small-box and discrete nanoparticle modelling for PDF refinement of 3.6 nm diameter ligand-capped gold nanoparticle. The refinements with single and two phases using PDFGui (small-box), and with whole particle (ligand+particle) using DIFFEV (discrete modeling) were performed. Results showed that fully atomistic modelling provided better agreement for Au-S interactions at low-r region. The latter refinement took 17 h for each cycle in total of 221 cycles using 31 CPUs in parallel, indicating a high computational demand even for such small particle [53]. Computational demand of big-box and discrete nanoparticle modeling for particle sizes over 15 nm is high [54], hence, quick small-box modeling is preferred for larger nanocrystals. In this study, we used small-box modelling

to extract lattice parameter, MSD, and particle size of the realistic nanocrystals at different temperatures.

5.2 Obtaining the PDF of the Realistic Nanocrystals by Debye Scattering Equation

5.2.1 Generating X-ray Diffraction Data from Atom Coordinates of the Realistic Nanocrystals

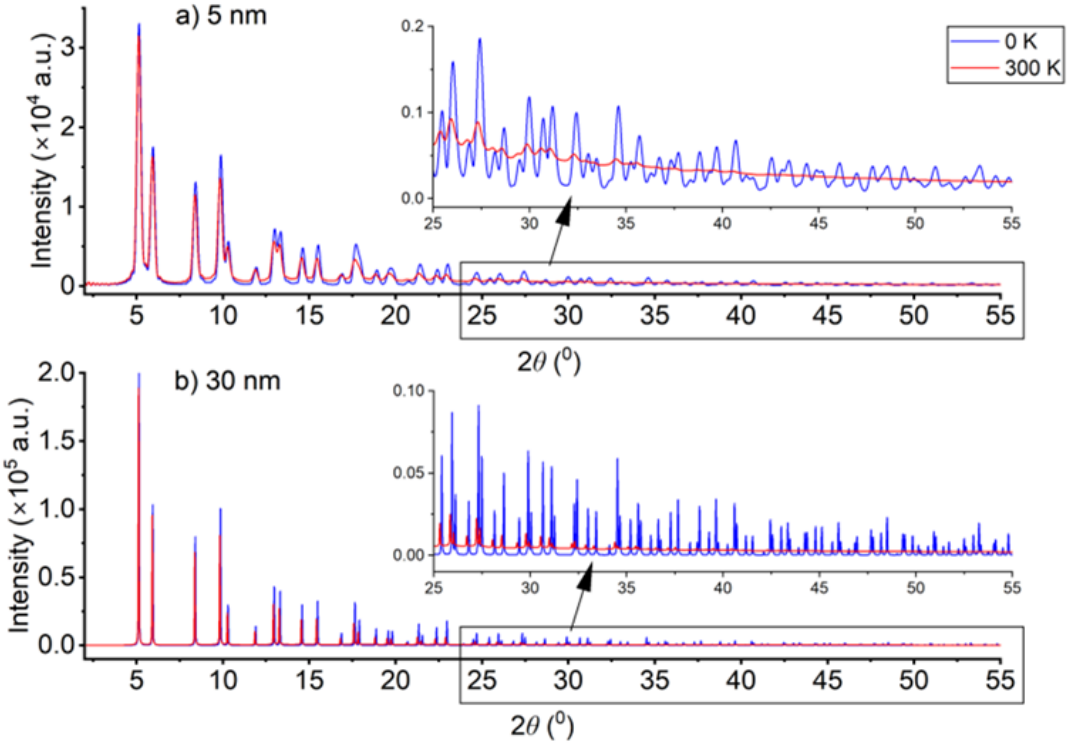
To compute analytical diffraction data, we implemented the Debyer algorithm [25], which evaluates the Debye scattering equation [55] in an optimized way for particles with large number of atoms. 5000 snapshots of atomic coordinates and the element type were fed into the algorithm to simulate the time-averaged diffracted intensities for each nanocrystal model [56]. Without loss of generality, the wavelength of X-rays was set as 0.21 Å, the scattering angle interval as [0.1°, 55°] with an angular spacing of 0.001°and $|\vec{q}| = \frac{4\pi \sin\theta}{\lambda}$ was evaluated. These experimental parameters were selected to optimize the computation time for diffraction simulations[1] and to determine the performance limits in typical experiments performed in synchrotron settings [57] while keeping the momentum transfer vector accessible with our experimental parameters comparable with past publications [58, 59, 60, 61]. Figure 5.3 shows the calculated diffraction data at 0 and 300 K for 5 nm and 30 nm gold nanocrystals.

5.2.2 Generating PDF Data from X-ray Diffraction Data

The first step of PDF analysis was converting the diffraction intensities to reduced PDFs (G_{XRD}). This was achieved by the Fourier Sine transform algorithm implemented in PDFgetX3 [62]. Before Fourier transforming, small angle scattering portions of the

[1]For each nanocrystal model at a particular temperature, 5000 separate Debye function calculation is performed with each snapshot coordinate.

Figure 5.3: *Simulated powder diffraction data for finite-sized a) 5 nm and b) 30 nm diameter gold nanocrystals at 0 and 300 K. The insets show the intensities over the range of 25°< 2θ < 50° and the assumed wavelength of X-rays is 0.21 Å. Note that the Bragg peaks at higher scattering angles disappear at 300 K due to the Debye-Waller factor.*



intensities were eliminated so that $|q_{min}|$=1.56 Å^{-1} for all datasets. The highest value of the momentum transfer vector was $|q_{max}|$=27.55 Å^{-1}. The observed PDF can be expressed as:

$$G_{XRD}(r) = \frac{2}{\pi}\int_{q_{\min}}^{q_{\max}} q[S(q)-1]\sin(qr)dq \tag{5.1}$$

where $S(q)$ is the reduced total scattering function and can be written as:

$$S(q) - 1 = \frac{I_{coh}(q)}{N\langle f\rangle^2} - \frac{\langle f^2\rangle}{\langle f\rangle^2} \tag{5.2}$$

where N is number of atoms, $q = |\vec{q}| = \frac{4\pi\sin\theta}{\lambda}$ and $\langle f\rangle^2$ is the squared average atomic scattering factor. $I_{coh}(q)$ is the total coherent intensity obtained with the Debyer software.

5.3 Small-Box PDF Refinement Algorithm

5.3.1 The G(r) Function

The reduced PDF or G(r) function for bulk model can be expressed as:

$$G(r) = 4\pi r \left[\rho(r) - \rho_0\right] \tag{5.3}$$

where ρ_0 is the atomic number density, and $\rho\,(r)$ is the atom-pair density function given as:

$$\rho(r) = \frac{1}{4\pi r^2 N} \sum_{\vartheta} \sum_{\mu} \delta\left(r - r_{\vartheta\mu}\right) \tag{5.4}$$

where *N* is number of atoms, δ is Dirac delta function, ϑ and μ refer to individual atoms, and $r_{\vartheta\mu}$ is interatomic distance between atoms ϑ and μ. In the small-box PDF refinement algorithm, a supercell of unit cell is created so that the desired r-range is achieved. Next, (5.3) is multiplied with nanocrystal shape factor to include both shape and finite size effects on the bulk PDF model. The final form of the Gr relation for nanocrystal model can be written as:

$$G_{nano}(r) = 4\pi r \left[\rho(r) - \rho_0\right] f(r) \tag{5.5}$$

where $f(r)$ is the shape factor for spherical nanocrystals [32] and given as:

$$f(r) = 1 - \frac{3}{2}\frac{r}{D} + \frac{1}{2}\left(\frac{r}{D}\right)^3 \tag{5.6}$$

where *r* is interatomic distance, and *D* is the particle diameter. Note that the second term in (5.5) is the PDF baseline for nanocrystal model. Convolution of (5.5) with the Fourier transform of the termination function (or window function) due to q_{max}, equals to experimentally accessible PDF G_{XRD} in (5.1) [63]. Lastly, we evaluated the first component of (5.3) from the nanocrystal model. In this case, the shape factor is unnecessary since the model is a nanocrystal. We call the new function $G_{forward}$ in this study, which can be

expressed as:

$$G_{\text{forward}}(r) = 4\pi r\rho(r) = \frac{1}{rN}\sum_{m}^{N}\sum_{n}^{N}\delta\left(r - r_{mn}\right) \tag{5.7}$$

5.3.2 Atomic Disorder

Sample-related [63, 64] and instrument-related [65] factors cause finite broadening in all PDF peaks. The former originates from lattice strains (static) and thermal displacements [64] (dynamic) of atoms from ideal lattice positions. While thermal displacements emerge from atomic vibrations at finite temperatures, lattice strains originating from surface reconstruction are present in nanocrystals even at 0 K [3]. Unfortunately, analytical models incorporating the effect of static displacements due to surface reconstruction of nanocrystals on PDF peak widths do not exist [16]. But peak broadening due to thermal displacements is modelled by the following strategy: If relative displacements of atoms are entirely uncorrelated, all PDF peaks broaden by an equal amount of $\sqrt{2MSD}$, where MSD is the mean square atom displacements [64]. In crystalline solids, nearby neighbour atom movement is not random due to strong interatomic forces; thus, correlations are considered [64] by a peak sharpening factor, δ, which is most significant for the closest atoms. In crystalline solids, therefore, a variation in the peak breadth at different radial distances is expected.

DiffpyCMI employs two forms of δ (correlation/sharpening parameter): for the PDF peak centered at an interatomic distance r_{ij}, δ scales with $1/{r_{ij}}^2$ at temperatures lower than the Debye temperature $(\theta_D)$of the crystal and with $1/r_{ij}$ at temperatures higher than that [64]:

$$\begin{aligned}\sigma\left(r_{ij}\right) &= \sqrt{1 - \frac{\delta_1}{r_{ij}}} * \sigma_0 \quad (T \geq \theta_D) \\ \sigma\left(r_{ij}\right) &= \sqrt{1 - \frac{\delta_2}{{r_{ij}}^2}} * \sigma_0 \left(T \leq \theta_D\right)\end{aligned} \tag{5.8}$$

In (5.8), $\sigma(r_{ij})$ is the width of the PDF peak and σ_0 is the peak-width corresponding

to the uncorrelated limit or $\sigma_0 = \sqrt{2MSD}$. For atomic pairs with a large separation distance, the corresponding PDF peak is assigned a peak breadth value of σ_0. Once a peak-width model is selected, the profile function is generated using the Gaussian function in DiffpyCMI.

5.3.3 Including Finite Q_{max} Effect with Window Function

The PDF containing termination effect (or termination ripples), that is, the effect of Q_{max} included in PDF, can be obtained by convolution of ideal PDF with the Fourier transform of the window function. The ideal PDF is the PDF calculated from the model structure; hence, the ideal PDF contains no effect of Q_{max}. The convoluted PDF is defined as (A3.3.12 in [63]):

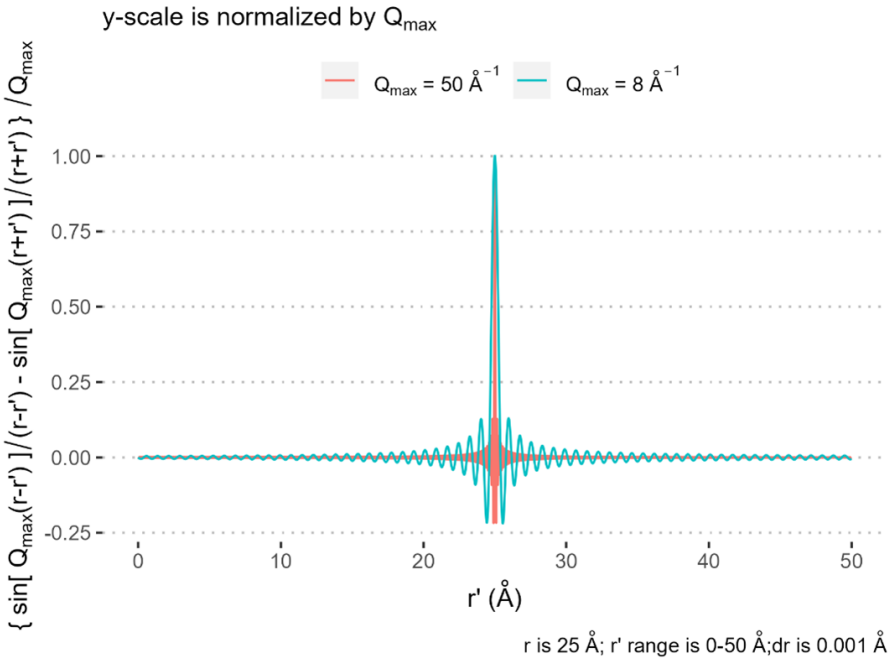
$$G'(r) = \frac{1}{\pi}\int_0^\infty G\left(r'\right)\left[\frac{\sin Q_{\max}\left(r-r'\right)}{r-r'} - \frac{\sin Q_{\max}\left(r+r'\right)}{r+r'}\right]dr' \tag{5.9}$$

where $G'\left(r\right)$ and $G(r\prime)$ are convoluted and ideal PDFs, respectively. The second component of the right-hand side of the equation is the the Fourier transform of the window function, and it causes termination ripples in PDF due to finite Q_{max}.

In Figure 5.4, normalized Fourier transform of the window function, as a function of *r* is shown for $Q_{max} = 8\,\text{Å}^{-1}$ and $Q_{max} = 50\,\text{Å}^{-1}$. The Fourier transform of the window function, has many peaks (central peak and neighbor peaks). The neighbor peaks decay with increasing distance from the central peak. Furthermore, as Q_{max} increases, the central peak becomes narrower, and other neighbor peaks decay relatively faster. In the limiting case (infinite Q_{max}), the central peak becomes δ-function. In addition, wavelength of ripples in PDF is $\approx 2\pi/Q_{max}$ (Page 60 in [63]). Note that this wavelength is not the wavelength of peaks in the Fourier transform of the window function but in convoluted PDF.

The (5.9) was evaluated numerically for some series of Gaussian functions generated artificially (not coming from real atomic model) to represent PDF. Two scenarios

Figure 5.4: *Normalized (by Q_{max}) Fourier transform of the window function, at two different Q_{max}: $8\,\text{Å}^{-1}$ (blue line) and $50\,\text{Å}^{-1}$ (red line).*



were tested. The first scenario aims to show the effect of Q_{max} for fixed peak width (or MSD), the other scenario demonstrates the effect of peak width for fixed Q_{max}. First scenario: Figure 5.5 illustrates the effect of finite Q_{max} on convoluted PDF. From the figure, one can notice that the ripples are negligible when Q_{max} is relatively large, that is, the ideal and convoluted PDFs are almost same (compare Figure 5.5 (top) and Figure 5.5 (bottom)). In contrast, the ripples are evident when Q_{max} is relatively small. Therefore, the convoluted PDF contains fake peaks (or ripples) in addition to real peaks of ideal PDF (compare Figure 5.5 (top) and Figure 5.5 (middle)). Furthermore, relatively small Q_{max} modifies real peaks (by making them broader) as well, in addition to causing ripples in between real peaks. Second scenario: Figure 5.6. illustrates the effect of MSD on the convoluted PDF for a fixed Q_{max}. First, the ideal PDFs at 10 K (Figure 5.6 (Top left)) and 300 K (Figure 5.6 (Bottom left)) were generated. Then, ideal PDFs were convoluted with the Fourier transform of the window function to account for finite Q_{max} ($26\,\text{Å}^{-1}$) at 10 K

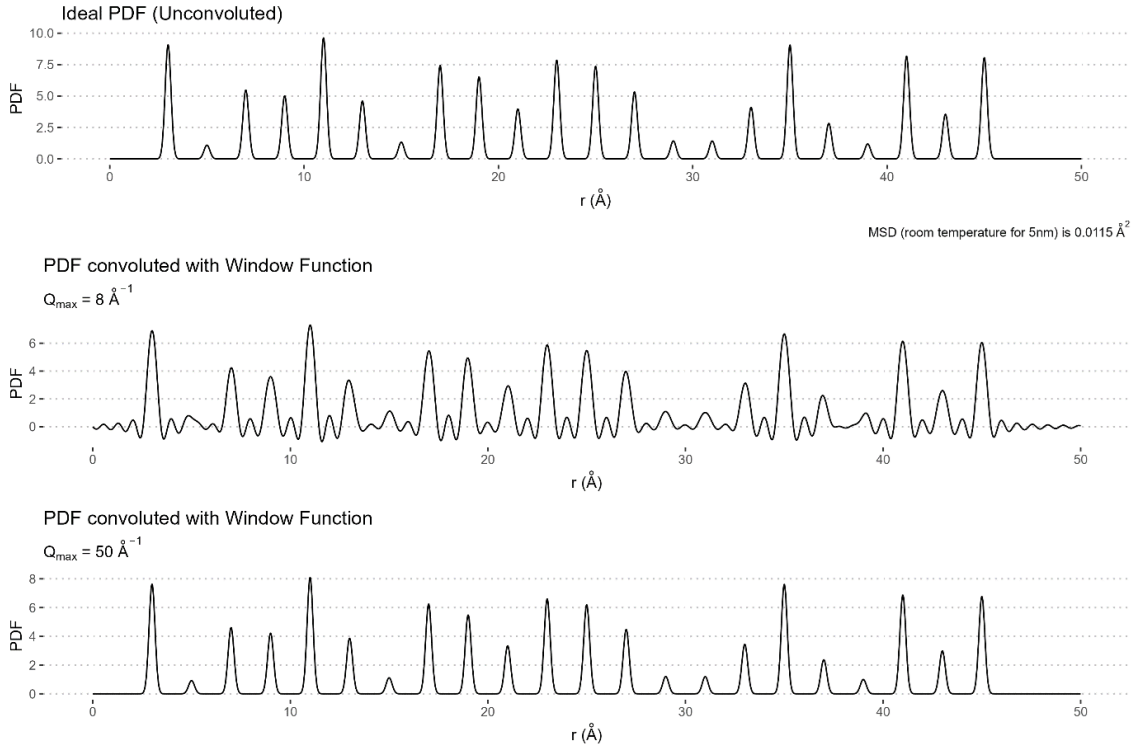
and 300 K temperatures. The convoluted PDF at 10 K (Figure 5.6 (Top right)) contains termination ripples and modified real peaks. In contrast, the convoluted PDF at 300 K (Figure 5.6 (Bottom right)) has no obvious sign of ripples, hence, is almost same with the corresponding ideal PDF.

We illustrated that finite Q_{max} causes termination ripples in PDF (Figure 5.5). We also showed that termination ripples are negligible when MSD is relatively larger (broader PDF peak width) (Figure 5.6). Then, there must be a relation between Q_{max} and MSD such that this relation determines whether termination ripples caused by finite Q_{max} are negligible or not. The effect of termination ripples on PDF is negligible when Q_{max} is approximately equal to $3/\ll u^2 \gg^{1/2}$ (Page 86 in [63]). The denominator of this relation is equal to the square root of MSD. Indeed, we observed negligible termination ripples in Figure 5.6 (Bottom right), for which, Q_{max} ($26\,\text{Å}^{-1}$) and $3/\ll u^2 \gg^{1/2}$ ($28\,\text{Å}^{-1}$) are more or less close to each other. On the other hand, termination ripples are significant in Figure 5.6 (Top right), for which, Q_{max} ($26\,\text{Å}^{-1}$) is much smaller than $3/\ll u^2 \gg^{1/2}$ ($158\,\text{Å}^{-1}$).

5.4 PDF Refinement Methodology

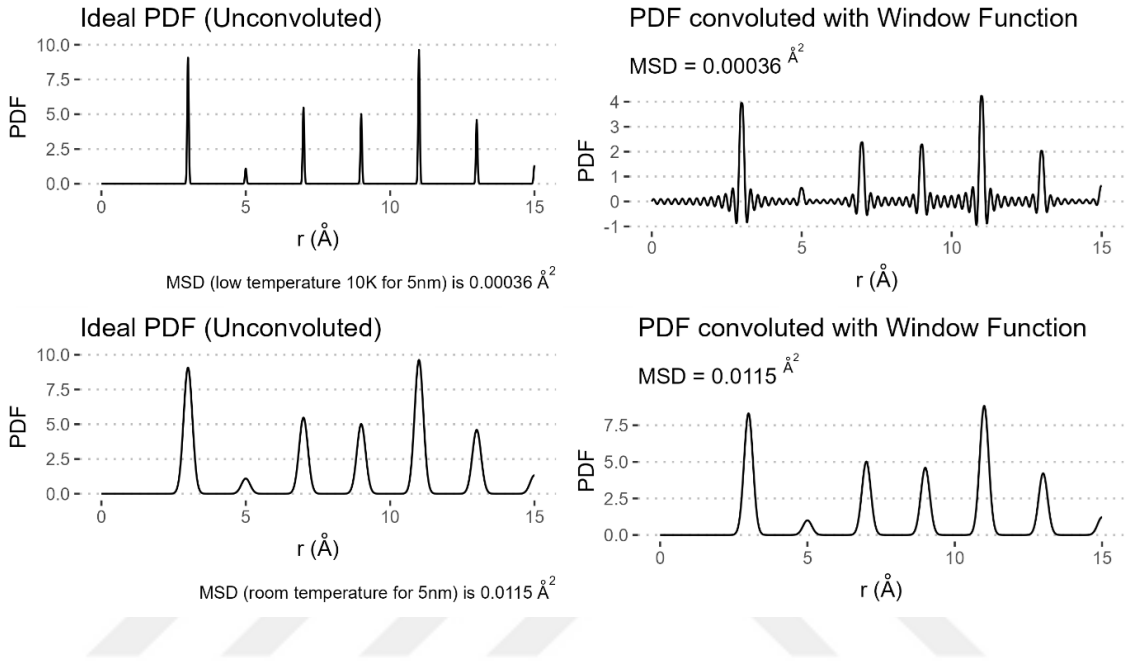
After Fourier transformation, the resulting atomic pair distribution functions were refined by DiffpyCMI [66]. For all analyzed diffraction datasets, q_{damp} and q_{broad} were fixed at 0 since the data were computed analytically and did not include any instrument-related broadening or damping effects, and five parameters were refined over the real space interval from 1.5 Å to 10 Å in excess of the true nanocrystal diameter: 1) an arbitrary scale factor, 2) particle size, which corresponds to the average size of the diffracting particles assuming they are spherical in shape [67], 3) lattice parameter that sets the positions of the atomic pair distances present in the particle volume, 4) atomic displacement parameter to account for the broadening of the PDF peaks due to combined dynamic and

Figure 5.5: *Top) Ideal or unconvoluted PDF, Middle) convoluted PDF with the Fourier transform of the window function of Q_{max}: $8\,\text{Å}^{-1}$, and Bottom) Q_{max}: $50\,\text{Å}^{-1}$. The ideal PDF was generated artificially at given r positions with constant peak width being equal to $\sqrt{2MSD}$ where MSD is room temperature (300 K) MSD of 5 nm finite-sized particle (see the caption of top figure for exact MSD). Peak heights are randomly scaled to imitate real PDF. Note that, MSD is fixed, only Q_{max} changes between middle and bottom PDF.*



static displacements [68], 5) correlated displacement parameter (δ_1 or δ_2) which tunes the sharpness of the PDF peaks and acts as a measure of the correlation between the relative displacement of atomic pairs at different bond lengths. The refinements were performed in multiple steps in the following order: 1) refine lattice parameter and scale factor while keeping the remaining parameters fixed, 2) add atomic displacement parameter and refine all three, 3) add particle size and refine all four, 4) fix all previous parameters, free delta and refine it alone, 5) free all previous four parameters and refine all five together. At the end of each refinement, we evaluated the success of the procedure by visually checking

Figure 5.6: *Effect of peak width (or MSD) on convoluted PDF for a fixed Q_{max}. Only r up to 15 Å is shown for clarity. Similarly, PDF data is artificially generated as in Figure 5.5. Top left) Ideal PDF at 10 K, and Top right) Convoluted PDF with Q_{max}: 26 $\mathrm{\AA}^{-1}$. Bottom left) Ideal PDF at 300 K, and Bottom right) Convoluted PDF with Q_{max}: 26 $\mathrm{\AA}^{-1}$. Note that, Q_{max} is fixed, only MSD changes between top and bottom PDFs.*



the agreement between the refined model and the atomic PDF computed from the diffraction data and by monitoring the residuals. A typical value of weighted residual in our refinements was around 0.07.

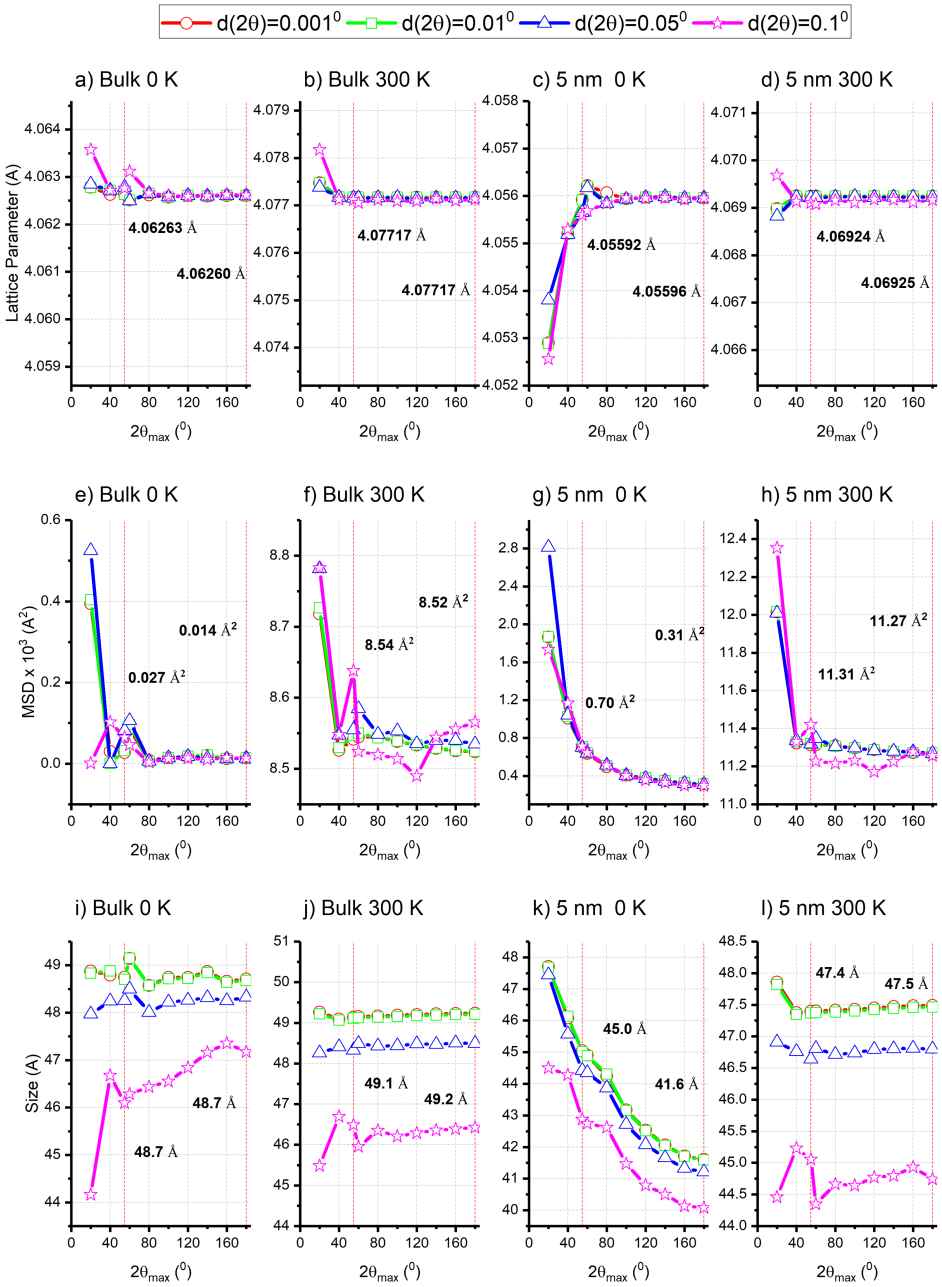
We note that proper selection of the initial values for the parameters to be refined was critical for the success and reliability of the PDF refinement. Among the five parameters studied here, we found the initial value of the lattice parameter to be the most critical. Since lattice parameter was strongly temperature dependent, we observed failure of PDF refinements of lowest temperature diffraction data when the initial value of the lattice parameter was set to that of the CIF file for gold, i.e., 4.078 Å at room temperature. Hence for the refinement of all datasets, the initial values of the lattice parameters were set to those computed by MD simulations of bulk gold crystals at the corresponding

temperatures. In this step, the particle size dependence of lattice parameters was not as significant as their temperature dependence, hence at a particular temperature, we used the same initial value for lattice parameters for all nanocrystal sizes. The initial values of the remaining refinement parameters were 1) scale factor = 1.0, 2) particle size = same as the nominal sizes of the nanocrystals used to simulate the diffraction data, 3) atomic displacement parameter = isotropic displacement values published in past literature [21].

5.5 Finite Q_{max} Effect on Extracted Structural Parameters from the PDF Refinement

We checked whether the parameters selected to simulate the diffraction data, i.e. ($2\theta_{\max}$, $d2\theta$), had an effect on the refinement results. This is shown in Figure 5.7 where the refined lattice parameters (5.7(a-d)), MSDs (5.7(e-h)) and crystal sizes (5.7(i-l)) are reported from a single snapshot of diffraction data evaluated with different angular spacing values ($d2\theta$) and refined over different angular ranges: refined lattice parameters only differed in the fifth decimal between our angular range (i.e. $2\theta_{\max} = 55^\circ$ indicated as the left red dashed line) and the full angular range (i.e. $2\theta_{\max} = 180^\circ$ and $d2\theta = 0.001^\circ$ indicated as the right dashed line) whereas the MSDs depended on the angular range more strongly, especially for the diffraction data evaluated at 0 K. However, at finite temperature, the angular range of the diffraction data had a much weaker effect. Lastly, the refined crystal sizes were more sensitive to the angular spacing ($d2\theta$) than the angular range and the largest refined sizes were obtained with the smallest $d2\theta$ which was indeed what we selected in our diffraction simulations.

Figure 5.7: *Variation in refined lattice parameters (a-d), MSD (e-h) and crystallite size (i-l) from PDF analysis with respect to the angular range and step size of the diffraction data from a single snapshot of atomic coordinates. Each subfigure depicts the variations for 5 nm truncated-bulk or finite-sized nanocrystal model at 0 or 300 K indicated in the title. Values on each window report the refined parameter values corresponding to the step size and angular range selected in this study (left) and for* $2\theta_{\max} = 180°$.

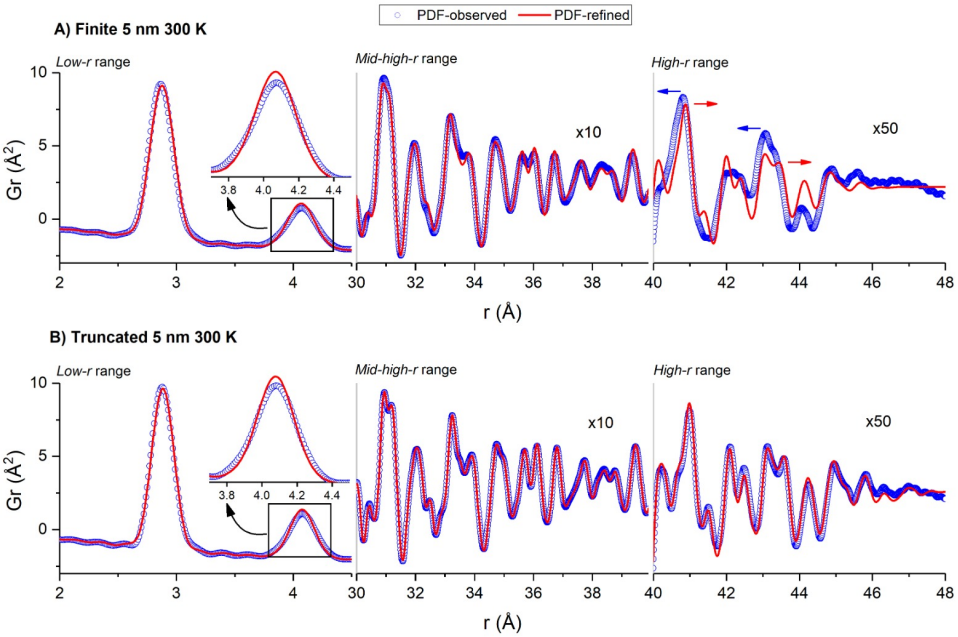


5.6 Effect of Nanocrystal Surface on the Quality of PDF Refinement

We start by comparing the quality of PDF refinement on the diffraction data from truncated-bulk and finite-sized nanocrystals. Figure 5.8 shows the PDF refinement results for finite-sized 5 nm nanocrystal and its truncated-bulk counterpart at 300 K. Here "PDF-refined" is the PDF computed from the unit cell model by DiffpyCMI and "PDF-observed" is the PDF obtained by Fourier transforming the diffraction data. We group the PDF peaks based on the interatomic distances indicated as "Low-r range", "Mid-high-r range", and "High-r range". ("PDF-refined" agrees almost perfectly with "PDF-observed" over the "Mid-r range" as shown in Figure 5.9.) Only the first two peaks in the "Low-r range" are shown since the remaining peaks share common characteristics. Due to the decreasing heights of nanocrystalline PDF peaks with increasing interatomic distance [67], peaks in the "Mid-high-r range" and "High-r range" are enhanced by approximately 10 and 50 times relative to the peak heights shown in "Low-r range".

In the "Low-r range" of the PDFs of truncated-bulk crystal, peaks are sharp due to the strong correlation between displacements of neighbouring atoms [59, 69]. However, "PDF-observed" deviates from "PDF-refined" as the figure inset shows. This deviation results from the inadequacy of the correlated displacement parameter in modelling the sharpening of PDF peaks, since the observed PDFs from diffraction data including uncorrelated atomic displacements or those without thermal diffuse scattering agreed with the refined PDFs [56] (see Figure 5.10). Similar deviation is observed between "PDF-observed" and "PDF-refined" from the finite-sized nanocrystal. Moreover, PDF peaks become broader, indicating larger atomic displacement in finite-sized nanocrystals than the truncated-bulk model [70, 71].

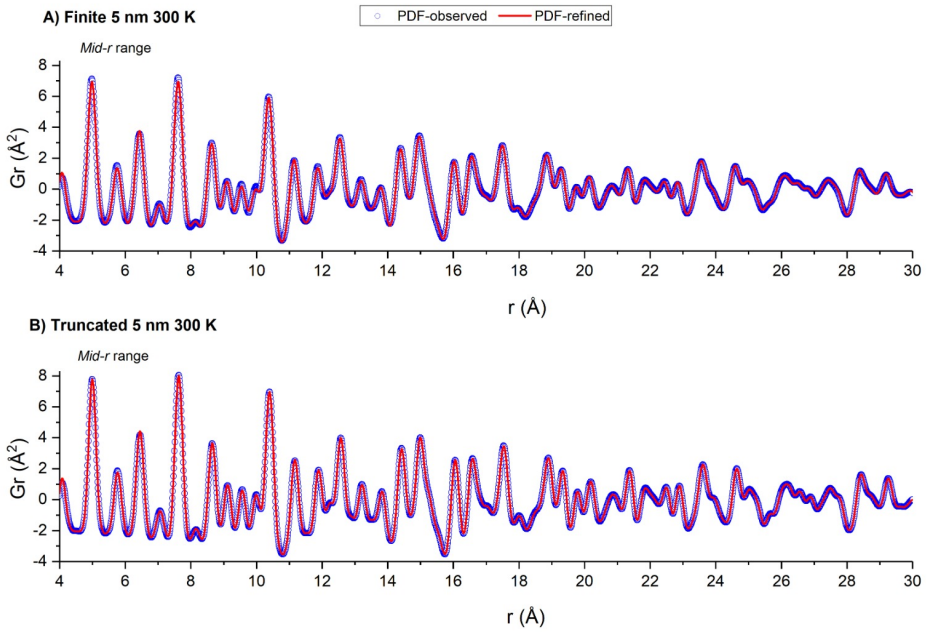
Figure 5.8: *PDF refinement of diffraction data simulated from 5 nm truncated-bulk and finite-sized spherical gold nanocrystals at 300 K. Blue markers indicate the PDF data evaluated from Fourier transforming the diffraction data while the red plots indicate the fitted PDFs by DiffpyCMI. Peak widths were refined by* δ_1.



In the "Mid-range", shown in Figure 5.9, correlated displacement effects disappear, and atoms vibrate independently, resulting in a perfect match between "PDF-observed" and "PDF-refined" for both finite-sized and truncated-bulk crystals. This indicates that the dominant disorder in this region is the uncorrelated dynamic disorder properly captured by the broadened Gaussian models representing the PDF peaks. PDF peaks in this region are not well-separated unlike peaks in the "Low-r range" and many neighbouring and broadened PDF peaks exist. The deviation between "PDF-refined" and "PDF-observed" increases over the "Mid-high-r range" for the finite-sized particle where both static and dynamic displacement effects gradually increase [56]. This is expected since PDF peaks in this r range are dominated by bond distances from core & surface regions rather than core & core region.

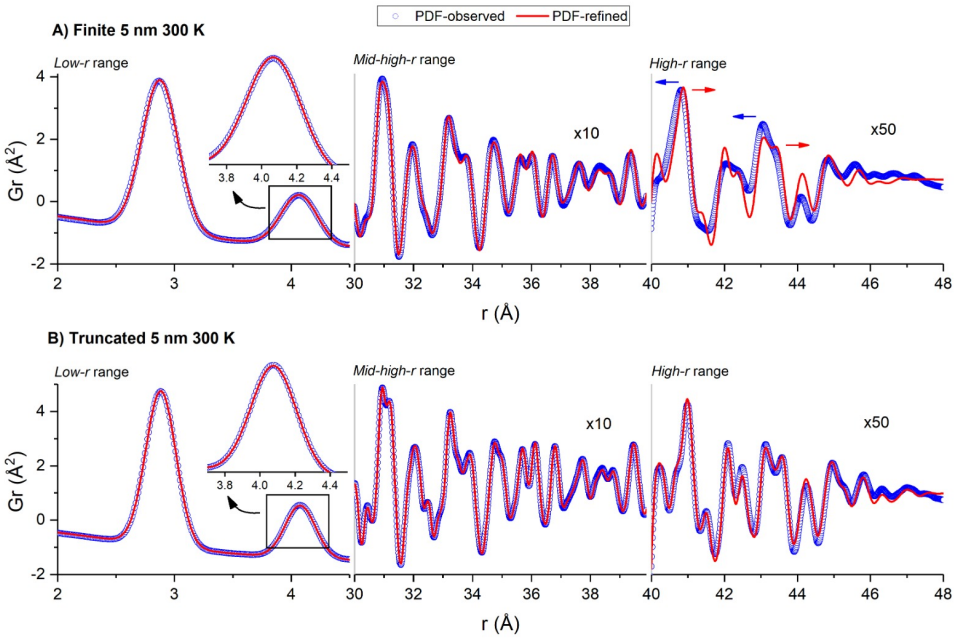
In the "High-r range" of truncated-bulk crystal, peak widths and the agreement

Figure 5.9: *PDF refinement of diffraction data simulated from 5 nm truncated-bulk and finite-sized spherical gold nanocrystals at 300 K over the mid-r range (4 Å < r < 30 Å). Blue markers indicate the PDF data evaluated from Fourier transforming the diffraction data while the red markers indicate the fitted PDFs by DiffpyCMI. Peak widths were refined by* δ_1.



between "PDF-observed" and "PDF-refined" are similar to those of the "Mid-r range" except peak heights are lower due to limited particle size. No PDF peak exists beyond 48 Å which corresponds to the maximum interatomic distance. In the finite-sized nanocrystal, agreement between "PDF-observed" and "PDF-refined" is worse because PDF peaks in this range are dominated by surface & surface bond distances and both static [56] and dynamic [18] displacements are maximized in surface atoms. Since "PDF-refined" can be interpreted as the PDF of the long-range (average) structure of the particle [72], while "PDF-observed" as the signature of local (short-range) structural deviations from the long-range order, the following can be extracted by comparing "PDF-refined" with "PDF-observed" over this r region: 1) Overall, peak positions of "PDF-refined" are greater than

Figure 5.10: *PDF refinement of diffraction data simulated from 5 nm truncated-bulk and finite-sized spherical gold nanocrystals at 300 K. Blue markers indicate the PDF data evaluated from Fourier transforming the diffraction data after thermal diffuse scattering intensity is subtracted while the red plots indicate the fitted PDFs by DiffpyCMI. Peak widths were refined by* δ_1.



that of "PDF-observed" pointing to contracted local surface & surface bond distances relative to long-range bond distances. It indicates that static displacements of surface atoms cause a left shift in the PDF peak positions, 2) Static atomic displacements are heterogeneously distributed within the surface layer, causing a variable amount of shift for each observed PDF peak relative to the refined PDF peak. Thus, lattice parameters computed from these PDF peaks must fluctuate, 3) "PDF-observed" is broader than "PDF-refined" indicating that the total MSD of surface atoms is larger than that of the long-range structure, 4) Structural coherency in this region is weakened, therefore "PDF-refined" decays earlier than "PDF-observed".

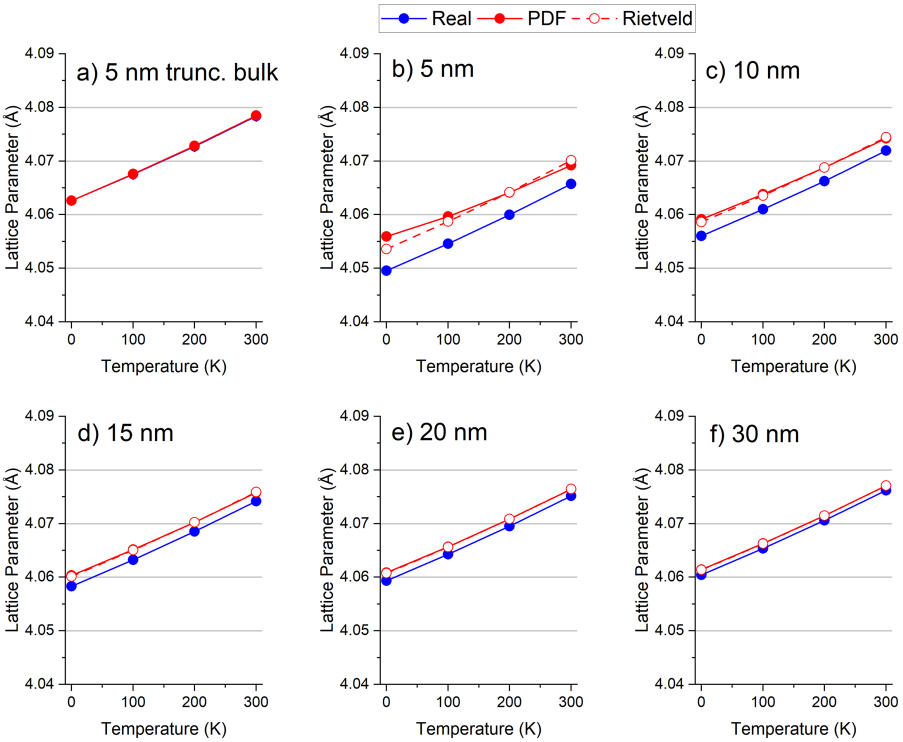
5.7 Comparison of the Real Space and Extracted Structural Parameters from the PDF Refinement

5.7.1 Lattice Parameter

Figure 5.11 presents the lattice parameters obtained from real space calculations based on static atom coordinates ("Real") and PDF refinement of diffraction data ("PDF-refined") from truncated-bulk (5.11(a)) and finite-sized gold nanocrystals (5.11(b-f)) at 0 K, 100 K, 200 K, and 300 K. PDF refinement at all temperatures was performed on the diffraction data computed from the snapshot atom coordinates, except that at 0 K the diffraction data was computed from static coordinates. Furthermore, atomic displacement correlations were modeled with a peak-width parameter δ_1. Figure 5.11(a) shows that for the truncated-bulk crystal model, both real space calculations and PDF refinements of lattice parameters increase linearly with increasing temperature indicative of linear thermal expansion. Irrespective of the selected peak-width model (nodelta, δ_1 or δ_2), the agreement between PDF refinement and real space calculation is almost perfect; with maximum deviation ($\frac{a_{PDF}-a_{Real}}{a_{Real}} \times 100\%$) from real space being 0.00377 % observed from the PDF refinement with no peak-width modeling (nodelta) at 300 K. Compared to our past work which reported around 0.025 % deviation from the true (average) lattice parameter at 0 K [2], the accuracy of PDF refinement is higher than Rietveld refinement for truncated-bulk nanocrystals. In addition, this deviation $\Delta \mathrm{a} = 1.54 \times 10^{-4}$Å is comparable to the precision of standard diffractometers $\Delta \mathrm{a} \approx 10^{-4}$Å [2] and further decreases to $\Delta \mathrm{a} = 4.89 \times 10^{-5}$Å for 10 nm gold nanocrystals.

For finite-sized nanocrystals seen in Figure 5.11(b-f), due to the surface reconstruction, the lattice parameter of unit cells in the surface layer is smaller than the core region [56, 3] which is also evident from Figure 5.8. Hence, the average lattice parameter increases with increasing particle size at a given temperature consistent with previous

Figure 5.11: *Average lattice parameters with respect to temperature calculated from atomic coordinates (Real) and extracted by PDF (PDF) and Rietveld refinement (Rietveld) of the corresponding diffraction data are shown for a) 5 nm truncated-bulk crystal and b-f) 5-30 nm finite-sized nanocrystals. The peak-width parameter selected during PDF refinement is* δ_1.



experimental work [70] at 300 K, the average real space computed lattice parameters are 4.06570 Å, 4.07193 Å, 4.07417 Å, 4.07516 Å, and 4.07623 Å for 5, 10, 15, 20, and 30 nm nanocrystals, respectively. This confirms that the effect of contracted surface unit cells on the average lattice parameter is less significant in larger nanocrystals since the average lattice parameter approaches the limiting value of 4.0782 Å belonging to bulk crystalline gold [73]. Similar size-dependent trends are observed in PDF refined lattice parameters; although these are slightly higher than those from real space calculations and their deviation from real space calculations decreases with increasing particle size for all temperatures. Repeating these refinements with different peak-width parameters leads to

similar conclusions. It shows that lattice parameter is relatively insensitive to the selection of the correlated displacement parameter (see Table 5.1). However, among the three peak-width models (δ_1, δ_2, nodelta), the maximum deviation of PDF-refined lattice parameter is observed as 0.1579 % for the 5 nm finite-sized nanocrystal equilibrated at 0 K and refined with "nodelta" peak-width model. This is orders of magnitude larger deviation from real space calculations than the truncated-bulk crystal model. Moreover, compared to previous work where Rietveld refinement of 5 nm particle with surface relaxation showed 0.0909 % deviation from real space-computed lattice parameter [3], it means that PDF refinement is less successful in capturing average lattice parameters than Rietveld refinement when static displacements exist in the nanocrystal surface.

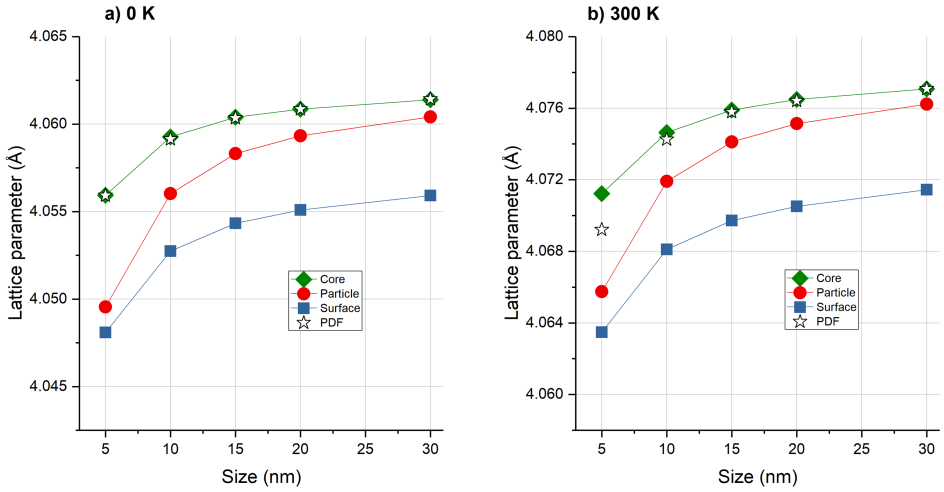
To correlate PDF-refined lattice parameters with local variations of the lattice parameter in the crystal, we present core-, surface- and particle-averaged lattice parameters from real space calculations separately against the PDF-refined lattice parameters at 0 and 300 K in Figure 5.12. For these calculations, we divided each nanocrystal into core and surface regions and computed corresponding average lattice parameters. The surface region included atoms that were located on the outermost shell volume of 10 Å thickness, and the core region contained the remaining atoms (The thickness of the surface shell was determined based on the fluctuation of the local lattice parameter shown in our earlier study [56]). Figure 5.12(a) shows that real space calculations of core lattice parameters are greater than their surface counterparts at 0 K. Particle-wide average lattice parameter is between those of the core and surface. Like particle-wide average values, lattice parameters of the core and surface regions depend on the size of the nanocrystal. Switching to the PDF refined lattice parameters at 0 K, we observe they agree with core lattice parameters rather than particle-wide average lattice parameters. It indicates that static displacement of atoms of the surface region, which is the only type of displacement

Table 5.1: *Lattice parameters of the investigated nanopowders computed by real space calculations and by PDF refinement of the diffraction data. The three different refinement results from PDF analysis belong to three different peak-width models employed in DiffpyCMI.*

Size (nm)	Temperature (K)	Real Space a (Å)	PDF a (Å)		
			δ_1	δ_2	Nodelta
5	0	4.0496	4.05592 (9)	4.05593 (8)	4.05595 (8)
	100	4.0546	4.0597 (2)	4.0597 (2)	4.0597 (2)
	200	4.0599	4.0641 (4)	4.0642 (4)	4.0642 (3)
	300	4.0657	4.0692 (5)	4.0692 (5)	4.0694 (5)
10	0	4.0560	4.05915 (4)	4.05915 (4)	4.05915 (4)
	100	4.0610	4.0638 (1)	4.0638 (1)	4.06379 (9)
	200	4.0663	4.0688 (2)	4.0688 (2)	4.0688 (2)
	300	4.0719	4.0743 (2)	4.0743 (2)	4.0743 (2)
15	0	4.0583	4.06035 (3)	4.06035 (3)	4.06035 (3)
	100	4.0633	4.06514 (6)	4.06514 (6)	4.06514 (6)
	200	4.0685	4.0703 (1)	4.0703 (1)	4.0703 (1)
	300	4.0742	4.07580 (14)	4.07580 (14)	4.07580 (14)
20	0	4.0593	4.06085 (3)	4.06085 (3)	4.06085 (2)
	100	4.0643	4.06569 (5)	4.06569 (5)	4.06569 (5)
	200	4.0695	4.07086 (8)	4.07086 (8)	4.07086 (8)
	300	4.0752	4.07641 (11)	4.07641 (11)	4.07641 (11)
30	0	4.0604	4.06143 (2)	4.06143 (2)	4.06143 (2)
	100	4.0653	4.06630 (4)	4.06630 (4)	4.06630 (4)
	200	4.0706	4.07150 (6)	4.07150 (6)	4.07150 (6)
	300	4.0762	4.07707 (8)	4.07707 (8)	4.07707 (8)
5 (Bulk)	0	4.0626	4.06263 (6)	4.06263 (6)	4.06263 (6)
	100	4.0675	4.06759 (14)	4.06759 (14)	4.06759 (14)
	200	4.0728	4.0729 (3)	4.0729 (3)	4.0729 (3)
	300	4.0784	4.0785 (4)	4.0785 (4)	4.0785 (4)

at 0 K, is almost invisible to PDF analysis. In contrast, the PDF lattice parameter approaches the particle-averaged lattice parameters from real space calculations at 300 K as shown in Figure 5.12(b). It means that static surface atom displacements which are more dominant for the smallest nanocrystals, must be somewhat captured by PDF refinement at finite temperature.

Figure 5.12: *Real space calculations of core, surface and particle-wide average lattice parameters of finite-sized gold nanocrystals with respect to crystal size at a) 0 K and b) 300 K.*



To identify the reason for this temperature-dependent behavior, we calculated the PDFs directly from atomic coordinates ($G_{forward}$) of the 5 nm particle at 300 K (by (5.7)) with and without temperature effect using snapshot and static coordinates. The forward calculations did not include instrumental errors (i.e., those due to q_{min}, q_{max}, Δq) and resulted in a series of isolated PDF peaks each corresponding to a particular interatomic distance. The first three forward-calculated PDF peaks are shown in Figure 5.13(a-b) for 5 nm snapshot and static finite-sized particle models, respectively. We extracted the PDF peak centers by fitting Gaussian functions (consistent with Diffpy-CMI algorithm) and converted them to lattice parameters. Figure 5.13(c) shows the

difference between these lattice parameters from static and snapshot coordinates, i.e. $(a_{PDF,\ Snapshot} - a_{PDF,\ Static})$, as a function of interatomic distance *r* along with the PDF-refined lattice parameters from analyzing the diffraction data by DiffpyCMI. From the figure we observe that $(a_{PDF,\ Snapshot} - a_{PDF,\ Static})$ is negative since $a_{PDF,\ Static}$ is greater than $a_{PDF,\ Snapshot}$ even though they are identical when computed directly from atomic coordinates. A similar result is obtained with PDF refinements (horizontal line) suggesting that different profiles of static and snapshot PDF peaks influence the positions of the fitted Gaussians from which lattice parameters are derived. To confirm this, we calculated the skewness parameter of all forward-calculated PDFs from static and snapshot coordinates. Figure 5.13(d) shows the distribution of the skewness parameters: The average skewness is -1.12 and -0.095 for static and snapshot PDF, respectively, indicating that deviation from Gaussian shape is higher in static PDFs. This means that static displacements of surface atoms increase the absolute skewness of PDF peaks, lower the quality of Gaussian-fitting and thus affect their positions. It also explains why the PDF-refined lattice parameter agrees with the core lattice parameter and deviates from particle-averaged lattice parameters the most at 0 K, i.e. $(a_{PDF} - a_{Real,particle})/a_{Real,particle} = 0.1579\%$. At finite temperature, dynamic atom displacements increase and become comparable with/surpass static displacements, PDF peak profiles become more Gaussian (as seen at 300 K) and therefore PDF refinement results in better agreement with particle-averaged lattice parameter (which encodes information from the surface layer), i.e. $(a_{PDF} - a_{Real,particle})/a_{Real,particle} = 0.086\%$. Figure 5.14 depicts the relative variation of static and dynamic atom displacements from particle core to particle surface at 0 and 300 K for a 10 nm gold nanocrystal (These were computed by (3.3) and (3.4) over a series of concentric spherical shells with 0.125 Å thickness). As seen, only static displacements are present at 0 K, which are independent of temperature [56] and low around the particle

center. Around the particle surface, however, they become significant. Dynamic displacements are present only at finite temperatures and these are dependent on both temperature and the radial distance from the particle center. Hence at 300 K, the core atom displacement is almost composed solely of dynamic component whereas the surface atom displacements have almost equal contribution from both static and dynamic components. This difference in both the spatial and thermal variation of static and dynamic displacement explains why PDF refinement performs differently at different temperatures.

5.7.2 Particle Size

PDF peaks of finite-sized nanocrystals decay with increasing interatomic distance and approach background values beyond distances larger than the crystallite size. Hence, DiffpyCMI implements a shape-dependent size correction factor during refinement of crystal size assuming nanocrystals as attenuated bulk crystals [74]. In our case, the finite size correction factor for the spherical shapes was used [67]. All PDF refinements were performed with three peak-width models: δ_1, δ_2 and "nodelta". Static coordinates were used for real space calculations of crystal size, and mean and maximum diameters were selected for comparison with PDF-refined crystallite sizes from the corresponding diffraction data (see Table 5.2).

In Figure 5.15, "Real-mean" and "Real-max" indicate the mean and maximum values of the diameter distributions from real space calculations. For all crystal models studied, "Real-max" is approximately 2.5 Å larger than "Real-mean" at all temperatures. Comparing real space calculations with PDF analysis for the 5 nm truncated-bulk crystal in Figure 5.15(a), we see that PDF-refined sizes are almost the same as "Real-max" at all temperatures and are larger than "Real-mean". This means that PDF refinement captures the maximum crystallite diameter accurately regardless of temperature when the

Figure 5.13: *a) First three peaks of $G_{forward,Snapshot}$ from 5 nm finite-sized gold nanocrystal. 5000 snapshot coordinates were used to compute the PDF peaks. The fitted Gaussian function is shown as a red line. b) $G_{forward,Static}$ of 5 nm finite-sized, static gold nanocrystal model at 300 K. Fitted Gaussian function is shown as a red line. The inset shows the third PDF peak centered at around 5 Å. c) Difference between lattice parameters from the snapshot and static $G_{forward}$ as a function of peak position. The dashed black line at 0 is added as a reference, whereas a red solid horizontal line passing from -0.00214 Å shows the lattice parameter differences between PDF-refined snapshot and static intensities of 5 nm finite-sized nanocrystal at 300 K. Fluctuations at high r are due to poor fits on diminished PDF peaks. d) Skewness distribution of $G_{forward}$ from the snapshot (blue) and static (red) coordinates of finite-sized 5 nm gold nanocrystal at 300 K.*

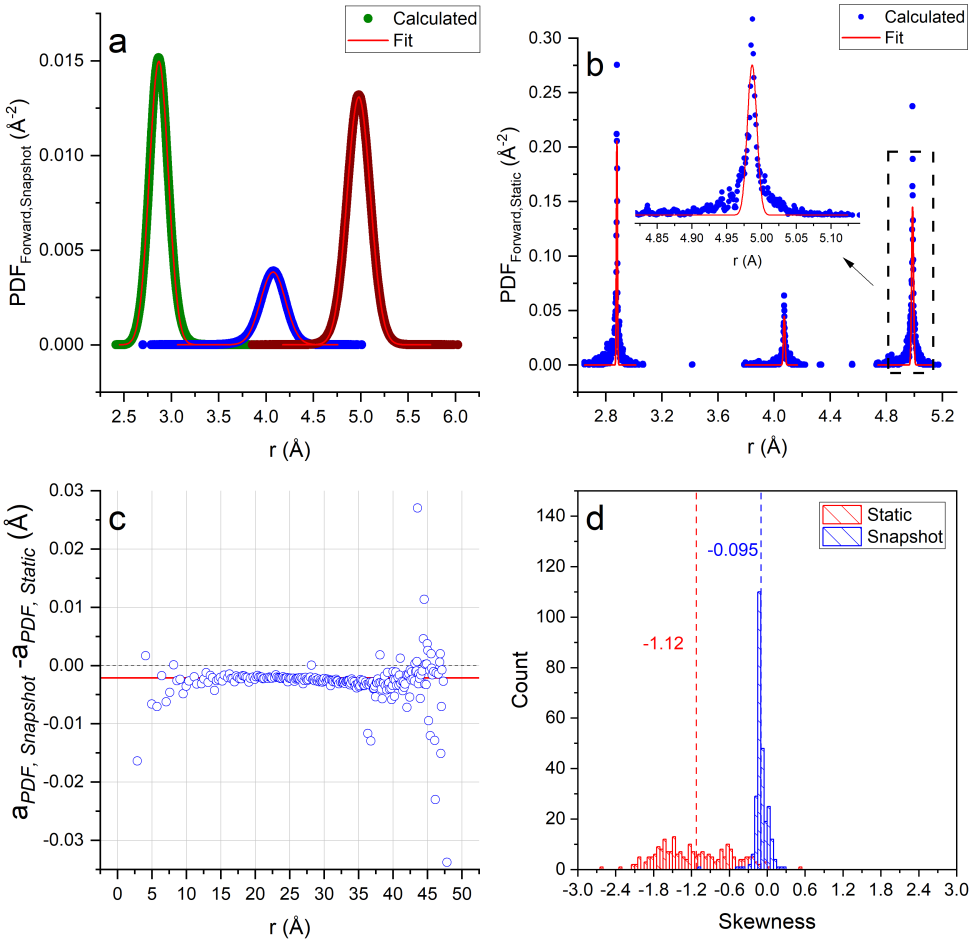
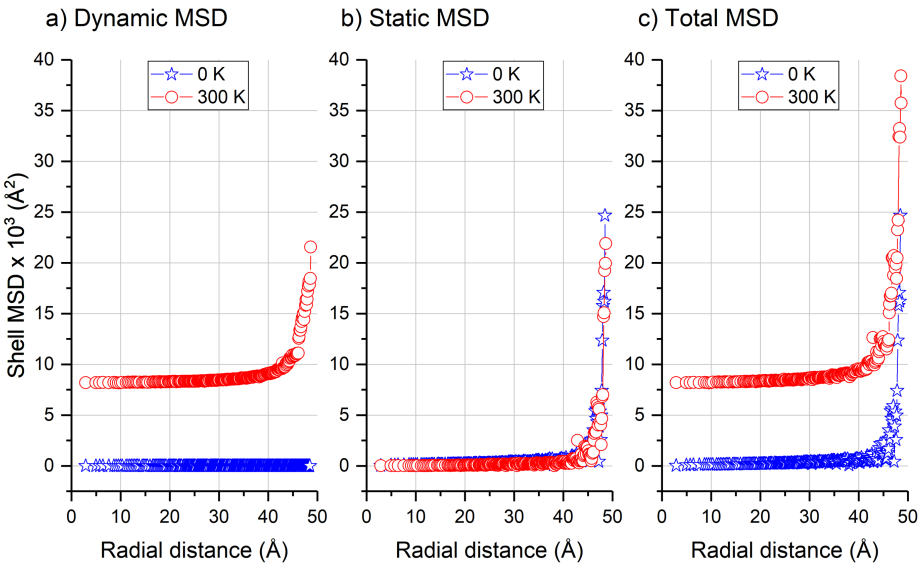


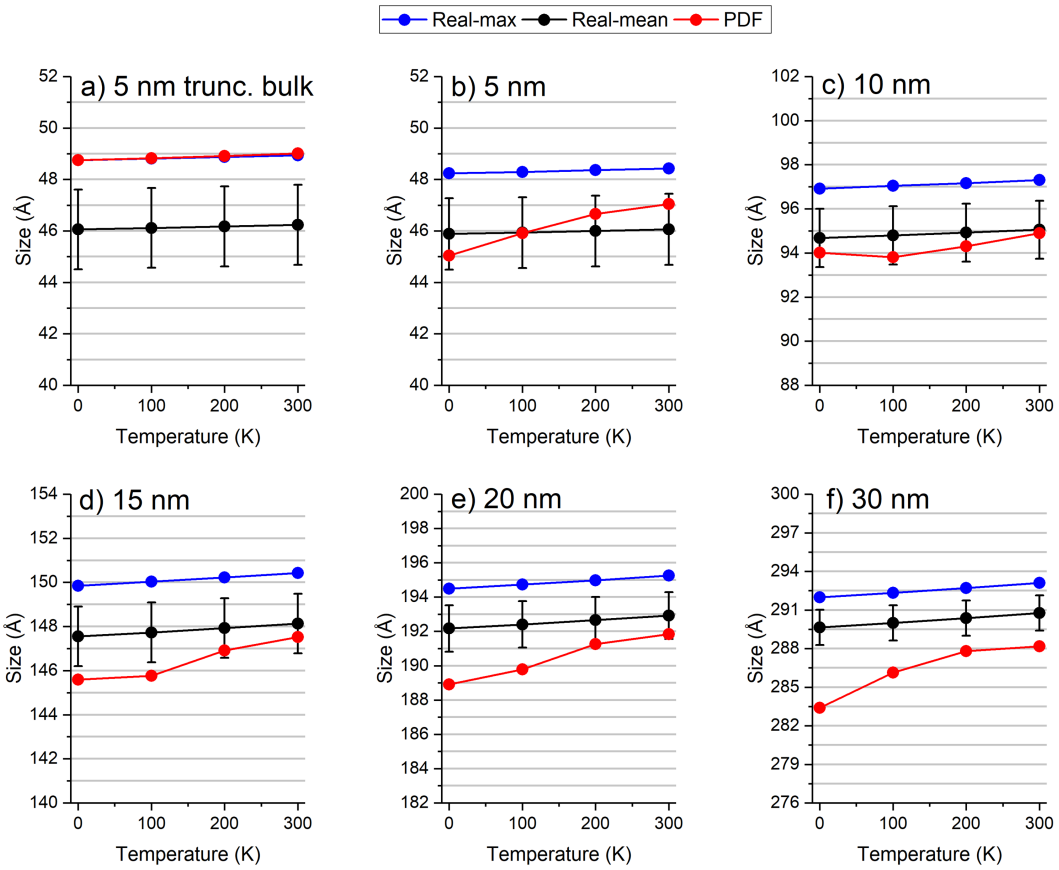
Figure 5.14: *Average a) dynamic, b) static and c) total MSD as a function of radial distance from the particle center computed over spherical shell volumes (with 0.125 Å thickness) at 0 and 300 K for finite-sized 10 nm gold nanocrystal.*



crystal does not experience surface reconstruction. The maximum deviation of PDF-refined particle size from "Real-max" is calculated as 0.1497 % for "PDF-snapshot" of the truncated-bulk crystal at 300 K (with δ_1). For this case δ_2 and "nodelta" peak-width models result in -1.4431 % and -5.2427 % deviations, which shows that the PDF-refined crystallite sizes are less than "Real-max" for these peak-width models.

In finite-sized nanocrystals and even with the best performing peak-width model, i.e. δ_1, PDF-refined sizes are below the maximum crystallite size, i.e., "Real-max", as shown in Figure 5.15(b-f). This is because the atoms in the outermost shell of the finite-sized crystals experience static displacements and do not preserve their coherency with the core atoms, unlike the truncated-bulk crystal. The snapshot intensity diffuses around the Bragg angle leading to earlier decay in the corresponding PDFs. Among different peak-width models, PDF-refined crystallite sizes with "nodelta" model deviate most from "Real-max": for example, the deviation of "PDF" is -9.3825 % with "nodelta", -4.8047 % with δ_2 and -2.8539 % with δ_1 peak-width model for 5 nm finite-sized nanocrystal

Figure 5.15: *Mean and maximum crystallite sizes over 0-300 K calculated in real space and refined from PDF analysis are shown for a) truncated-bulk (5 nm) and b-f) 5-30 nm finite-size nanocrystals. The peak-width parameter selected in PDF refinement is* δ_1.



at 300 K. However, the deviation from real space calculations decreases with increasing crystallite size for all peak-width models: as the particle size increases from 5 nm to 30 nm, the size error decreases from -6.61 % to -2.94 % at 0 K and from -2.85 % to -1.68 % at 300 K (with δ_1). Finally, focusing on temperature dependent trends we see that except for the 5 nm gold nanocrystal, sizes from PDF-refined and "Real-max" agree better with increasing temperature. This is attributed to PDF peaks acquiring more Gaussian-like profiles due to Gaussian distributed dynamic atom displacements exceeding the non-Gaussian-distributed static atom displacements (see Figures 5.14(a-c)).

Table 5.2: *Average diameters of the investigated nanopowders computed in real space and by PDF refinement of the diffraction data. Three different refinement results are presented from PDF analysis where different peak broadening models were employed in each refinement scheme.*

Size (nm)	Temperature (K)	Real Space Size (Å)		PDF Size (Å)		
		Max.	Mean	δ_1	δ_2	Nodelta
5	0	48.2	45.9 (14)	45.0 (3)	44.7 (3)	44.3 (3)
	100	48.3	45.9 (14)	45.9 (5)	45.0 (5)	43.3 (5)
	200	48.4	46.0 (14)	46.7 (7)	45.7 (6)	43.6 (6)
	300	48.4	46.1 (14)	47.0 (8)	46.1 (7)	43.9 (7)
10	0	96.9	94.7 (13)	94.0 (7)	93.5 (7)	93.1 (6)
	100	97.0	94.8 (13)	93.8 (10)	92.4 (9)	90.8 (9)
	200	97.2	94.9 (13)	94.3 (12)	92.6 (11)	90.4 (10)
	300	97.3	95.1 (13)	94.9 (14)	92.8 (13)	90.2 (12)
15	0	149.8	147.6 (14)	145.6 (11)	145.0 (10)	144.7 (10)
	100	150.0	147.7 (14)	145.8 (16)	143.6 (15)	141.8 (14)
	200	150.2	147.9 (14)	146.9 (20)	144.1 (18)	141.6 (17)
	300	150.4	148.1 (14)	147.5 (22)	144.5 (21)	141.4 (20)
20	0	194.5	192.2 (14)	188.9 (15)	188.2 (14)	187.9 (14)
	100	194.7	192.4 (14)	189.8 (22)	186.8 (20)	184.9 (20)
	200	195.0	192.6 (14)	191.3 (27)	187.9 (25)	185.2 (24)
	300	195.3	192.9 (14)	191.8 (30)	188.3 (28)	185.1 (27)
30	0	292.0	289.6 (14)	283.4 (26)	282.5 (26)	282.2 (26)
	100	292.3	290.0 (14)	286.1 (38)	282.2 (35)	280.1 (35)
	200	292.7	290.4 (14)	287.8 (44)	283.6 (42)	280.7 (41)
	300	293.1	290.8 (14)	288.2 (49)	283.7 (47)	280.4 (45)
5 (Bulk)	0	48.8	46.06 (16)	48.7 (3)	48.7 (3)	48.7 (3)
	100	48.8	46.1 (16)	48.8 (5)	48.2 (5)	46.9 (4)
	200	48.9	46.2 (16)	48.9 (6)	48.2(6)	46.5 (5)
	300	48.9	46.2 (16)	49.0 (7)	48.2 (7)	46.4 (6)

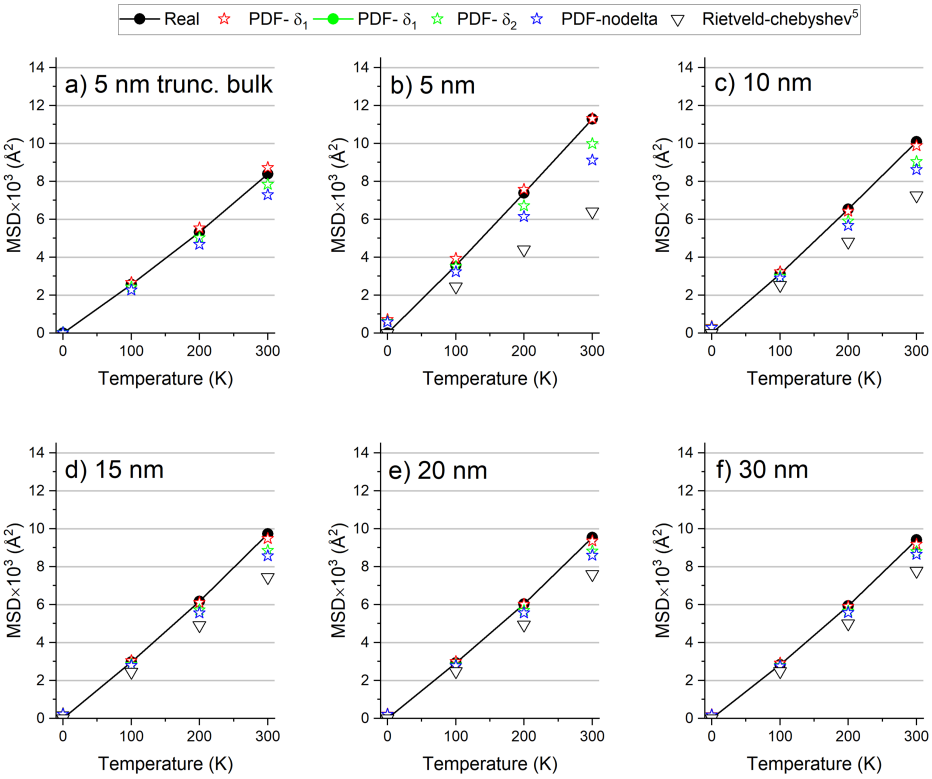
5.7.3 MSD

Figure 5.16 shows the average MSDs with respect to temperature for a 5 nm truncated-bulk (5.16(a)) and five finite-sized nanocrystals (5.16(b-f)) with sizes from 5 to 30 nm. The Real-space computed dynamic MSDs from atomic coordinates, i.e. "Real", were obtained from (3.4) and PDF-refined MSDs from corresponding diffraction data with different correlation parameter models are shown separately. In both nanocrystal models, MSDs from both analyses are linearly dependent on temperature and increase

with higher temperature indicating that the PDF-refined MSDs are predominantly of dynamic type -since static MSDs are temperature independent [56]-: the Real-MSDs of truncated-bulk model (Figure 5.16(a)) are calculated as 2.558×10^{-3} Å^2, 5.317×10^{-3} Å^2, and 8.395×10^{-3} Å^2 at 100, 200, and 300 K, and are comparable to the MSD of bulk gold reported earlier [21] with 2.686×10^{-3} Å^2, 5.364×10^{-3} Å^2, and 8.042×10^{-3} Å^2 at 100, 200, and 300 K, respectively. In finite-sized nanocrystals (Figures 5.16(b-f)), Real-MSDs show a strong particle size dependency: At 300 K, we calculated 11.281×10^{-3} Å^2, 10.089×10^{-3} Å^2, 9.725×10^{-3} Å^2, 9.544×10^{-3} Å^2, and 9.422×10^{-3} Å^2 for 5, 10, 15, 20, and 30 nm nanocrystals (see Table 5.3). This decrease in Real-MSDs with increasing particle size results from decreasing proportion of surface atoms having enhanced dynamic displacements relative to core atoms which was experimentally shown as well [70, 75].

When we focus on PDF-refined MSDs, we see that different correlation models result in slightly different average MSDs. Among the three models, refined MSDs without a correlation parameter ("nodelta") are the lowest, followed by δ_2 and δ_1 (see Table 5.3). Particle size and temperature-dependent trends in PDF-refined MSDs are like those from real space calculations irrespective of the selected correlation parameter, however, real space computed and PDF-refined MSDs agree the most when the correlation parameter δ_1 is selected. The superior performance of δ_1 is consistent with past work [64] suggesting δ_1 for PDF refinement of diffraction data obtained at $T \geq \theta_{Debye}$ for all selected temperatures -except 100 K which is below the expected Debye temperature (θ_{Debye}) of all our nanocrystal models [76]. The unexpected performance of δ_1 below its suggested temperature range was mentioned in other studies [61, 77] as well. Quantifying the accuracy of PDF-refined MSDs is challenging since the finite breadth of PDF peaks corresponds to combined static and dynamic atom displacements [68], but only dynamic displacements are Gaussian-distributed -compatible with the peak fitting scheme of DiffpyCMI. Moreover, as shown before in Figures 5.7(e-f), PDF-refined MSDs depend strongly on $2\theta_{\max}$

Figure 5.16: *Dynamic MSD vs. temperature calculated from atomic coordinates (Real), PDF refinement (PDF) and Rietveld refinement of diffraction data for a) 5 nm truncated-bulk crystal and b-f) 5-30 nm finite-sized nanocrystals. PDF-nodelta indicates the refinement result with no peak sharpening factor. A fifth-order Chebyshev polynomial was used to subtract thermal diffuse scattering during Rietveld refinement.*



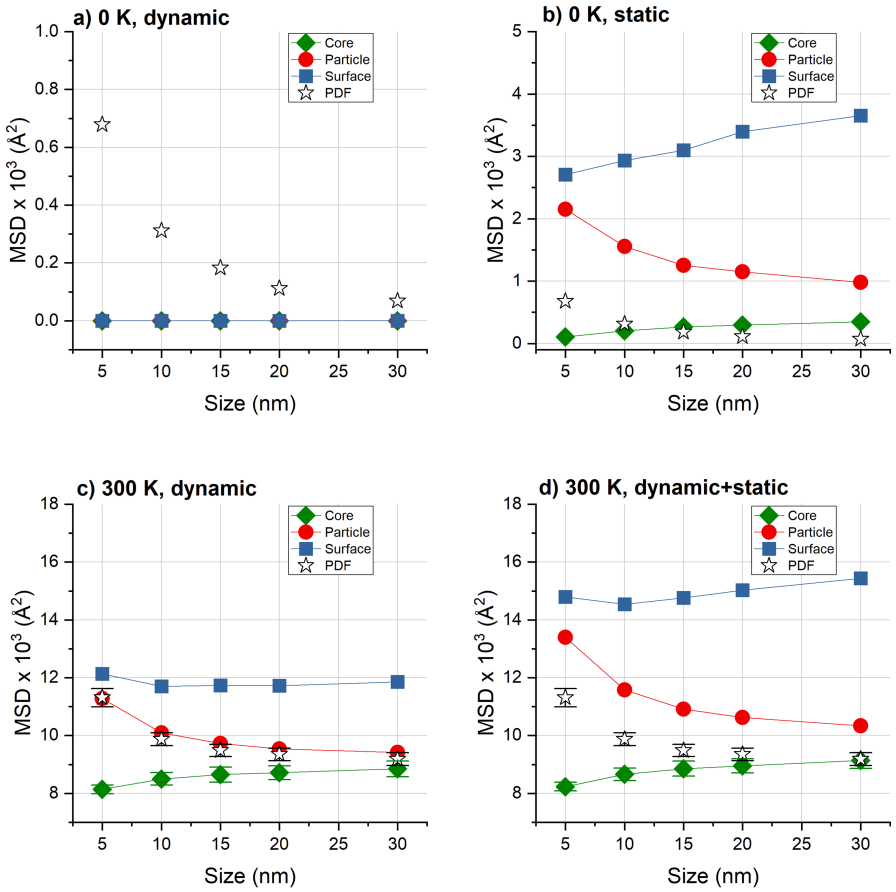
especially at low temperatures (at 0 K, PDF-refined MSD of truncated-bulk crystal for $2\theta_{\max} = 55°$ is $0.027 \times 10^{-3} \mathring{A}^2$, and for $2\theta_{\max} = 180°$ is $0.014 \times 10^{-3}\ \mathring{A}^2$). Hence, for a fair comparison, we limit ourselves to 300 K and evaluate the performance of PDF-refined MSDs taking real-space computed dynamic displacements as reference. Accordingly, at 300 K, the agreement between real space and PDF-refined MSDs is within 3.88 % for truncated-bulk crystal model (with δ_1) and within 3 % for finite-sized nanocrystals. This error in the truncated-bulk crystal is explained by the inadequacy of the peak sharpening parameters in modelling the thermal diffuse scattering. However, the lower error from finite-sized nanocrystal relative to truncated-bulk crystal is misleading and implies that

Table 5.3: *Average MSDs of the investigated nanopowders calculated in real space and by PDF refinement of the simulated diffraction data. Three different refinement results are presented from PDF analysis where different peak broadening models were employed in each refinement scheme.*

Size (nm)	Temperature (K)	Real Space MSD ($\times 10^{-3}$ Å^2)		PDF MSD ($\times 10^{-3}$ Å^2)		
		Dynamic	Static	δ_1	δ_2	Nodelta
5	0	0	2.15	0.70 (3)	0.62 (3)	0.58 (3)
	100	3.6 (2)	2.14	3.94 (9)	3.51 (7)	3.23 (6)
	200	7.4 (4)	2.11	7.57 (2)	6.71 (15)	6.14 (13)
	300	11.3 (5)	2.11	11.3 (3)	10.0 (2)	9.1 (2)
10	0	0	1.56	0.35 (3)	0.31 (2)	0.30 (2)
	100	3.12 (8)	1.52	3.23 (6)	2.99 (5)	2.89 (5)
	200	6.5 (2)	1.50	6.42 (13)	5.91 (11)	5.67 (10)
	300	10.1 (2)	1.49	9.9 (2)	9.0 (2)	8.6 (2)
15	0	0	1.25	0.25 (3)	0.23 (3)	0.22 (2)
	100	2.97 (5)	1.23	3.03 (6)	2.85 (5)	2.78 (5)
	200	6.18 (8)	1.21	6.11 (12)	5.72 (11)	5.56 (10)
	300	9.7 (2)	1.19	9.5 (2)	8.9 (2)	8.6 (2)
20	0	0	1.15	0.23 (3)	0.20 (3)	0.20 (3)
	100	2.92 (3)	1.12	2.99 (6)	2.82 (5)	2.77 (5)
	200	6.03 (6)	1.10	6.01 (13)	5.68 (11)	5.55 (12)
	300	9.54 (14)	1.08	9.3 (2)	8.8 (2)	8.6 (2)
30	0	0	0.98	0.19 (3)	0.17 (3)	0.17 (3)
	100	2.83 (2)	0.96	2.91 (7)	2.79 (6)	2.75 (6)
	200	5.93 (6)	0.94	5.90 (13)	5.65 (12)	5.57 (12)
	300	9.42 (15)	0.92	9.2 (2)	8.8 (2)	8.6 (2)
5 (Bulk)	0	0	0	0.03 (3)	0.02 (2)	0.02 (2)
	100	2.56 (9)	0	2.66 (6)	2.42 (5)	2.26 (4)
	200	5.3 (2)	0	5.55 (12)	5.02 (10)	4.68 (9)
	300	8.4 (3)	0	8.7 (2)	7.8 (2)	7.28 (15)

dynamic displacements are almost perfectly captured by PDF refinement even when the surface effect is present: In reality, PDF-refined MSDs must correspond to dynamic displacements only for the truncated-bulk particle (due to zero static displacement at the surface layer) and to the combined static and dynamic displacements for the finite-sized nanoparticle. The almost perfect match with real space computed dynamic MSDs, thus, clearly shows that static displacements are largely ignored in the refined MSDs. Nevertheless, compared to the MSDs obtained from Rietveld refinement, PDF refinement yields

Figure 5.17: *PDF-refined MSDs obtained by δ_1 from finite-sized nanocrystals with respect to crystal size (error bars reported from DiffpyCMI) along with real space calculations of core, surface and particle-wide averaged a) dynamic displacements at 0 K, b) static displacements at 0 K, c) dynamic displacements at 300 K, d) combined dynamic and static displacements at 300 K.*



a much closer estimate of the dynamic displacements with respect to the true values computed in real space (The procedure followed during Rietveld refinement of the diffraction data was reported previously [56]).

To investigate the local variation of MSDs over the volume of finite-sized nanocrystals, we computed in real space the local dynamic and static MSDs belonging to the core and surface regions separately and plotted them at 0 and 300 K in Figures 5.17(a-d) along with particle-wide average values, i.e. "Particle", and MSDs from PDF refinement, i.e.

"PDF". The same thickness value of 10 Å as in Figure 5.12 was selected to distinguish the surface and core regions of the nanocrystals. Figure 5.17(a) shows that real space calculations at 0 K predict zero dynamic displacements for both the core and the surface regions. However, the PDF-refined MSDs are finite and are maximized for the 5 nm finite-sized nanocrystal. As particle size increases, the PDF-refined MSDs decrease, but they do not entirely disappear even for the 30 nm nanocrystal. Two reasons explain the finite MSDs from PDF analysis at 0 K: 1) As seen in Figure 5.7(g), PDF-refined MSD for $2\theta_{\max} = 55^{\circ}$ is 0.7×10^{-3} Å^2, but for $2\theta_{\max} = 180^{\circ}$ it is nearly 0.31×10^{-3} Å^2 for the 5 nm nanocrystal. 2) Although no dynamic displacement is present at 0 K, static atom displacements exist even for the largest nanocrystal and contribute to the PDF-refined MSDs. This is seen by comparing Figures 5.7(e) and 5.7(g): For $2\theta_{\max} = 55^{\circ}$, PDF-refined MSD of the truncated-bulk 5 nm nanocrystal is 0.027×10^{-3} Å^2 which is less than 4 % of that of the finite-sized 5 nm nanocrystal (0.7×10^{-3} Å^2). That being the case, no correlation exists between the PDF-refined MSDs in Figure 5.17(b) and the static displacements of the particle core or surface. Instead, PDF-refined MSDs are closest to the average static displacement of the core, overestimate them in small particle sizes and underestimate them in large ones. This shows that the large proportion of surface atoms and their static displacements are minimally captured by PDF refinement in smaller nanocrystals, but these do not contribute enough to enable refined MSDs to follow the particle-wide average static displacements, irrespective of the crystal size.

5.8 Summary and Conclusions

In this work, we investigated the effect of nanocrystal surface on the lattice parameters, crystallite sizes and dynamic atom displacements obtained from PDF refinement of diffraction data. A truncated-bulk nanocrystal with nanoscale dimensions but identical atomic arrangement in its core and surface; and a finite-sized nanocrystal which presents

surface reconstruction resulting in a different atomic arrangement in its core and surface were analyzed. The particle size and temperature range of our interest were 5-30 nm and 0-300 K. Analytical diffraction data with no sampling or photon counting statistics were used to correlate PDF analysis results with real space calculations under ideal conditions. The main conclusions are listed as follows:

- Relative amounts of static and dynamic atom displacements in nanocrystals affected the accuracy of crystallographic parameters refined from PDF analysis: While static atom displacements were non-Gaussian, dynamic atom displacements were Gaussian distributed. Hence conditions promoting static displacements to be more dominant compared to dynamic displacements, either small particle size and/or low temperature, resulted in distortions in PDF peaks from Gaussian profiles. This caused degradation in the fitting quality during PDF refinement and had implications on the refined parameters.

- Average lattice parameters obtained from atomistic real space calculations and refined from PDF analysis agreed almost perfectly at all temperatures for truncated-bulk nanocrystals. However, PDF analysis underestimated the average lattice parameters of finite-sized nanocrystals. The underestimation was as high as 0.16 % for 5 nm nanocrystals at 0 K but it reduced to 0.021 % for the 30 nm nanocrystals at 300 K. Separate calculations of core- and surface-averaged lattice parameters of finite-sized nanocrystals showed that PDF-refined lattice parameters correlated with the core lattice parameters at 0 K indicating that static atom displacements at the surface was invisible to PDF analysis (even when MSD was refined). At finite temperature, PDF-refined lattice parameters neither matched with the core nor the surface lattice parameters but approached the surface parameters thus deviating from core lattice parameters for smaller nanocrystals. This was explained by the

enhanced dynamic displacements of atoms surpassing the static displacements resulting in better peak fitting and more accurate peak centers during PDF refinement.

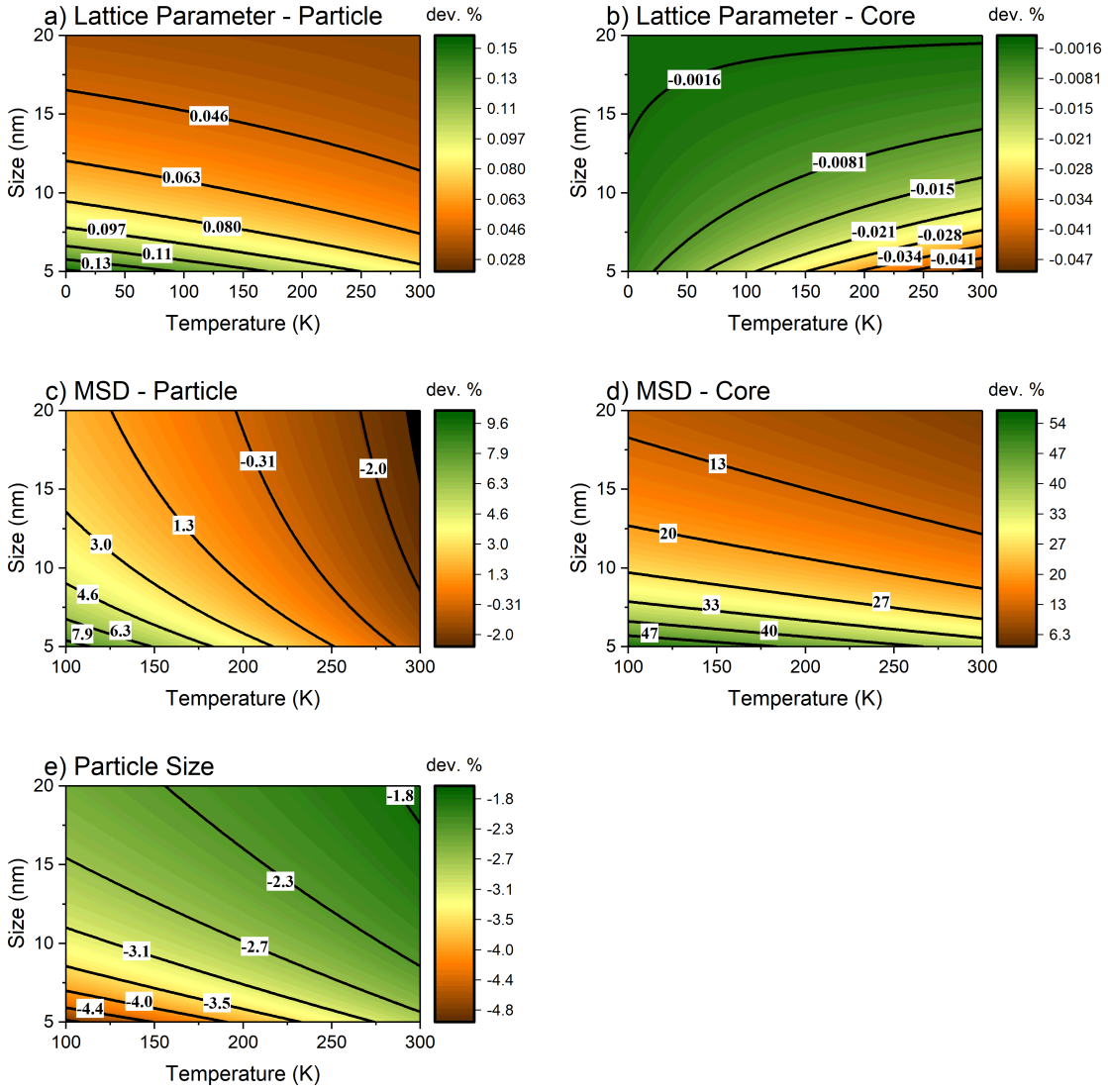
- Particle sizes from the PDF refinement of 5 nm truncated-bulk crystal corresponded with the maximum diameter of the particle within an error less than 0.15 %. In finite-sized particles, PDF refinement underestimated both maximum and mean diameters at large particle sizes. The largest deviation (-6.61 %) from the maximum particle diameter was at 0 K for the 5 nm particle. This showed that the combined static and dynamic surface atom displacements caused the high-r range PDF peaks to broaden and dampen, leading to smaller refined sizes. This deviation decreased to -2.85 % at 300 K. Increasing agreement with temperature was attributed to total (static+dynamic) atomic displacement distributions resembling the Gaussian profile. Moreover, the accuracy of particle size strongly depended on the selected peak-width model, with "nodelta" as the worst peak-width model and δ_1 as the best.

- MSDs refined from PDF analysis agreed with an error of 3.88 % with the dynamic MSDs of truncated-bulk nanocrystals. The error was attributed to the peak sharpening parameters neglecting the directional dependence of correlated motion. These errors (total MSD) increased for finite-sized nanocrystals to -15 %. On the other hand, dynamic MSD errors were around -3 %. Among the two peak-width models, δ_1 performed better than δ_2 with closer MSDs to the real space computed particle-averaged MSDs. Focusing on how PDF-refined MSDs relate with different regions of the finite-sized nanoparticle, we observed two different behaviors: when the dominant contribution to atomic displacement was the static surface atom displacement (e.g. at 0 K), PDF significantly overestimated the true dynamic MSDs. At

300 K, dynamic displacements dominated over static displacements, PDF peak profiles appeared more Gaussian and fitting performance improved resulting in good agreement between PDF-refined MSDs and particle-wide average dynamic MSDs computed in real space.

These results show that PDF refinement of diffraction data from small nanocrystals presents deviations from the true crystallographic descriptors even under ideal conditions. These deviations increase with decreasing crystallite size and temperature as shown in Figure 5.18. The expected error in the crystallographic parameters obtained from PDF analysis can be estimated from our computational analysis over 0-300 K, and underlying structures of nanocrystals smaller than 30 nm can be obtained more reliably. Since static displacements do not depend on temperature while dynamic displacements do, an appropriate strategy to obtain better estimates of structural information from the surface regions can be to perform PDF refinements over multiple diffraction datasets collected at separate temperatures.

Figure 5.18: *Particle size and temperature dependent deviation of PDF-refined a) particle-averaged lattice parameters, b) core lattice parameters, c) particle-averaged MSDs, d) core MSDs, e) crystallite size from real space calculations.*



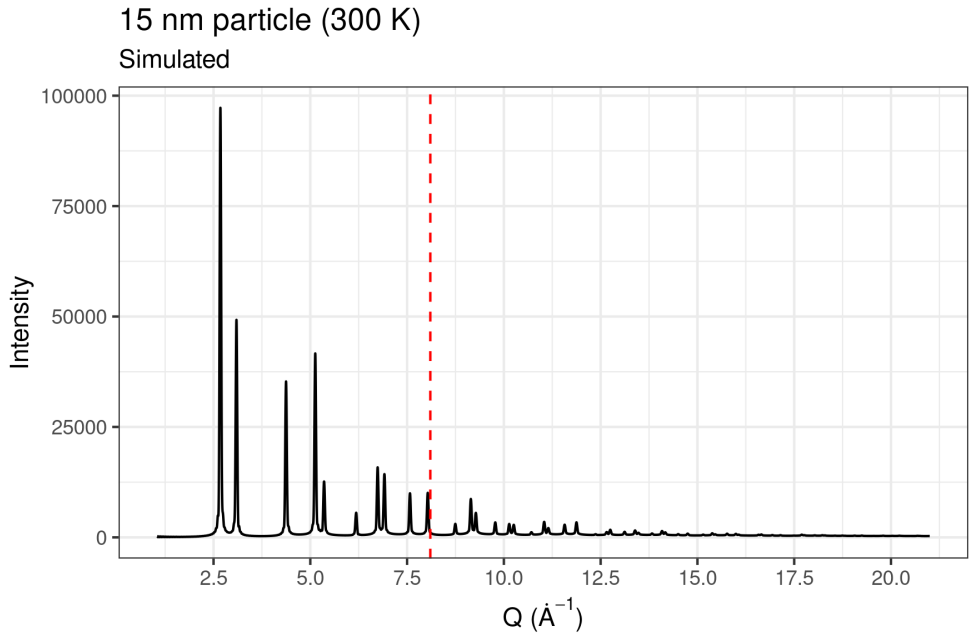
6. PERFORMING THE PDF REFINEMENT ON EXPERIMENTALLY MEASURED PDF WITH A LABORATORY X-RAY DIFFRACTOMETER

6.1 Introduction

In this chapter, we will explain our experimental work on PDF refinement of gold nanoparticles. In general, PDF experiments are conducted in high-energy synchrotrons. The reason is that the resolution of PDF is inversely related to the wavelength of the X-ray beam used in measurement. The higher the energy of the beam, the smaller the wavelength is. Typically, X-ray wavelength around 0.21 Å is provided in the synchrotron, making the maximum achievable momentum transfer vector magnitude around $Q_{max} \approx$ 27 Å^{-1}. Moreover, the flux of the beam is high, providing faster measurement times. However, the number of synchrotrons is limited in the world. Once the scientists apply and get accepted for beamtime in the synchrotron, usually, they wait in a long queue. In contrast, laboratory X-ray diffractometers are common. However, their energy is relatively low compared to synchrotron sources. Here, we used a laboratory diffractometer, which has a wavelength of 1.54 Å for diffraction measurement of 14 nm gold nanoparticles purchased from the nanografi. The simulated diffraction data of 15 nm gold nanocrystal obtained from MD simulations at 300 K is shown in Figure 6.1. The vertical dashed line is the upper limit that we can reach with the lab diffractometer in this study. The full range corresponds to the range accessible with synchrotron beams. Obviously, the number of Bragg peaks is less in the former case, which will negatively affect the resolution of PDF data as will be shown later. Our sample is in powder form. Following measurements, we will first attempt to analyse the measured PDF without using any model, then by using PDF refinement as attenuated crystal modeling, and finally, by using MD as a tool for

structure solution.

Figure 6.1: *Simulated diffraction intensity of 15 nm gold nanoparticle at room temperature. The dashed vertical line is the upper limit for our lab X-ray diffractometer. Wavelength corresponds to 0.21 Å.*



6.2 Diffraction Pattern Measurement of 14 nm Gold Nanoparticle Powder with Lab Diffractometer

Diffraction measurements for PDF analysis are usually called total scattering experiments. It is called "total" scattering since both Bragg and diffuse intensity are used in PDF analysis. In the case of Rietveld analysis, we only use Bragg intensity. The diffuse intensity is embedded into the background. In order to separate it from other sources in the background, such as air scattering, scattering from instrument parts, and scattering from the sample holder, another measurement from an empty sample holder is required. Therefore, we did two measurements using the sample holder with the sample and the sample holder without the sample. We used a "zero-background" sample holder that minimizes

scattering from the sample holder. Measurements were performed in reflection geometry from $2\theta = 30°$ to $165°$ with $d2\theta$ step of $0.02°$ for two different amounts of gold nanopowder, 50 mg and 100 mg. At each step, 1 second measurement time was selected. The measurement with the selected settings took around 112 minutes. With maximum 2θ angle, we achieved Q_{max} =8.08 Å^{-1}. The sample holder, sample, and diffractometer used in the study are shown in Figure 6.2.

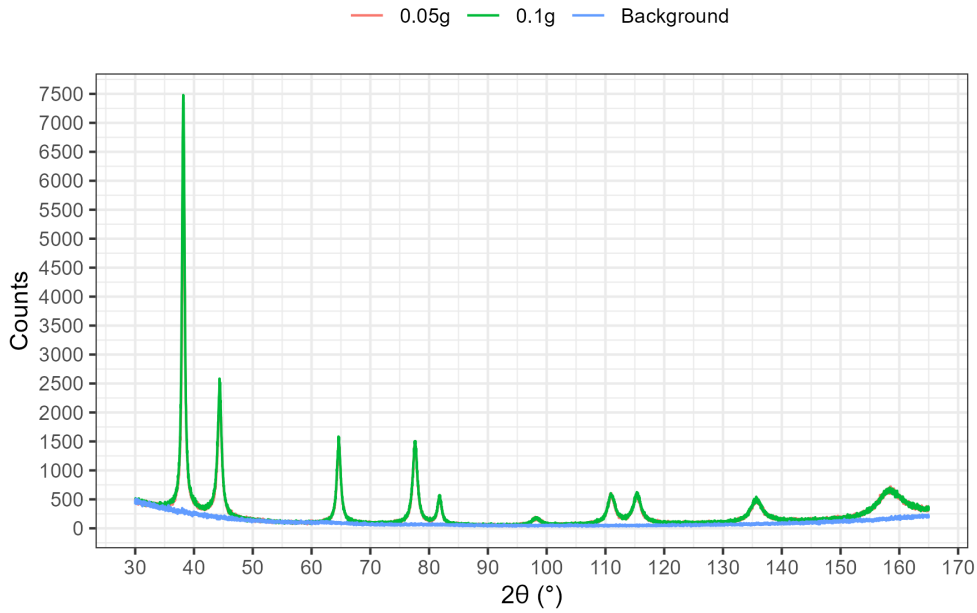
Figure 6.2: *Top left) Measuring the 100 mg of powder in the lab, top middle) sealed glass bottle containing the powder and cleaned sample holder - "zero-background", right) poured powder on the sample holder, bottom left) XRD measurement in reflection geometry with Bruker D8 DISCOVER diffractometer (with Cu tube) in the OzUBEX.*



The measured X-ray diffraction pattern for two different amounts of powders with 50 and 100 mg is shown in Figure 6.3 along with background intensity. First, the difference between the two patterns is negligible, indicating that 50 mg of sample is enough to get the diffraction signal. Second, we observed 10 Bragg peaks with selected wavelength

and angular range, which is fully consistent with simulated diffraction data as shown in Figure 6.1 for gold material. Therefore, we can tell that this diffraction pattern belongs to gold material. Third, Bragg peaks are sharp and well separated from each other, indicating good crystallinity in the sample.

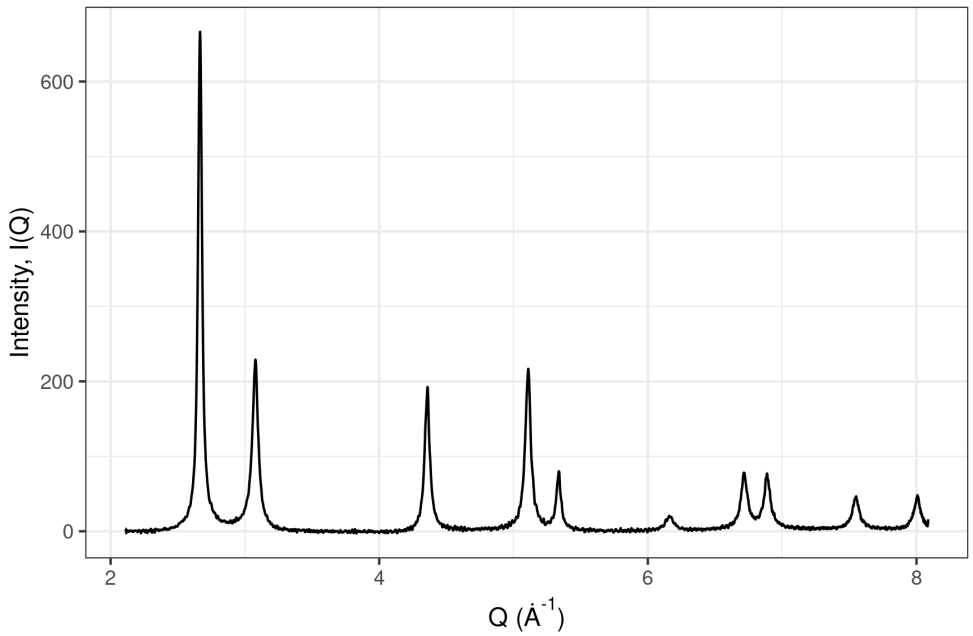
Figure 6.3: *PXRD pattern of gold nanoparticle with background intensity for 50 and 100 mg of powder sample. The amount of sample has a negligible effect on measured data.*



Once measurements were done, background intensity was subtracted from the total intensity to get only sample-related intensity as $I_{sample} = I_{total} - I_{background}$, and the polarization correction was applied. The background-subtracted intensity, I_{sample}, as a function of diffraction vector magnitude Q is shown in Figure 6.4. For conversion from 2θ to Q, the relation $Q = \frac{4\pi \sin\theta}{\lambda}$ is used. The intensity profile is then used as an input to the software PDFGetX3 to obtain the measured PDF shown in Figure 6.5. At first sight, we can approximately determine average particle size by looking at the r-position position where all peaks decayed. From the measured PDF plot, this position is around 150 Å, beyond which no significant PDF peak is observed. Thus, the average nanoparticle

size is qualitatively determined as 150 Å in our sample.

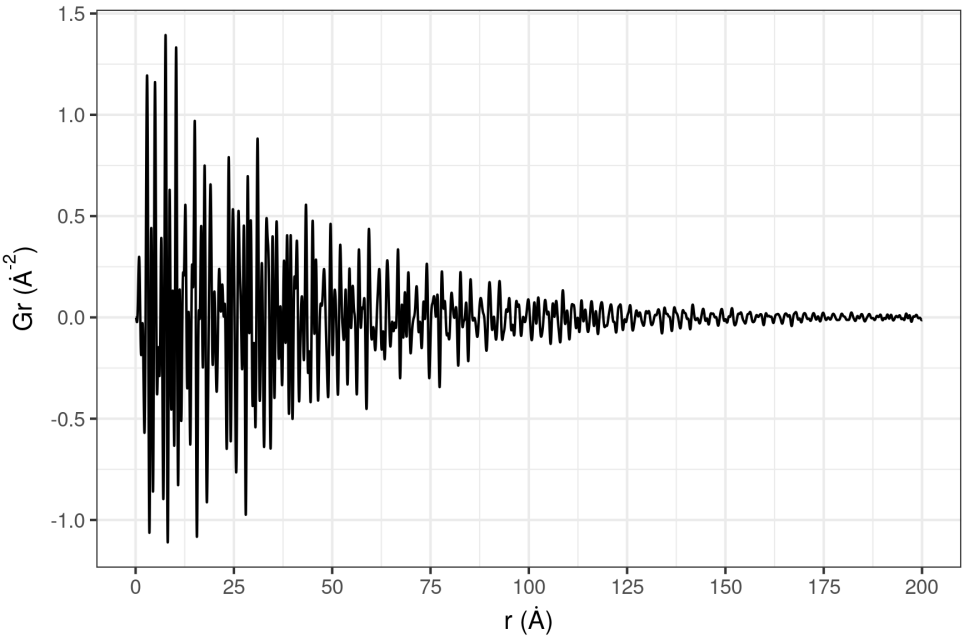
Figure 6.4: *Measured PXRD pattern (background subtracted and polarization corrected) of gold nanoparticle as a function of diffraction vector magnitude. Other corrections such as smoothening and* $\mathrm{K}\alpha_2$ *stripping were applied with the QualX software [78].*



6.3 Model-Free Analysis of Measured PDF

Model-free analysis of measured PDF is the method of obtaining structural information from the PDF without using any structural model refinement algorithm. This includes obtaining interatomic distance from PDF peak position, MSD from peak width, and particle size from peak decay. First, particle size is already obtained as 150 Å as mentioned in Figure 6.5. Second, peak widths are not reliable at this point to extract the MSD since low resolution due to small Q_{max} has additional peak broadening, making accurate determination of MSD challenging. Third, interatomic distance can be obtained by fitting the Gaussian profile to the measured PDF. Then, these interatomic distances can be matched with that of a known structure.

Figure 6.5: *PDF pattern of gold nanoparticle obtained by Fourier transformation using the measured intensity shown in Figure 6.4. Note that particle size is obtained as 150 Å, which is the position in the x-axis of the PDF plot beyond which no significant peaks exist.*



From the measured PXRD data, we assume that the structure is gold since we observed all expected Bragg peaks. The first 8 interatomic distances of bulk gold at room temperature are obtained from the atomic model as 2.8835, 4.0785, 4.9945, 5.7675, 6.4485, 7.0635, 7.6295, and 8.1565 Å, respectively. Atom pairs making the mentioned interatomic distances are illustrated with the red line in the unit cell structure of bulk gold as shown in Figure 6.6. These distances are added as a vertical line in the measuredPDFplot as shown in Figure 6.7. First,PDFpeaks below 2 Å can not be assigned to any Au-Au distance since two gold atoms cannot physically have bond lengths at such a short distance. These might be measurement errors. Second, most of the vertical dashed lines match well with measured PDF peak positions, indicating the structure is gold. However, it is clear that some peaks slightly shifted, and some are totally mismatched with the expected interatomic distance. For example, the 6^{th}, 8^{th} and 10^{th} vertical lines don't match with

any peaks of the measured PDF. At this point, two questions arise about whether this mismatch is related to the underlying structure or a side effect of finite Q_{max} due to a lab diffractometer. To clarify this problem, we simulated PDF pattern of 15 nm nanocrystal at 300 K obtained from MD simulations at two different Q_{max} values of 8.08 Å^{-1} and 21 Å^{-1}, which correspond to Q_{max} accessible with lab diffractometer and synchrotron, respectively, as shown in Figure 6.8. From the simulated PDF pattern, it is clear that decreasing Q_{max} has an adverse effect on PDF. This includes peak shifting, additional peak broadening, and the appearance of additional peaks called termination ripples. Note that all of these are not structure-related and can lead to incorrect interpretation of PDF results. Therefore, a more reliable approach that can calculate PDF from some model and refine its parameters to minimize the difference between calculated and measured PDF. In addition, the approach should include the finite Q_{max} effect on the calculated PDF. We will discuss in the next section such an approach.

Figure 6.6: *Unit cell model for FCC gold structure is shown. Red arrows show the first 10 interatomic distances between atom pairs. In case of distances exceeding one unit cell, a second unit cell is added with a blue plane separating two unit cells.*

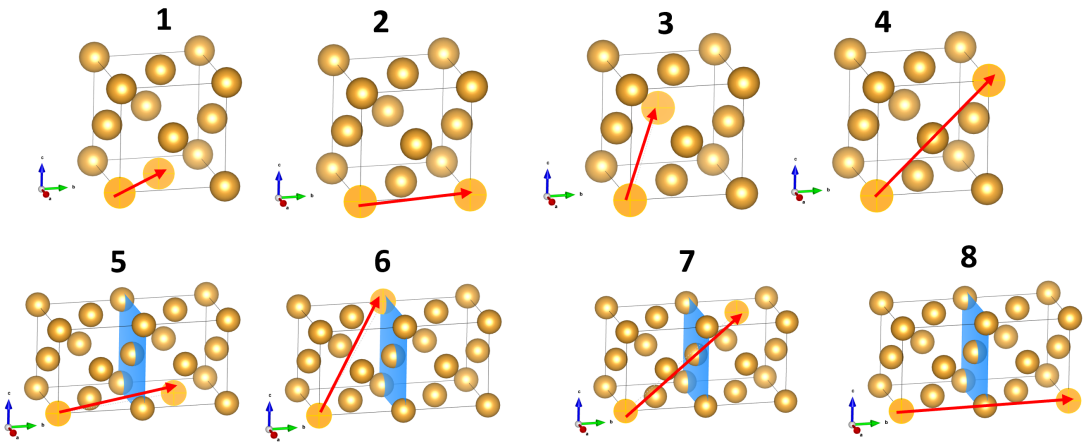


Figure 6.7: *Measured PDF pattern of gold nanoparticle. Only r-range up to 15 Å is shown. The first 10 vertical dashed lines correspond to atomic pairs shown inside FCC unit cell as illustrated in Figure 6.6.*

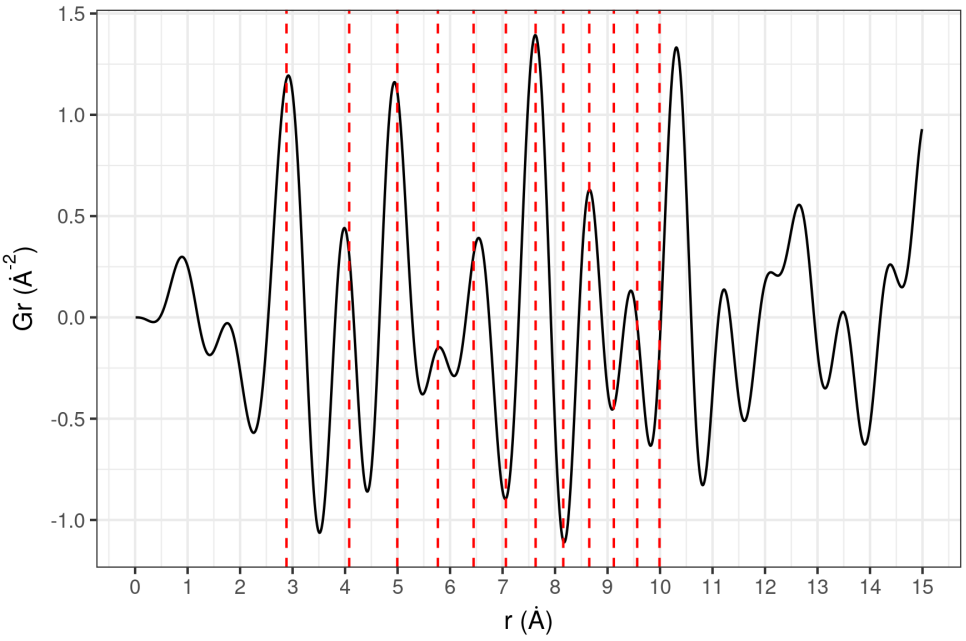
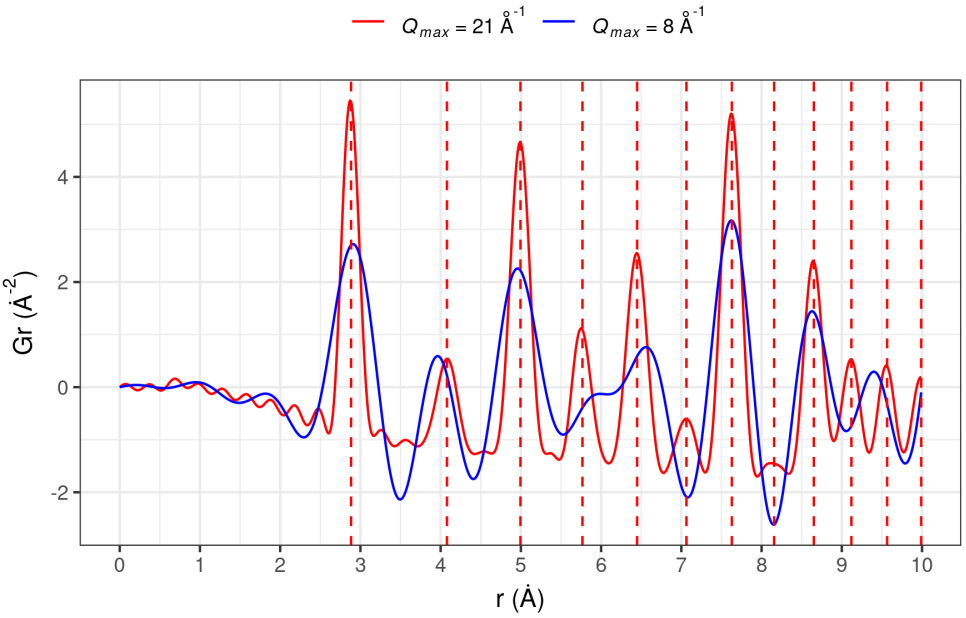


Figure 6.8: *Simulated PDF pattern of gold nanoparticle obtained at two different Q_{max}: 8.08 Å^{-1} and 21 Å^{-1}. Peaks are broadened at low Q, and some of the peaks are lost.*



6.4 PDF Refinement of Measured PDF by Including Finite Q_{max} Effect

We seek to extract the structural parameters of gold nanoparticles in a reliable approach that includes the finite Q_{max} effect on the calculated PDF. Below, two approaches will be explained. These are attenuated crystal modeling and MD-assisted modeling. While the former is same as unit cell modeling with an ideal crystal structure without static atomic displacements, the latter includes more realistic particles with surface atomic displacements obtained from MD simulations. Moreover, the latter method includes particle size distribution.

6.4.1 Attenuated Crystal Modeling of PDF from Gold Nanocrystals

Attenuated Crystal Modeling (ACM) uses the same algorithm explained in Chapter 5. First, it creates a periodic supercell box structure from the unit cell, where the dimensions of the supercell box are larger than the desired maximum interatomic distance in PDF. Unit cells are identical everywhere throughout the box without any atomic displacements. PDF of this box corresponds to bulk PDF. Second, calculated bulk PDF is attenuated with particle shape factor that decreases peaks with increasing interatomic distance due to the finite size of the particle. Third, a Gaussian peak profile is created for each unique interatomic distance to account for atomic displacements. Fourth, PDF is convoluted with window function to include the finite Q_{max} effect on calculated PDF. Lastly, structural parameters such as lattice parameter, MSD, particle size, and correlated atomic motion parameter are refined along the scale factor until the difference between the measured and calculated PDFs is minimized according to the following relation:

$$R_{\mathrm{wp}} = \sqrt{\frac{\sum_i w_i \left[G_{\mathrm{obs}}\left(r_i\right) - G_{\mathrm{calc}}\left(r_i\right)\right]^2}{\sum_i w_i \left[G_{\mathrm{obs}}\left(r_i\right)\right]^2}} \tag{6.1}$$

where w_i, G_{obs}, G_{calc} are weight, measured PDF, and calculated PDF at i^{th} point.

Refinement methodology is as follows: 1) refine the scale and lattice parameter, 2) add the MSD and refine all three, 3) add the particle size and refine all four, 4) fix all and refine only correlated motion parameter δ_1, 5) free all, and refine all. Instrumental-related broadening and dampening parameters, Q_{damp} and Q_{broad}, were obtained from the standard corundum sample (Standard Reference Material (SRM) 1976c) and fixed during the refinements. The calculated PDF that agrees best with the measured PDF is shown in Figure 6.9 for three different r ranges: low-, mid-, and high-r ranges. By looking at the difference plot (green line), we notice that calculated and measured PDF agree better at low-r range or short-range correlation. In contrast, the deviation between the two is hight at the high-r range, where interatomic distances are comparable to the diameter of the nanoparticle. Quantitatively, residual factor Rw was calculated as 15.4 %, which is considered a good fit since it is below the acceptable range of 20 %. With this Rw, we obtained structural parameters shown in Table 6.1. Lattice parameter calculated as 4.0787 Å agrees well with the experimental value of 4.0782 Å for bulk gold [73]. It is well known that the lattice parameter decreases with nanocrystal size. However, the lattice parameter converges to the bulk value for nanocrystals with a size over 15 nm [56], which is the case here. In case of MSD, our calculated MSDMSD 15.61×10^{-3} Å^2 is higher than that of 15 nm gold nanocrystal obtained as 9.7×10^{-3} Å^2 from MD simulations [18]. One of the reasons for this discrepancy might be explained in terms of particle size distribution. In ACM modeling, we assumed that our powder sample is composed of nanocrystals with the same diameter, which is called a monodispersed system. Here, with this assumption, we calculated the average diameter as 150.8 Å. This seems unrealistic since almost always there is size distribution in synthesized gold nanocrystal powders. However, the ACM modeling is fast and gives us initial thoughts about the sample properties. In the next section, we will consider modeling the polydispersed system.

Figure 6.9: *Comparison of fit quality between the measured and calculated PDF from ACM modeling. The difference between the two PDFs is shifted below for clarity and shown as green line. Fitting range was between 0-150 Å. For clarity, r-range is divided into three ranges: a) low-r range (0-50 Å), b) mid-r range (50-100 Å), c) high-r range (100-150 Å). Note the disagreement at the high-r range.*

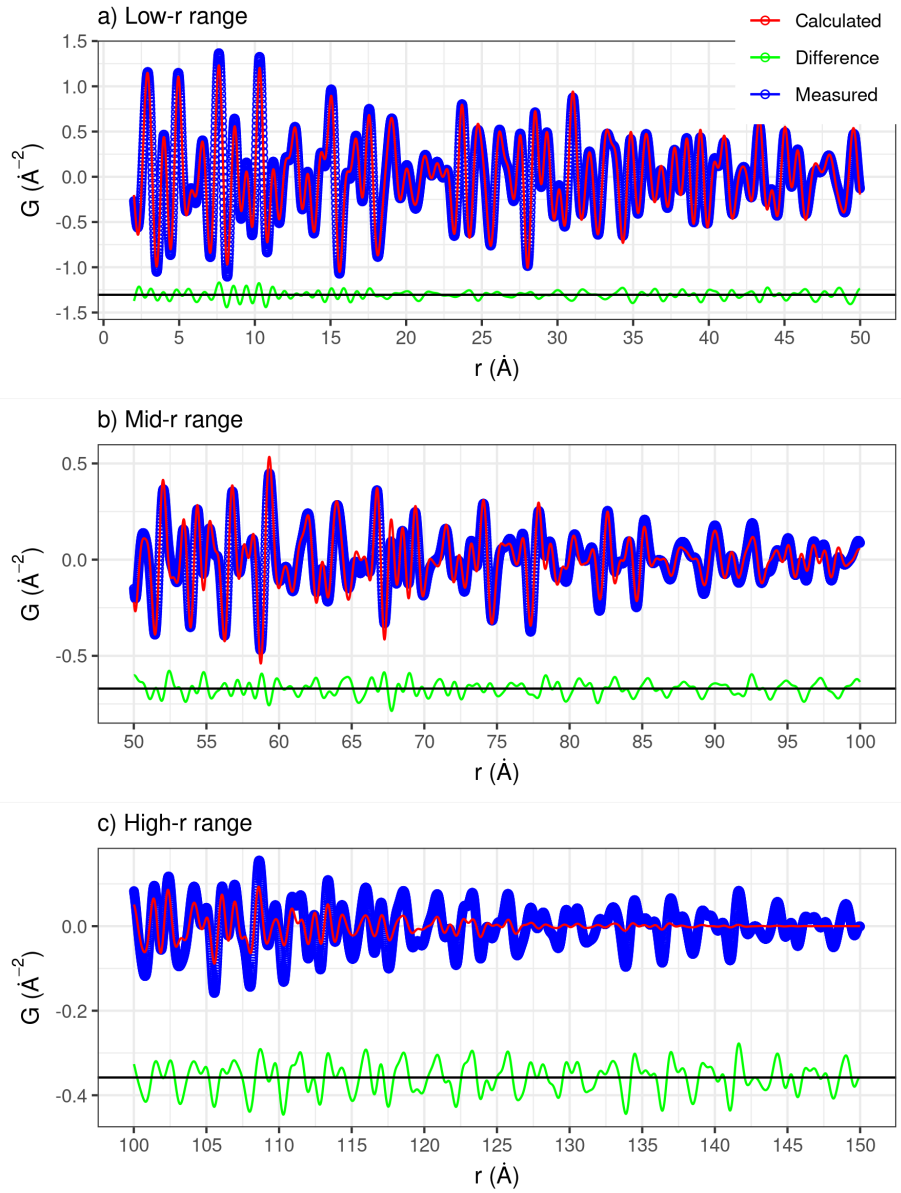


Table 6.1: *PDF refined structural parameters. ACM modeling strategy is used.*

Lattice Parameter (Å)	MSD ($\times 10^{-3}$ Å^2)	Diameter (Å)	Rw %
4.0787	15.61	150.8	15.4

6.4.2 MD-Assisted Modelling of PDF from Polydispersed Realistic Gold Nanocrystals

Based on the preliminary findings with ACM modeling, we will extend our modeled monodispersed system to a polydispersed system obtained from MD simulations. We will assume that our powder system is composed of realistic spherical gold nanocrystals of 5, 10, 15, 20, and 30 nm, with surface static atom displacements. With these nanocrystals, it is possible to create a set of polydispersed systems. In each system, particles have different lattice parameter - MSD combinations. We scanned around the lattice parameter and MSD obtained from ACM modeling. Lattice parameter and MSD ranges were selected as $4.0750 - 4.0810$ (Å) by 0.0002 Å step, and $10 - 25\,(\times 10^{-3}\,\text{Å}^2)$ by $0.5 \times 10^{-3}\,\text{Å}^2$ step, respectively. For a given lattice parameter, atomic coordinates of the core region of static particles are scaled with a_{new}/a_{old}, where a_{old} and a_{new} are average core lattice parameter of static particle and average core lattice parameter of a particle in the polydispersed system, respectively. For a given MSD, atomic displacements are added uniformly to the scaled atomic coordinates using Gaussian distribution. Assignments of lattice parameter and MSD are followed by PXRD calculation in Debyer and PDF calculation in PDFGetX3, respectively. An example of calculated PDFs for each particle size can be seen in Figure 6.10.

Each polydispersed system can be optimized to get size distribution based on (6.2). Once each point in lattice parameter - MSD space is optimized for size distribution, the one that agrees best with the measured PDF or with the lowest Rw is accepted as the best representing system. The total PDF of each point in lattice parameter - MSD space is given by:

$$\begin{aligned} G_{\text{calc}}\,(r) =& s_{5nm}G_{5nm}(r) + s_{10nm}G_{10nm}(r) + s_{15nm}G_{15nm}(r) \\ &+ s_{20nm}G_{20nm}(r) + s_{30nm}G_{30nm}(r) \end{aligned} \tag{6.2}$$

where G_{calc} , G_{5nm}, G_{10nm}, G_{15nm}, G_{20nm}, and G_{30nm} are PDF of polydispersed system, 5, 10, 15, 20, and 30 nm nanocrystals, respectively. Size-specific PDFs are shown in

Figure 6.10: *PDFs for particles used in polydispersed system. The particle sizes are 5, 10, 15, 20, and 30 nm.*

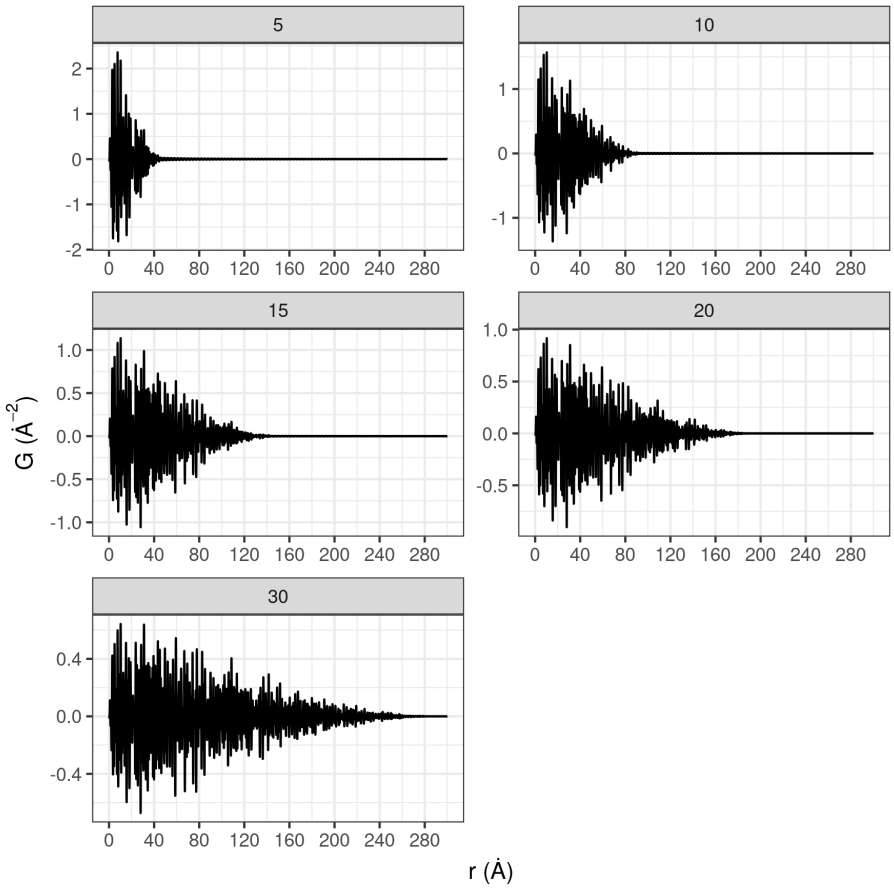


Figure 6.10. Multiplication factors are called scale factors that give weight to each particle size in a polydispersed system. Then, G_{calc} is used as an input to the optimized function (6.1) to find scale factors for each system. Optimized polydispersed systems in lattice parameter - MSD space is shown as a contour plot in Figure 6.11, where each point is colored based on residual factor Rw.

The best agreement is obtained by a polydispersed system in the contour plot that provided a minimum Rw of 13.6 %. The corresponding structural parameters are shown in Table 6.2, and the distribution of weights for particles is shown in Figure 6.12. First, the change in lattice parameter is negligible, and it is almost the same as the ACM modeling

Figure 6.11: *Lattice parameter - MSD space of polydispersed systems. Each point in the contour plot is a polydispersed system and is colored based on agreement factor Rw. The smaller Rw is, the better the agreement between the calculated PDF and measured PDF. The polydispersed system is composed of 5, 10, 15, 20, and 30 nm diameter gold nanocrystals.*

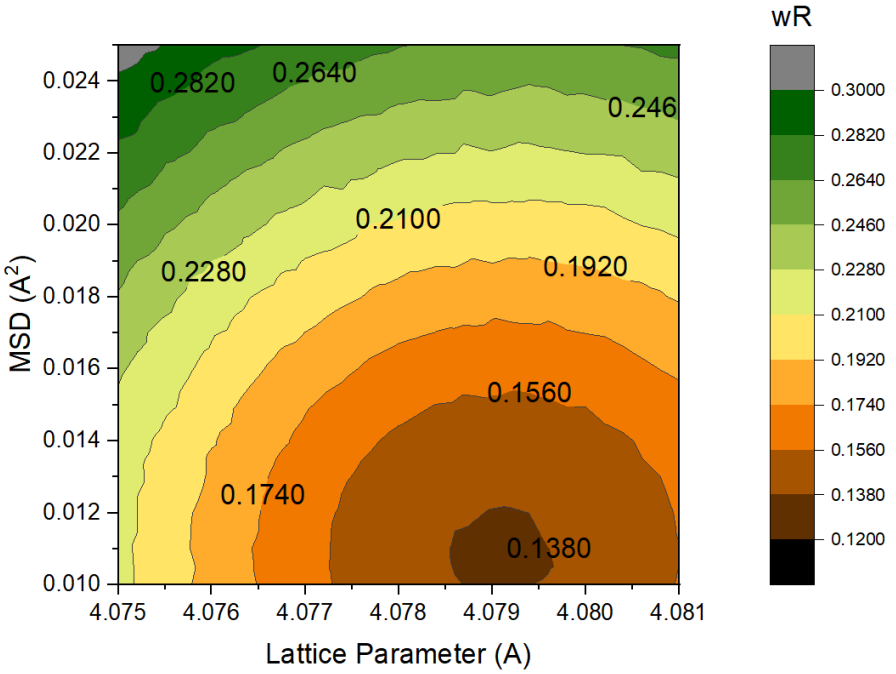
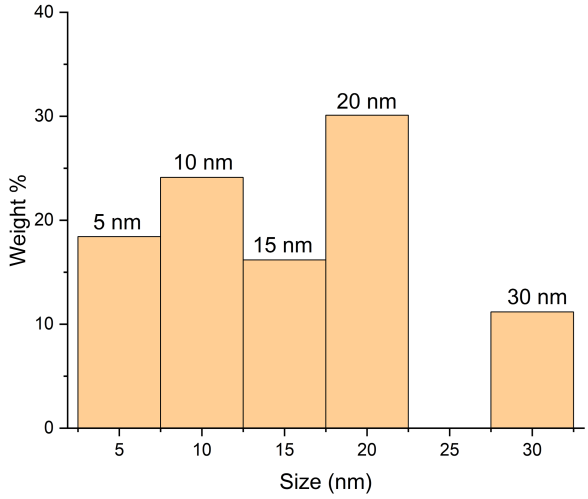


Table 6.2: *PDF refined structural parameters. MD-assisted modeling strategy is used.*

Lattice Parameter (Å)	MSD ($\times 10^{-3}$ Å^2)	Diameter (Å)	Rw %	$s_{5nm}/s_{10nm}/s_{15nm}/s_{20nm}/s_{30nm}$
4.0792	10.5	151.32	13.6	0.188/0.246/0.165/0.307/0.114

result. Second, improvement in MSD (10.5×10^{-3} Å^2) is clear as it approached our reference value of 9.7×10^{-3} Å^2 from MD simulations [18]. This was 15.61×10^{-3} Å^2 from the ACM modeling. Third, improvement in fitting quality increased as Rw decreased from 15.4 % to 13.6 %. Most of the improvement is observed in the high-r range, as shown in Figure 6.13. We note that most of the peaks were absent in this region when ACM modeling was used (compare high-r ranges of Figure 6.13 with Figure 6.9).

Figure 6.12: *Size distribution in polydispersed system as obtained from MD-assisted PDF modeling.*



Secondary Electron Scanning Transmission Electron Microscopy (SE-STEM) images of powder sample is shown in the Figure 6.14. Images showed that particles in powder were agglomerated, even though small spherical particles can be noticed. Elemental mapping analysis with Energy Dispersive X-ray Spectroscopy (EDX) clearly showed that the particle is composed of gold atoms in the Figure 6.15. TEM and High-Resolution Transmission Electron Microscopy (HRTEM) analysis showed that particles are crystallites in Figure 6.16, and the interplanar spacings of (111) and (200) planes ($d_{(111)}$=0.241 nm and $d_{(200)}$=0.207 nm) are in good agreement with the Joint Committee on Powder Diffraction Standards (JCPDS) data (04 0784) of FCC Au corresponding to the (111) and (200) lattice planes ($d_{(111)}$=0.236 nm and $d_{(200)}$=0.204 nm).

6.5 Summary and Conclusions

In this chapter, we investigated the possibility of extracting structural parameters from 14 nm gold nanocrystals using a laboratory X-ray diffractometer that provides an

Figure 6.13: *Comparison of fit quality between the measured and calculated PDF from MD-assisted polydisperse modeling. The difference between the two PDFs is shifted below for clarity and shown as green line. Fitting range was between 0-150 Å. For clarity, r-range is divided into three ranges: a) low-r range (0-50 Å), b) mid-r range (50-100 Å), c) high-r range (100-150 Å). Note the improved agreement at the high-r range compared to that of ACM modeling shown in Figure 6.9.*

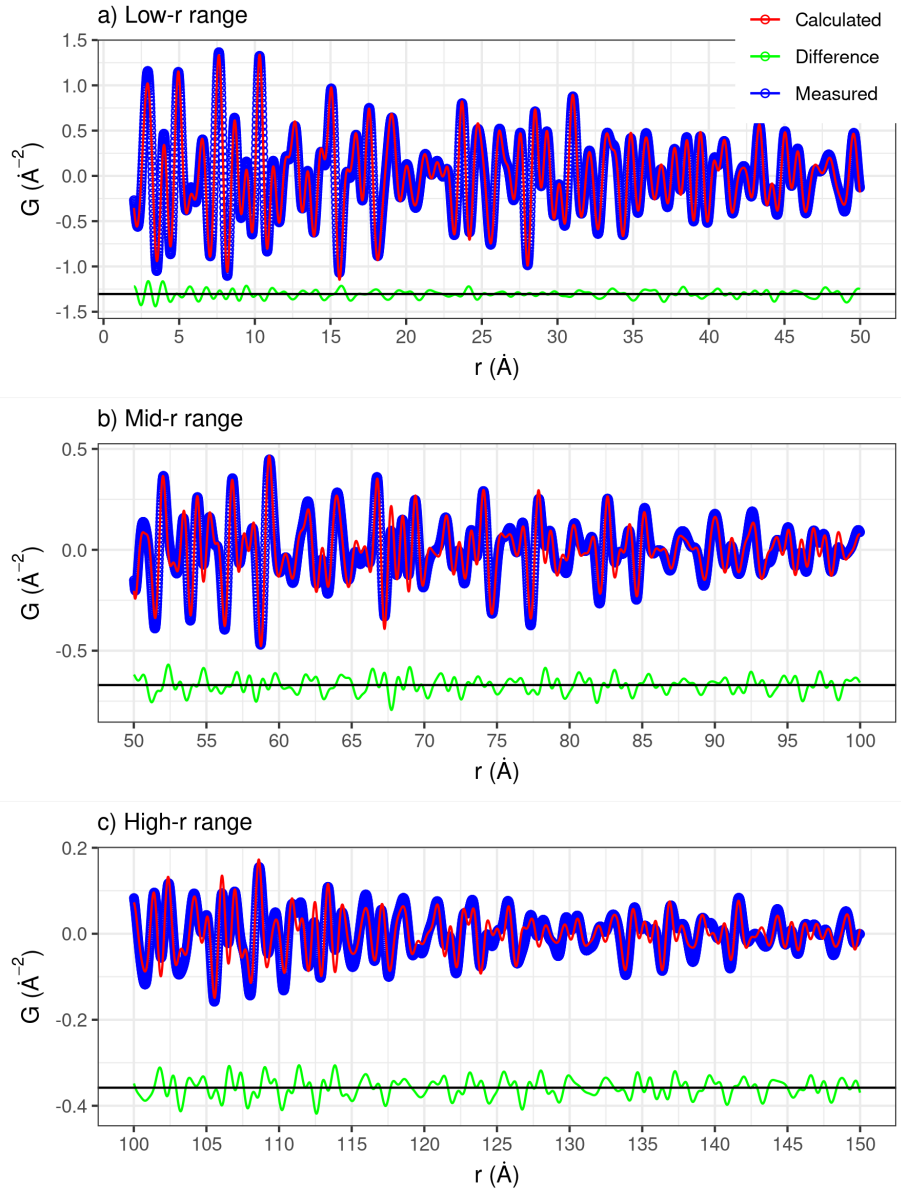


Figure 6.14: *SE-STEM images of the gold powder sample.*

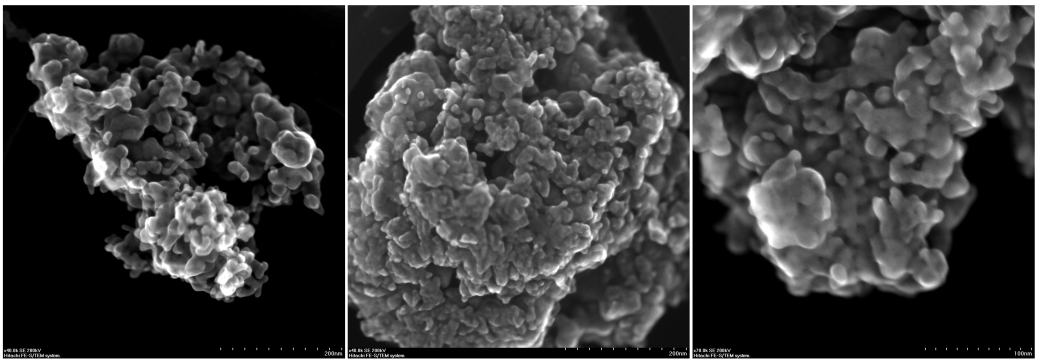


Figure 6.15: *Top figure, from left to right: electron image of the nanocrystal region, mapped elements with EDX in the selected region, only gold element is mapped in the selected region. Bottom figure: EDX map. The Cu signal comes from the copper gird used in the TEM.*

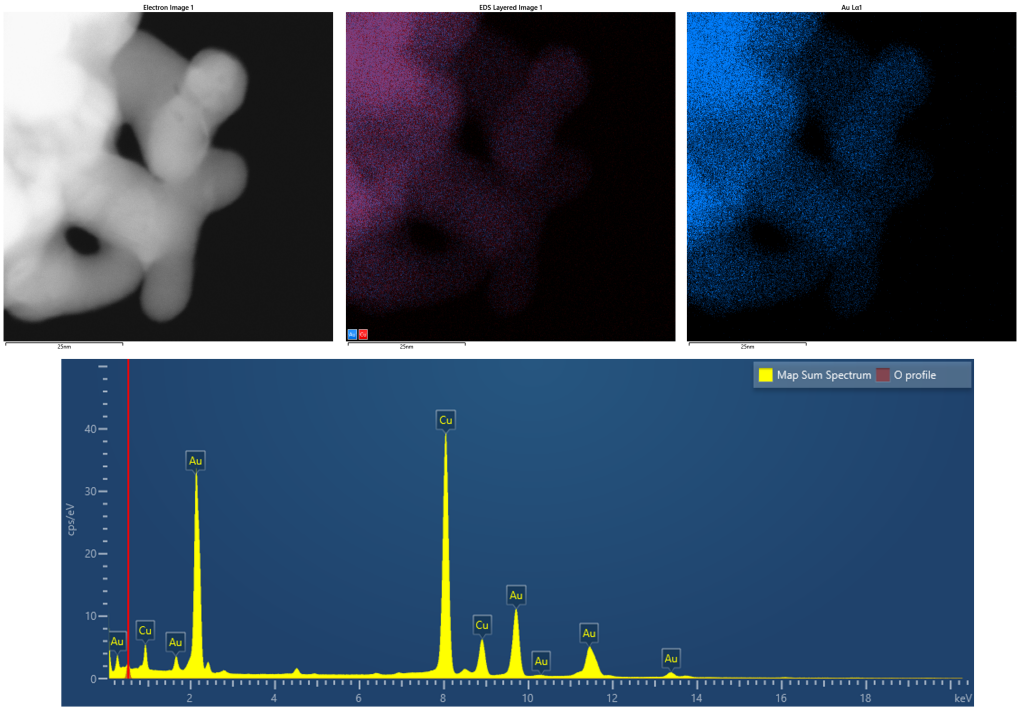
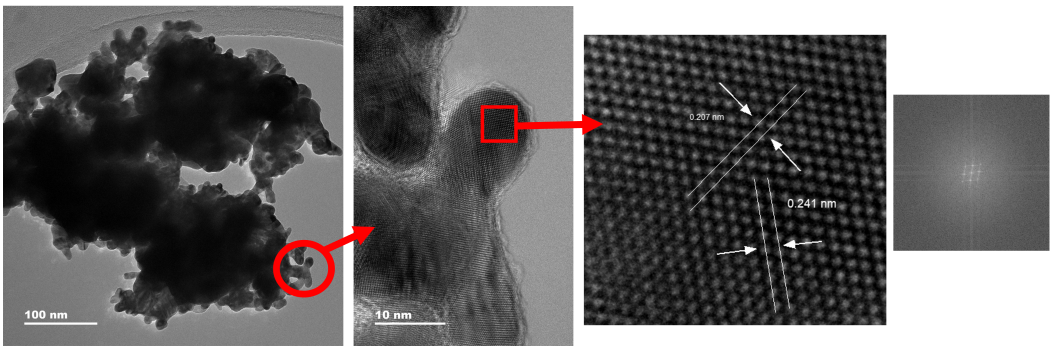


Figure 6.16: *From left to right: TEM, HRTEM, lattice planes, and FFT of the selected region.*



X-ray wavelength of 1.54 Å. Most PDF studies are conducted in synchrotrons due to their high flux and high energy beam sources. The PDF resolution is directly related to the energy of the X-ray beam; therefore, synchrotrons are useful in that sense. However, they are limited in number and have long queues. In contrast, laboratory diffractometers are common, but they provide low-resolution PDFs. In this Chapter, we showed that extracting structural parameters from PDF measured with a lab diffractometer is possible if the appropriate strategy is utilized. However, using other measurement techniques, such as TEM and SEM, will be helpful in the interpretation of structural parameters extracted from PDF. The main conclusions are listed as follows:

- PDF resolution is highly affected when a lab diffractometer is used. While some peaks shifted slightly, some peaks with low heights totally disappeared. Moreover, additional peak broadening is observed. We call it additional because PDF peak broadening is normally assigned to structure-related property, that is, MSD. Under this scenario, model-free analysis that relates peak position and width to interatomic distance and MSD is unreliable. Therefore, PDF modeling that includes finite Q_{max} effect in ideal PDF (not affected by instrument) is necessary.

- ACM modeling strategy that includes finite Q_{max} effect allowed extraction of average particle size and lattice parameter. However, we observed a high error in MSD when compared to theoretical MSD. ACM modeling assumes a monodispersed system, which is not realistic since there is always particle size distribution in real samples.

- MD-assisted modeling strategy provided more reliable MSD in addition to lattice parameter and particle sizes. Also, it allowed extraction of size distribution. Compared to ACM modeling, it provided better fit quality at the high-r range in PDF, where interatomic distances are comparable to particle diameters. The disadvantage of this technique is high computational demand since we scanned enormous lattice parameter - MSD space. The computational complexity of each PDF scales with N^2 where N is the number of atoms. In this regard, fast ACM modeling can be used for preliminary results.

7. CONCLUSIONS

In this thesis, we did an X-ray diffraction analysis of small nanocrystalline powders. Our main research question was correlating extracted structural parameters from the diffraction analysis with underlying nanocrystal structure. The difficulty for this correlation stems from incompatibility between the diffraction analysis algorithm that assumes infinite atomic planes and the nanocrystal structure that has a finite number of atomic planes due to finite dimensions. Moreover, single unit cell representation is used in the diffraction analysis algorithm. In contrast, realistic nanocrystals cannot be represented by single unit cell since surface unit cells behave differently than core unit cells. These incompatibilities cause errors in extracted structural parameters from diffraction analysis of nanocrystals. To conduct such a study, we developed a generalizable computational workflow. In this workflow, first, MD simulations are conducted to create realistic nanocrystals under different environmental conditions. Second, both local and average structural parameters are calculated from the atomic coordinates of nanocrystals. These are called true structural parameters. Third, the diffraction pattern is calculated from atomic coordinates. Fourth, diffraction analysis of calculated patterns is performed to extract structural parameters. These are called extracted structural parameters. Lastly, extracted parameters are correlated with true structural parameters calculated in step 2. This workflow can be used for other nanocrystal types by modifying atom types, nanocrystal shapes, alloying, surface chemistry, etc., to correlate extracted parameters from diffraction analysis with nanocrystal structure. In this study, diffraction analysis was performed by using two different methods: Rietveld and PDF analysis. In addition, we sought to apply PDF analysis of diffraction data with a lab diffractometer that provides relatively low X-ray energy compared to synchrotron sources. The main findings of the thesis can be summarized as follows:

- Rietveld analysis of diffraction data showed that the extracted lattice parameters have errors as large as 0.1 % for 5 nm nanocrystal at 0 K. The error is orders of magnitude higher than the precision of lab diffractometers. Moreover, the extracted lattice parameter correlates better with the core region of the nanocrystal rather than the particle-wide average lattice parameter that includes the surface region in addition to the core. The accuracy of extracted MSD depends on the selected method for TDS modeling. If TDS can be estimated accurately and subtracted before Rietveld analysis, errors can be minimized down to 5 % from 45 % of Chebyshev background functions. Finally, lattice strains extracted from Rietveld analysis closely follow lattice strains in the core region. Highly distorted surface lattice strains are invisible to Rietveld analysis.

- PDF analysis of diffraction data showed that errors in extracted lattice parameter have a similar trend to that of Rietveld analysis. However, PDF peak shapes were found to be temperature-dependent, deviating from Gaussian shapes with decreasing temperature due to changes in the relative ratio of static and dynamic atomic displacements. This caused a temperature-dependent error in the extracted lattice parameter with high error at low temperatures (0.16 % for 5 nm nanocrystal at 0 K). Extracted MSD from PDF analysis strongly correlated with dynamic MSD of nanocrystal at higher temperatures. Dynamic MSD errors were found to be around 3 % in contrast to -15 % of total MSD. However, PDF peaks deviated from the Gaussian profile as static MSD dominates dynamic MSD at lower temperatures, causing higher deviation of extracted MSD from dynamic MSD of nanocrystal. In general, extracted MSD from PDF analysis agrees better with particle-wide average dynamic MSD of nanocrystal (-3 %) at higher temperatures compared to extracted MSD from Rietveld analysis (45 %) without TDS modeling. Finally, within the correlated atomic motion parameters, δ_1 provided better agreement with true structural

parameters.

- Experimental diffraction study of 14 nm gold nanocrystal showed that some of PDF peaks shifted, disappeared, and broadened due to low X-ray energy accessible by laboratory diffractometer (wavelength $\lambda = 1.54$Å). However, we showed that PDF analysis can still extract structural parameters using ACM that gives a good agreement factor Rw of 15.4 %. The better fit quality with Rw of 13.6 % was obtained when realistic nanocrystals from MD simulation were modeled as a polydispersed system.

Future Work

This work can be extended to

1) Nanocrystals with different surface chemistry. The surface of nanocrystals can be capped with ligand molecules to provide colloidal stability while avoiding agglomeration. Depending on ligand type, core-ligand interaction can increase the amount of static displacements on the surface of the nanocrystal. These kinds of particles may even have lower crystallinity compared to free-standing particles modeled in this study. Additional disorders due to ligand interaction will cause higher errors in Rietveld analysis results. As an alternative solution, PDF refinement with two phases - disordered and ordered phases - can be implemented in a small-box modeling algorithm.

2) Polydispersed nanocrystal systems with different particle sizes and shapes. The effect of polydispersity on extracted structural parameters is not clearly resolved yet. Most of the studies in the literature reported high disagreement between average particle size obtained from TEM and PDF analysis. The computational methodology developed here can be extended to study such systems.

3) Big-box modeling and differential evolutionary algorithm for disordered systems. We showed that surface and core regions of free-standing nanocrystals have different bond lengths, deviating from perfect lattice structures. Small-box modeling used in Chapter 5 uses a single unit to model the whole structure, causing errors in extracted structural parameters. However, it is not clear yet if we can minimize these errors by using other modeling strategies, such as big-box modeling and differential evolutionary algorithms, claimed to be superior to small-box modeling in disordered systems.

4) Complex modeling strategy. Developing an appropriate optimization algorithm that can find underlying structures from a pool consisting of particle shape, size, disorder amount, alloying, etc., can be highly influential for PDF analysis of nanomaterials. Obviously, amount of variables to be optimized can be huge but can be decreased by supporting optimization algorithms with additional information from other measurement techniques such as TEM, SEM, EDX, etc.

REFERENCES

[1] B. Palosz, E. Grzanka, S. Gierlotka, S. Stelmakh, R. Pielaszek, U. Bismayer, J. Neuefeind, H.-P. Weber, and W. Palosz, "Diffraction studies of nanocrystals: theory and experiment," *Acta Physica Polonica A*, vol. 102, no. 1, pp. 57–82, 2002.

[2] S. Xiong, H. Öztürk, S.-Y. Lee, P. M. Mooney, and I. C. Noyan, "The nanodiffraction problem," *Journal of Applied Crystallography*, vol. 51, no. 4, pp. 1102–1115, 2018.

[3] S. Xiong, S.-Y. Lee, and I. C. Noyan, "Average and local strain fields in nanocrystals," *Journal of Applied Crystallography*, vol. 52, no. 2, pp. 262–273, 2019.

[4] S. Tao, J. Billet, J. De Roo, and S. J. Billinge, "Rapid modeling of the local structure of metal oxide nanoparticles from pdf data: A case study using tio2 nanoparticles," *Chemistry of Materials*, vol. 36, no. 21, pp. 10912–10921, 2024.

[5] H. Ozturk, *Computational analysis of diffraction in ideal nanocrystalline powders*. Columbia University, 2015.

[6] B. E. Warren, *X-ray Diffraction*. Courier Corporation, 1990.

[7] B. D. Cullity and R. Smoluchowski, "Elements of x-ray diffraction," *Physics Today*, vol. 10, no. 3, pp. 50–50, 1957.

[8] M. S. Daw and M. I. Baskes, "Embedded-atom method: Derivation and application to impurities, surfaces, and other defects in metals," *Phys. Rev. B*, vol. 29, pp. 6443–6453, Jun 1984.

[9] S. M. Foiles, M. I. Baskes, and M. S. Daw, "Embedded-atom-method functions for the fcc metals cu, ag, au, ni, pd, pt, and their alloys," *Phys. Rev. B*, vol. 33, pp. 7983–7991, Jun 1986.

[10] A. Voter, J. Westbrook, and R. Fleischer, "Intermetallic compounds: Principles and practice," *ch*, vol. 4, pp. 77–90, 1995.

[11] P. Tian, "Molecular dynamics simulations of nanoparticles," *Annual Reports Section" C"(Physical Chemistry)*, vol. 104, pp. 142–164, 2008.

[12] H. Sheng, M. Kramer, A. Cadien, T. Fujita, and M. Chen, "Highly optimized embedded-atom-method potentials for fourteen fcc metals," *Physical Review B—Condensed Matter and Materials Physics*, vol. 83, no. 13, p. 134118, 2011.

[13] S. M. Rassoulinejad-Mousavi and Y. Zhang, "Interatomic potentials transferability for molecular simulations: A comparative study for platinum, gold and silver," *Scientific reports*, vol. 8, no. 1, p. 2424, 2018.

[14] A. P. Thompson, H. M. Aktulga, R. Berger, D. S. Bolintineanu, W. M. Brown, P. S. Crozier, P. J. In't Veld, A. Kohlmeyer, S. G. Moore, T. D. Nguyen, *et al.*, "Lammps-a flexible simulation tool for particle-based materials modeling at the atomic, meso, and continuum scales," *Computer Physics Communications*, vol. 271, p. 108171, 2022.

[15] D. J. Evans and B. L. Holian, "The nose–hoover thermostat," *The Journal of chemical physics*, vol. 83, no. 8, pp. 4069–4074, 1985.

[16] L. Gelisio, K. Beyerlein, and P. Scardi, "Atomistic modeling of lattice relaxation in metallic nanocrystals," *Thin Solid Films*, vol. 530, pp. 35–39, 2013.

[17] P. Derlet, S. Van Petegem, and H. Van Swygenhoven, "Calculation of x-ray spectra for nanocrystalline materials," *Physical Review B—Condensed Matter and Materials Physics*, vol. 71, no. 2, p. 024114, 2005.

[18] M. Batyrow, I. Erucar, and H. Öztürk, "Size dependent change of mean square displacement in gold nanocrystals: A molecular dynamics simulation," *Concurrency and Computation: Practice and Experience*, vol. 35, no. 24, p. e7566, 2023.

[19] M. Chen, L. Hung, C. Huang, J. Xia, and E. A. Carter, "The melting point of lithium: an orbital-free first-principles molecular dynamics study," *Molecular Physics*, vol. 111, no. 22-23, pp. 3448–3456, 2013.

[20] G. A. Heiser, "Molecular dynamics calculation of mean square displacement in alkali metals and rare gas solids and comparison with lattice dynamics," Master's thesis, Brock University, 1984.

[21] L.-M. Peng, G. Ren, S. Dudarev, and M. Whelan, "Debye–waller factors and absorptive scattering factors of elemental crystals," *Acta Crystallographica Section A: Foundations of Crystallography*, vol. 52, no. 3, pp. 456–470, 1996.

[22] B.-J. Lee, J.-H. Shim, and M. Baskes, "Semiempirical atomic potentials for the fcc metals cu, ag, au, ni, pd, pt, al, and pb based on first and second nearest-neighbor modified embedded atom method," *Physical Review B*, vol. 68, no. 14, p. 144112, 2003.

[23] C. Zeni, K. Rossi, T. Pavloudis, J. Kioseoglou, S. de Gironcoli, R. E. Palmer, and F. Baletto, "Data-driven simulation and characterisation of gold nanoparticle melting," *Nature Communications*, vol. 12, no. 1, p. 6056, 2021.

[24] C. Mays, J. Vermaak, and D. Kuhlmann-Wilsdorf, "On surface stress and surface tension: Ii. determination of the surface stress of gold," *Surface science*, vol. 12, no. 2, pp. 134–140, 1968.

[25] "Debyer." `https://debyer.readthedocs.io/en/latest/`. Accessed: 2024.

[26] R. Young, "Introduction to the rietveld method," *The Rietveld Method*, pp. 1–38, 1993.

[27] "Gsas manual." `http://ccp14.cryst.bbk.ac.uk/ccp/web-mirrors/pssp/pdf/GSASManual.pdf`. Accessed: 2024.

[28] B. Palosz, E. Grzanka, S. Gierlotka, and S. Stelmakh, "Nanocrystals: Breaking limitations of data analysis," *Zeitschrift für Kristallographie - Crystalline Materials*, vol. 225, no. 12, pp. 588–598, 2010.

[29] P. Brown, A. Fox, E. Maslen, M. O'keefe, and B. Willis, "6.1. intensity of diffracted intensities," *International Tables for Crystallography C*, vol. 554, 2006.

[30] B. H. Toby and R. B. Von Dreele, "Gsas-ii: the genesis of a modern open-source all purpose crystallography software package," *Journal of Applied Crystallography*, vol. 46, no. 2, pp. 544–549, 2013.

[31] A. J. C. Wilson, "X-ray optics: the diffraction of x-rays by finite and imperfect crystals," *(No Title)*, 1962.

[32] A. Guinier, *X-ray diffraction: in crystals, imperfect crystals, and amorphous bodies*. Courier Corporation, 2013.

[33] M. A. Krivoglaz, *X-ray and neutron diffraction in nonideal crystals*. Springer Science & Business Media, 2012.

[34] R. W. James, "The optical principles of the diffraction of x-rays," *(No Title)*, 1948.

[35] J. Als-Nielsen and D. McMorrow, *Elements of modern X-ray physics*. John Wiley & Sons, 2011.

[36] A. Vaitkus, A. Merkys, and S. Gražulis, "Validation of the crystallography open database using the crystallographic information framework," *Journal of applied crystallography*, vol. 54, no. 2, pp. 661–672, 2021.

[37] S. Stelmakh, K. Skrobas, S. Gierlotka, and B. Palosz, "Effect of the surface on the internal structure of cdse crystal lattice based on molecular dynamics simulations," *Journal of Nanoparticle Research*, vol. 19, pp. 1–16, 2017.

[38] Y. Kuru, M. Wohlschlögel, U. Welzel, and E. Mittemeijer, "Crystallite size dependence of the coefficient of thermal expansion of metals," *Applied physics letters*, vol. 90, no. 24, 2007.

[39] W. D. Callister Jr and D. G. Rethwisch, *Materials science and engineering: an introduction*. John wiley & sons, 2020.

[40] J. James, J. Spittle, S. Brown, and R. Evans, "A review of measurement techniques for the thermal expansion coefficient of metals and alloys at elevated temperatures," *Measurement science and technology*, vol. 12, no. 3, p. R1, 2001.

[41] K.-i. Ohshima, A. Hayashi, and J. Harada, "X-ray diffraction study of fine gold particles prepared by gas evaporation technique. ii. characteristic temperature," *Journal of the Physical Society of Japan*, vol. 48, no. 5, pp. 1631–1635, 1980.

[42] P. Fornasini and R. Grisenti, "On exafs debye-waller factor and recent advances," *Journal of synchrotron radiation*, vol. 22, no. 5, pp. 1242–1257, 2015.

[43] A. Stukowski, J. Markmann, J. Weissmüller, and K. Albe, "Atomistic origin of microstrain broadening in diffraction data of nanocrystalline solids," *Acta Materialia*, vol. 57, no. 5, pp. 1648–1654, 2009.

[44] J. Eastman, M. R. Fitzsimmons, and L. Thompson, "The thermal properties of nanocrystalline pd from 16 to 300 k," *Philosophical Magazine B*, vol. 66, no. 5, pp. 667–696, 1992.

[45] C. Yang and S. Li, "Size-dependent phase stability of silver nanocrystals," *The Journal of Physical Chemistry C*, vol. 112, no. 42, pp. 16400–16404, 2008.

[46] K. Sadaiyandi, "Size dependent debye temperature and mean square displacements of nanocrystalline au, ag and al," *Materials Chemistry and Physics*, vol. 115, no. 2-3, pp. 703–706, 2009.

[47] M. W. Terban and S. J. Billinge, "Structural analysis of molecular materials using the pair distribution function," *Chemical Reviews*, vol. 122, no. 1, pp. 1208–1272, 2021.

[48] L. Yang, P. Juhás, M. W. Terban, M. G. Tucker, and S. J. Billinge, "Structure-mining: screening structure models by automated fitting to the atomic pair distribution function over large numbers of models," *Acta Crystallographica Section A: Foundations and Advances*, vol. 76, no. 3, pp. 395–409, 2020.

[49] S. Billinge, "Nanometre-scale structure from powder diffraction: total scattering and atomic pair distribution function analysis," 2019.

[50] M. Harada, R. Ikegami, L. S. R. Kumara, S. Kohara, and O. Sakata, "Reverse monte carlo modeling for local structures of noble metal nanoparticles using high-energy xrd and exafs," *RSC advances*, vol. 9, no. 51, pp. 29511–29521, 2019.

[51] L. Kumara, O. Sakata, S. Kohara, A. Yang, C. Song, K. Kusada, H. Kobayashi, and H. Kitagawa, "Origin of the catalytic activity of face-centered-cubic ruthenium nanoparticles determined from an atomic-scale structure," *Physical Chemistry Chemical Physics*, vol. 18, no. 44, pp. 30622–30629, 2016.

[52] O. Gereben and L. Pusztai, "Rmc_pot: a computer code for reverse monte carlo modeling the structure of disordered systems containing molecules of arbitrary complexity," *Journal of computational chemistry*, vol. 33, no. 29, pp. 2285–2291, 2012.

[53] K. Page, T. C. Hood, T. Proffen, and R. B. Neder, "Building and refining complete nanoparticle structures with total scattering data," *Journal of Applied Crystallography*, vol. 44, no. 2, pp. 327–336, 2011.

[54] T.-M. Usher, D. Olds, J. Liu, and K. Page, "A numerical method for deriving shape functions of nanoparticles for pair distribution function refinements," *Acta Crystallographica Section A: Foundations and Advances*, vol. 74, no. 4, pp. 322–331, 2018.

[55] P. Debye, "Zerstreuung von röntgenstrahlen," *Annalen der Physik*, vol. 351, no. 6, pp. 809–823, 1915.

[56] M. Batyrow, İ. Erucar, and H. Öztürk, "Static and dynamic atom displacements in nanocrystalline powders from diffraction analysis at finite temperature," *Materialia*, vol. 34, p. 102099, 2024.

[57] K. W. Chapman, S. H. Lapidus, and P. J. Chupas, "Applications of principal component analysis to pair distribution function data," *Journal of Applied Crystallography*, vol. 48, no. 6, pp. 1619–1626, 2015.

[58] C. A. Reiss, A. Kharchenko, and M. Gateshki, "On the use of laboratory x-ray diffraction equipment for pair distribution function (pdf) studies," 2012.

[59] S. Stelmakh, K. Skrobas, S. Gierlotka, and B. Palosz, "Application of pdf analysis assisted by md simulations for determination of the atomic structure and crystal habit of cdse nanocrystals," *Journal of Physics: Condensed Matter*, vol. 30, no. 34, p. 345901, 2018.

[60] M. Sommariva, M. Gateshki, J.-A. Gertenbach, J. Bolze, U. König, B. Ş. Vasile, and V.-A. Surdu, "Characterizing nanoparticles with a laboratory diffractometer: from small-angle to total x-ray scattering," *Powder Diffraction*, vol. 29, no. S1, pp. S47–S53, 2014.

[61] J. Beyer, K. Kato, and B. Brummerstedt Iversen, "Synchrotron total-scattering data applicable to dual-space structural analysis," *IUCrJ*, vol. 8, no. 3, pp. 387–394, 2021.

[62] P. Juhás, T. Davis, C. L. Farrow, and S. J. Billinge, "Pdfgetx3: a rapid and highly automatable program for processing powder diffraction data into total scattering pair distribution functions," *Journal of applied crystallography*, vol. 46, no. 2, pp. 560–566, 2013.

[63] T. Egami and S. J. Billinge, *Underneath the Bragg peaks: structural analysis of complex materials*, vol. 16. Elsevier, 2003.

[64] I.-K. Jeong, R. Heffner, M. Graf, and S. Billinge, "Lattice dynamics and correlated atomic motion from the atomic pair distribution function," *Physical Review B*, vol. 67, no. 10, p. 104301, 2003.

[65] X. Qiu, E. S. Božin, P. Juhas, T. Proffen, and S. J. Billinge, "Reciprocal-space instrumental effects on the real-space neutron atomic pair distribution function," *Journal of Applied Crystallography*, vol. 37, no. 1, pp. 110–116, 2004.

[66] P. Juhás, C. Farrow, X. Yang, K. Knox, and S. Billinge, "Complex modeling: a strategy and software program for combining multiple information sources to solve ill posed structure and nanostructure inverse problems," *Acta Crystallographica Section A: Foundations and Advances*, vol. 71, no. 6, pp. 562–568, 2015.

[67] B. Gilbert, "Finite size effects on the real-space pair distribution function of nanoparticles," *Journal of Applied Crystallography*, vol. 41, no. 3, pp. 554–562, 2008.

[68] D. J. Sprouster, L. L. Snead, E. Dooryhee, S. K. Ghose, T. Koyanagi, and Y. Katoh, "Pair distribution function analysis of neutron-irradiated silicon carbide," *Journal of Nuclear Materials*, vol. 527, p. 151798, 2019.

[69] I.-K. Jeong, T. Proffen, F. Mohiuddin-Jacobs, and S. J. Billinge, "Measuring correlated atomic motion using x-ray diffraction," *The Journal of Physical Chemistry A*, vol. 103, no. 7, pp. 921–924, 1999.

[70] K. Jurkiewicz, M. Kamiński, W. Glajcar, N. Woźnica, F. Julienne, P. Bartczak, J. Polański, J. Lelątko, M. Zubko, and A. Burian, "Paracrystalline structure of gold, silver, palladium and platinum nanoparticles," *Journal of Applied Crystallography*, vol. 51, no. 2, pp. 411–419, 2018.

[71] B. Gilbert, F. Huang, H. Zhang, G. A. Waychunas, and J. F. Banfield, "Nanoparticles: strained and stiff," *Science*, vol. 305, no. 5684, pp. 651–654, 2004.

[72] K. Page, T. Proffen, S. McLain, T. Darling, and J. TenCate, "Local atomic structure of fontainebleau sandstone: Evidence for an amorphous phase?," *Geophysical research letters*, vol. 31, no. 24, 2004.

[73] A. Maeland and T. B. Flanagan, "Lattice spacings of gold–palladium alloys," *Canadian journal of physics*, vol. 42, no. 11, pp. 2364–2366, 1964.

[74] C. L. Farrow and S. J. Billinge, "Relationship between the atomic pair distribution function and small-angle scattering: implications for modeling of nanoparticles," *Acta Crystallographica Section A: Foundations of Crystallography*, vol. 65, no. 3, pp. 232–239, 2009.

[75] V. Petkov, B. N. Wanjala, R. Loukrakpam, J. Luo, L. Yang, C.-J. Zhong, and S. Shastri, "Pt–au alloying at the nanoscale," *Nano letters*, vol. 12, no. 8, pp. 4289–4299, 2012.

[76] C. C. Yang and S. Li, "Investigation of cohesive energy effects on size-dependent physical and chemical properties of nanocrystals," *Physical Review B—Condensed Matter and Materials Physics*, vol. 75, no. 16, p. 165413, 2007.

[77] J. Beyer, N. Roth, and B. Brummerstedt Iversen, "Effects of voigt diffraction peak profiles on the pair distribution function," *Acta Crystallographica Section A: Foundations and Advances*, vol. 78, no. 1, pp. 10–20, 2022.

[78] A. Altomare, N. Corriero, C. Cuocci, A. Falcicchio, A. Moliterni, and R. Rizzi, "Qualx2. 0: a qualitative phase analysis software using the freely available database pow_cod," *Journal of Applied Crystallography*, vol. 48, no. 2, pp. 598–603, 2015.

VITA

Name Surname Merdan Batyrov

Education

- Ph.D. Mechanical Engineering, Özyeğin University, 2020-
- B.Sc. Bioengineering, Yildiz Technical University, 2015-2019.

Work Experience

- Feb. 2020 – Jan. 2025, Teaching Assistant at Ozyegin University.
- Jan. 2019 – Feb. 2019, Intern at the Spinamer Health Products Industry and Technology.
- Jun. 2018 – Jul. 2018, Researcher at the Sezerman Lab in Acıbadem University.

Awards and Scholarships

- 2024, Scholarship for Academic Performance, TUBITAK 2250.
- 2023, IUCr Travel Support Bursary for European Crystallographic School at the BESSY II electron storage ring, Berlin, Germany.

Publications

- M. Batyrow, I. Erucar, and H. Öztürk, "Static and dynamic atom displacements in nanocrystalline powders from diffraction analysis at finite temperature," *Materialia*, vol. 34, p. 102099, 2024.

- M. Batyrow, K. Dericiler, B. A. Palabiyik, B. S. Okan, H. Öztürk, and I. Erucar, "Combining tensile test results with atomistic predictions of elastic modulus of graphene/polyamide-6,6 nanocomposites," *Materials Today Communications*, vol. 35, p. 105636, 2023.

- M. Batyrow, I. Erucar, and H. Öztürk, "Size dependent change of mean square displacement in gold nanocrystals: A molecular dynamics simulation," *Concurrency and Computation: Practice and Experience*, vol. 35, no. 24, p. e7566, 2023.

- B. Akkoca Palabıyık, M. Batyrow, and I. Erucar, "Computational investigations of bio-mof membranes for uremic toxin separation," *Separation and Purification Technology*, vol. 281, p. 119852, 2022.

- A. Baloochiyan, M. Batyrov, and H. Ozturk, "Accuracy limits of pair distribution function analysis in structural characterization of nanocrystalline powders by x-ray diffraction," *Journal of the Turkish Chemical Society Section A: Chemistry*, vol. 9, p. 527–544, 2022.

- O. Isik, M. Batyrow, A. M. Abdelrahman, I. Orman, H. Ozgun, M. E. Ersahin, M. E. Pasaoglu, I. Demir, and I. Koyuncu, "Dynamic membrane bioreactor performance for treatment of municipal wastewaters at different sludge concentrations," *Environmental Technology & Innovation*, vol. 22, p. 101452, 2021.

Presentations

- BAŞARIM 2022 Conference, Istanbul, Turkey.